UNIVERSITÀ DEGLI STUDI DI MILANO

DEPARTMENT OF PHYSICS

PHD SCHOOL IN
PHYSICS, ASTROPHYSICS AND APPLIED PHYSICS
CYCLE XXXII

EXPERIMENTAL AND MODELLING APPROACHES TO INVESTIGATE OPTICAL PROPERTIES OF ATMOSPHERIC AEROSOL

Disciplinary Scientific Sector FIS/07

PhD Thesis of:
Sara Valentini

Director of the School: Prof. Matteo Paris
Supervisor of the Thesis: Prof. Roberta Vecchi

A.Y. 2019-2020

To my mother

Contents

List of Figures

List of Tables

Abstract

The aerosol scientific community has a strong interest in improving knowledge about aerosol physical-chemical properties and measurement methodologies due to the large uncertainties still affecting estimates of aerosol optical properties and their impact on climate, visibility, and air quality. Therefore, in this PhD work, the contribution to this research field was mainly devoted to the study and implementation of experimental and modelling approaches aiming at filling some gaps in the current knowledge about absorption and scattering properties of atmospheric aerosols.
This PhD activities are shortly summarised in the following.

- The widespread U.S. IMPROVE algorithm used to estimate light extinction coefficient and visibility in natural parks and rural areas, based on atmospheric compositional and meteorological data, was tailored for a reliable application at a polluted urban site like Milan (Italy). Briefly, in order to reduce possible biases of the IMPROVE algorithm when applied at polluted urban sites, an equation with tailored (i.e. site-specific) coefficients was implemented. To this aim, a discrete dipole approximation code using as input data aerosol size distributions measured in Milan was employed to compute site-specific dry mass extinction efficiencies and water growth functions for major aerosol components. This new approach was applied to a PM_1 dataset available for Milan and the role of sources – assessed by the application of a receptor model – in visibility impairment and atmospheric extinction was evaluated. Details can be found in publications P2, P3, IO2, IP6, NO1, NP2.

- Experimental improvements and measurements were carried out during the PhD thesis using the multi-wavelength polar photometer (PP_UniMI) developed by the Environmental Physics research group in Milan for the assessment of aerosol absorption coefficient. This is a flexible instrument that allowed the investigation of biases affecting widespread on-line instrumentation for aerosol absorption measurements as well as applications to very different samples collected during collaborative field campaigns. Suitable set-ups were realised to carry out such measurements. The home-made polar photometer was checked in the past against a filter-based "reference" instrument; during this PhD work an inter-comparison

exercise was carried out in a laboratory experiment realised in collaboration with the Jülich Forschungszentrum (Germany) and the University of Genoa (Italy). Briefly, samples of laboratory-generated aerosol of different types and mixtures were collected on filters and measured in parallel by on-line instrumentation as for aerosol extinction, scattering, and absorption coefficients (IO1, IP3). On-line data were then compared with those from the off-line analysis performed with PP_UniMI and MWAA (a home-made filter-based photometer developed at the University of Genoa) showing a very good agreement. This was a relevant result for the research group and the scientific community because – as already mentioned – PP_UniMI can be used to investigate biases affecting instrumentation largely used by the scientific community (e.g. Aethalometers), which produces data for air quality and climate models. Indeed, this kind of investigation is currently an open issue and it is in progress at the Milan research group (IO6, IO7, IP2).

During the PhD, multi-wavelength photometer measurements were performed on atmospheric aerosol samples collected on filters in the frame of various experimental campaigns, as shortly described in the following.

- Participation to international collaborative project CARE (Carbonaceous Aerosol in Rome and Environs). It was carried out in Rome (Italy) using a variety of instruments and techniques in order to obtain a comprehensive and highly time-resolved picture of the aerosol properties at a Mediterranean urban background site. An overview of measurements performed and methodologies applied is reported in the paper P4. Apart from the collection of the samples and the assessment of the absorption coefficient, the contribution given to this research project during this PhD has been devoted to the identification and classification of aerosol types and their phenomenology exploiting all the available information about high-time resolved optical properties, chemical composition and size distribution of atmospheric aerosol. The main objective was to find out one or more possible combinations of intensive optical parameters that can be used as an original tool to identify aerosols with different origins, with the support of chemical and size information (IO4, IP1, S1).

- Participation to the ACTRIS-2 (Aerosol, Clouds and TRace gases InfraStructure) – Mt. Cimone and Po Valley Field Campaign. Multi-wavelength measurements of the absorption coefficient of aerosol samples collected at three sites with different characteristics were performed. This piece of information will be useful for inter-comparison purposes with other instrumentation in the field.

- Participation to a collaborative project together with research groups of the

University La Sapienza and IIA-CNR in Rome. In this case, the assessment of multi-wavelength aerosol absorption coefficient on samples collected during two campaigns (summertime and wintertime) in an area heavily impacted by anthropogenic sources (Terni - Italy) was coupled with a detailed chemical characterisation. The focus was to investigate the relationship between chemical composition and optical properties and to understand the differences between indoor and outdoor sites: indeed, it was the first time that indoor samples were measured for multi-wavelength optical absorption with PP_UniMI (and likely in the literature), and the system was optimised for the analyses of filters with a reduced sampled area. This work gave rise to an additional sampling campaign during which outdoor and indoor samples were collected in parallel in order to find suitable tracers of cigarette smoke: these filters were also measured with PP_UniMI to retrieve aerosol absorption and its spectral dependence.

It is also noteworthy to mention that six months (February-July 2018) were spent at the Department of Physics (Aerosol Physics and Environmental Physics Group) of the University of Vienna (Austria) with a fellowship obtained by the Erasmus+ Traineeship programme. The aim was to investigate methods to measure aerosol scattering coefficient and transfer the acquired expertise to the Milan research group. On-line instrumentation measuring multi-wavelength aerosol scattering coefficient at different scattering angles (i.e. polar Nephelometers – both commercial and home-made) was studied, with a focus on the truncation correction needed for this kind of instruments. A laboratory experiment was designed and realised deploying different on-line instruments that measured several properties of non-absorbing laboratory-generated aerosol particles of known size. The truncation correction was investigated via optical modelling simulations whose results were compared with directly measured scattering properties (IO8). This activity gave rise to the participation to an additional experiment focused on dust particles (i.e. with also absorption properties), whose results are still under investigation.

The knowledge gained about both absorption and scattering properties of atmospheric aerosol was used to analyse in detail all optical properties measured on-line with high-time resolution during the CARE experiment.

In addition to activities described above, several collaborations were performed during this PhD to other works carried out by the Environmental Physics research group in the frame of various national and international projects (see P1, P5, V1, IO3, IO5, IO9, IP4, IP5, NO2, NO3, NO4, NP1, NP3 in the List of Publications).

Introduction

Motivation

Optical properties of atmospheric aerosol are crucial for their role in Earth radiation budget and on visibility.
Aerosol particles both scatter and absorb light, causing the cooling and heating of the atmosphere, respectively; however, the dominant effect has not been assessed yet. Moreover, they also affect the reflectivity of clouds and Earth surface, further contributing to atmospheric temperature profile and fostering feedback processes. In addition, atmospheric aerosol also impacts on visibility, which depends on light extinction (the sum of scattering and absorption) and is a parameter strictly related to air quality and its perception by people.
Progresses have been done so far in knowledge of aerosol effects on climate: indeed, the increasing interest and number of studies about aerosol optical properties allowed to estimate their total radiative forcing (RF), that was not assessed e.g. in the first reports of the Intergovernmental Panel on Climate Change (IPCC) in 1996 and 2001. Nevertheless, due to the complexity of the aerosol system, a reliable value of RF due to aerosol is still lacking, being affected by an uncertainty as big as the estimate itself as recorded in the last IPCC report (2013).
Conversely to mass concentration and chemical composition of atmospheric aerosol, optical properties are not routinely measured by monitoring networks, although being key parameters needed as input in climate models. The collection of more reliable and abundant experimental data and their exploitation in advanced models are therefore mandatory to gain information about aerosol optical properties and their relationship with the concentration of chemical species, in order to reduce uncertainties in estimates of atmospheric aerosol effect on Earth radiation balance.
In addition to a better evaluation of aerosol radiative effects, improving the knowledge of optical properties of atmospheric particles could allow to face a number of open issues still affecting aerosol science.
One of the major topics that deserves further investigation is the relationship between scattering, absorption, and extinction coefficients of atmospheric particles and con-

centrations of different aerosol species. Indeed, the link between optical properties and mass concentration depends on the location and season. Thus, determining such relationship is complex and needs the collection of more experimental data and the development of tailored models.
Another open issue is represented by aerosol absorbing species, whose estimated radiative effect is affected by the highest uncertainty among all aerosols and precursors. Among absorbing species, Black Carbon (BC) is the largest contributor in particulate form to atmospheric radiative forcing and can also deposit on snow with feedback effects. Besides BC, other species such as light-absorbing organic matter (Brown Carbon) and mineral dust are considered as contributors to the heating of the atmosphere, even though a deep knowledge of their impact and properties is a current gap in atmospheric science.

In this thesis, both experimental and modelling approaches were studied and explored in order to contribute to a better knowledge of optical properties of atmospheric aerosol. Scattering, absorption, and extinction properties were investigated separately and combined together when possible, often focusing on their wavelength dependence, to provide a complete overview.

Thesis outline

In Chapter 1 an introduction and overview of main characteristics of atmospheric aerosol is provided. Moreover, a description of optical properties of individual particles and of a particle ensemble is reported, comprising a summary of results obtained by theories dealing with scattering and absorption in different size regimes, a focus on the wavelength dependence of optical properties, and the relevance of aerosol mixing state. Finally, effects of atmospheric aerosol on Earth radiation balance and on visibility are briefly described.
Chapter 2 reports several experimental and modelling methodologies developed in this thesis. A brief description of on-line instruments used in this work is presented. Moreover, methodological advancements carried out in the thesis about experimental techniques are described in Section 2.2. The set-up and principle of operation of the polar photometer PP_UniMI, an inter-comparison of its results with on-line instrumentation, and the optimisation of its set-up for the analyses of non conventional filters are explained. In addition, biases commonly affecting widespread on-line instruments to measure aerosol scattering and absorption coefficients are recalled; the use of both experimental data and models to investigate the scattering enhancement factor (in filter-based instruments) and the truncation correction (in Nephelometers)

are presented. Finally, the IMPROVE algorithm used to retrieve atmospheric light extinction is introduced and the tailored approach developed in this work is described. Chapter 3 reports applications of the methodologies developed in the thesis and major results of the experimental activity carried out in this work. In particular, data collected with on-line instruments and retrieved from PP_UniMI measurements in the frame of the Carbonaceous Aerosol in Rome and Environs (CARE) international project are presented, focusing on the combination of several optical properties and on their wavelength dependence. Furthermore, a description of major results obtained by PP_UniMI measurements performed on non conventional filters, including its first application to indoor samples, is given. Finally, an estimate of aerosol sources contributions to light extinction is presented, as obtained by coupling the application of the tailored IMPROVE approach and a source apportionment study to a completely characterised PM_1 dataset.

Chapter 1

Atmospheric aerosol: generalities, optical properties and effects

1.1 Atmospheric aerosol generalities: formation, sources, size-distribution

Atmospheric aerosol is a polydisperse collection of solid and liquid particles suspended in the atmosphere, each one maintaining its physical-chemical properties long enough to allow their observation and measurement.
In the last decades, atmospheric aerosol (also called particulate matter - PM) has raised increasing interest due to its impacts on both environment and human health [1]. In particular, aerosol can [2, 3, 4, 5]:

- affect Earth radiative balance, via its optical properties (scattering and absorption - direct effect) and by changing clouds lifetime and albedo (indirect effect);
- act as cloud and ice condensation nuclei;
- be a catalyst in chemical reactions taking place in the atmosphere;
- cause air and water pollution via dry and wet deposition processes;
- impair visibility and damage cultural heritage;
- be detrimental for human health, entering the respiratory tract and reaching other parts of the body.

Atmospheric aerosol is a very complex system; it is generated by different sources and emission processes and it shows a significant heterogeneity in terms of particles chemical composition, size, shape, and residence time. Finally, aerosol properties are

highly variable in space and time.
Formation processes of atmospheric aerosol comprise [6, 7]:

- disintegration of liquids or solids, resuspension of powder, breakup of agglomerates, and direct emissions from combustion processes; these mechanisms directly emit particles (primary aerosol) in the atmosphere;
- gas-to particle conversions originating secondary aerosol.

Particles formation pathways affect their physical-chemical properties: for instance, aerosol generated from gaseous precursors and fresh, primary combustion products tends to be smaller (particle diameter $d_p < 1\,\mu$m), whereas primary mechanically generated aerosol has generally $d_p > 1\,\mu$m [6, 2, 7]. Aerosol particles undergo various atmospheric processing mechanisms, that modify their own characteristics, depending also on their native properties such as size and chemical composition. Major processes contributing to aerosol formation, transformation, and removal [8, 6, 2, 9, 5] are represented in Figure 1.1 and briefly described below.

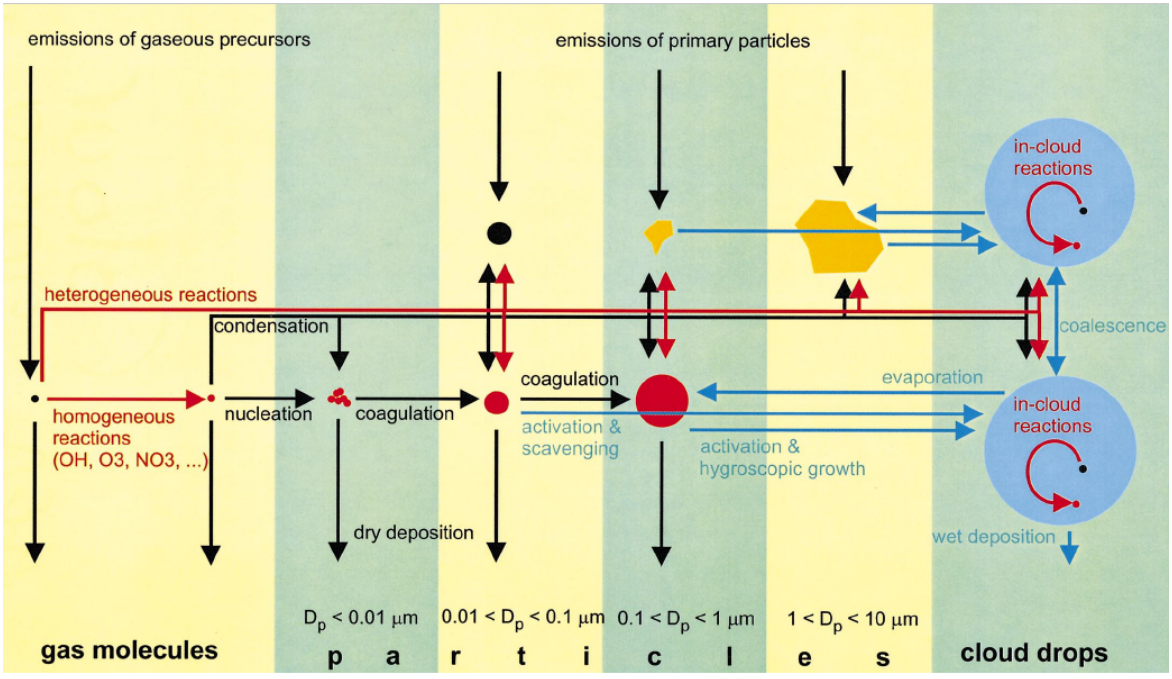

Figure 1.1: Scheme of major aerosol formation, transformation, and removal processes [2].

Homogeneous nucleation is the formation of particles from a super-saturated vapour without any condensation nuclei. This process is often referred to as "gas-to-particle conversion". Otherwise, *heterogeneous nucleation* leads to the formation of particles from a super-saturated vapour in presence of condensation nuclei. Aerosol formation and growth due to *condensation* are the most important mechanisms causing mass transfer from gaseous to particulate phase. Growth by condensation takes place when

molecular clusters formed by nucleation processes become larger than a critical size: stable atmospheric particles formed this way can increase in size due to condensation of vapour on their surface. Opposite to condensational growth, *evaporation* leads to more molecules leaving the surface of a particle compared to those that attach to it. Finally, *coagulation* takes place when two particles join together to form a unique and larger particle. Consequently, particle number decreases and the average diameter increases: this is one of the most important processes causing the passage of a particle from a size to a bigger one.
Finally, atmospheric aerosol is removed from the atmosphere via different deposition pathways [8, 3, 5]:

- dry deposition: particles are transported to a surface (e.g. the ground) and are then retained by it;

- wet deposition, that comprises: *fog deposition*, when particles get embedded in fog an mist droplets; *rain-out*, i.e. aerosol deposition caused by processes occurring in clouds, where particles serve as condensation nuclei for water droplets; *wash-out*, when aerosol particles are removed below clouds, where they are captured by precipitations.

Sources of atmospheric aerosol can be natural or anthropogenic. Among major sources of anthropogenic particles are: energy production, traffic, industrial activities, and domestic heating in urban and industrial areas; biomass burning, livestock and agricultural manure at rural sites. Natural aerosol sources comprise seas and oceans, deserts, soil, volcanoes, forests, and spontaneous fires. It is noteworthy that particles produced by different emission sources show different physical-chemical properties.
On a global scale, natural aerosol is significantly more abundant (of about one order of magnitude) than anthropogenic one [10, 5]. Nevertheless, the percentage of atmospheric particles produced by human activities can increase significantly and become comparable to the one of natural aerosol in densely populated and heavily industrialised areas. Moreover, anthropogenic aerosol deserves particular attention as it is related to aerosol potential detrimental effect on human health [5].
Table 1.1 reports emission fluxes of major natural and anthropogenic primary particles and secondary aerosol precursors. In the following, main natural and anthropogenic aerosol sources and their emissions [8, 11, 1, 5] are briefly discussed.

Table 1.1: Emission fluxes of major natural and anthropogenic primary particles and secondary aerosol precursors [4].

Aerosol type	Emission flux (per year)
Natural primary aerosols	
Desert dust	1000–3000 Tg
Sea spray	1000–6000 Tg
Biomass burning aerosols	20–35 Tg
Terrestrial primary biogenic aerosols	Order of 1000 Tg
Including bacteria	40–1800 Gg
Including spores	30 Tg
Precursors of natural secondary aerosols	
Dimethylsulphide (DMS)	20–40 Tg S
Volcanic SO_2	6–20 Tg S
Terpenes	40–400 Tg
Anthropogenic primary aerosols	
Industrial dust	40–130 Tg
Biomass burning aerosols	50–90 Tg
Black carbon (from fossil fuel)	6–10 Tg
Organic carbon (from fossil fuel)	20–30 Tg
Anthropogenic secondary aerosols	
SO_2	70–90 Tg S
Volatile organic compounds (VOCs)	100–560 Tg C
NH_3	20–50 Tg N
NO*x*	30–40 Tg N

C carbon, S sulphur, N nitrogen

Among natural sources, the most relevant are described below.

- Erosion of the lithosphere and dust resuspension from soil
  One of the major contributions to the global amount of aerosol is given by the mineral fraction, comprising natural primary particles generated by wind erosion of the Earth surface. Crustal aerosol is generally characterised by particles with diameter in the range 1-100 μm, irregular shape, and elemental composition dominated by Al, Si, Ca, Ti, and Fe oxides.

- Sea spray
  Marine aerosol represents a major fraction of global atmospheric aerosol concentration. It has mainly primary origin: it is produced via processes such as evaporation of droplets and bubble burst in waves. Sea spray is composed for the major portion by Na and Cl and, in smaller amount, by Mg, S, K, Br, and Ca. Moreover, several organic compounds are produced by phytoplancton and are thus observed in particular near oceans surfaces.

- Biogenic emissions
  Vegetation and some micro-organisms contribute to both primary and secondary aerosol formation. Primary biogenic particles include pollens, spores and other large particles (with diameters up to 100 μm). Volatile organic compounds (VOCs) such as terpenes are precursors of secondary aerosol.

- Volcanic eruptions
  Volcanic eruptions emit particles and gaseous compounds in the high troposphere and sometimes up to the stratosphere. Emissions reaching high altitudes can spread an run long distances causing effects also at global scale. Volcanoes emissions are mainly composed by water, and also by SO_2, CO_2, and NO_x, that undergo chemical reactions in the atmosphere and are therefore transformed into particles.

- Spontaneous forest fires
  Forest fires emit small particles containing mainly carbonaceous compounds and elements such as Mg, Ti, Na, and Ca.

Anthropogenic aerosol is mainly generated by emissions of particles and gaseous precursors by biomass and fossil fuel combustion. The most important sources of anthropogenic particles are listed below.

- Traffic
  In urban areas, traffic represents a relevant source of both primary and secondary aerosol. Vehicles are responsible for two kinds of emissions: exhaust (from tailpipe) and non-exhaust (from erosion of brakes, tyres and mechanical parts, via abrasion of roads surface and dust resuspention); each one accounts for about 50% of total traffic emissions [11]. Exhaust particles are mainly composed by C (especially from diesel vehicles), hydrocarbons and NO_x (a secondary aerosol precursor), whereas non-exhaust emissions include Mo, Fe, Cu, and Sb (from brakes), Ba and Zn (from tyres), besides Al, Si, Ca, Ti, and Fe (from dust resuspention). It is noteworthy that also railway traffic, airplanes, and ships are important aerosol sources, emitting especially metals (by railways), S, V, and Ni (by ships).

- Industries
  Industries emit typical combustion products and a variety of pollutants released during different production steps and whose properties depend on the type of process, the technology, and the materials used. For instance, S, heavy metals and hydrocarbons are emitted by chemical, petrochemical, and paper industries, while iron and steel industries emit C, Fe, Si, Ca, Mg, Pb, Zn, F, and metal oxides.

- Energy production
  Fossil fuel combustion employed to produce energy emits C, S, V, and, in a smaller amount, Na, Mg, Al, Ca, Fe, Ni, and Cu. The type of fuel and the production process largely affect composition and concentration of emitted aerosol.

- Domestic heating
  Domestic heating produces small particles with a chemical composition that depends on the fuel used. Coal and oil emissions are dominated by C, S, and V. In recent years, a widespread fuel is biomass (mainly wood), whose combustion generally emits small particles composed by C, Zn, K, Cl, and levoglucosan. It is noteworthy that properties and effects of wood burning emissions are largely affected by the appliances and the type of wood used.

- Waste incinerators
  Incinerators of solid waste are responsible for the emission of small particles mainly composed by Zn, K, and Cl, besides other elements depending on the type of waste burned.

Atmospheric aerosol is largely variable also in terms of shape, that is related to particles formation pathway [10, 5]. For instance, natural aerosol has usually an irregular shape, whereas anthropogenic particles (especially those produced by high temperature combustion processes) are typically spherical and smaller. Another fundamental aerosol feature is size. Since particles physical-chemical properties are heterogeneous, it is necessary to use equivalent diameters (based on specific aerosol features) in order to describe particles and compare them [10]. Some of the most commonly used equivalent diameters are defined in the following.

- Aerodynamic diameter (d_{ae}): equivalent diameter of a spherical particle of unit density having the same inertial properties (i.e. the same terminal settling velocity) as the actual particle.

- Optical diameter (d_{opt}): equivalent diameter of a spherical particle having the same refractive index as the one of particles used for the calibration of the optical instrument used to determine aerosol size distribution, that scatters the same amount of light in the measured solid angle.

- Electrical mobility diameter (d_m): equivalent diameter of a spherical particle having the same electrical mobility (i.e. the same migration velocity in an electric field) as the considered particle.

Aerosol size distribution is a key property depending on formation processes and affecting particles physical behaviour. Since atmospheric aerosol covers a wide range

of diameters (from a few nanometers to tens of micrometers), size distributions are usually represented as a function of the logarithm of the diameter itself. Size distributions can be expressed in terms of number, surface area, volume or mass of particles in different size fractions.

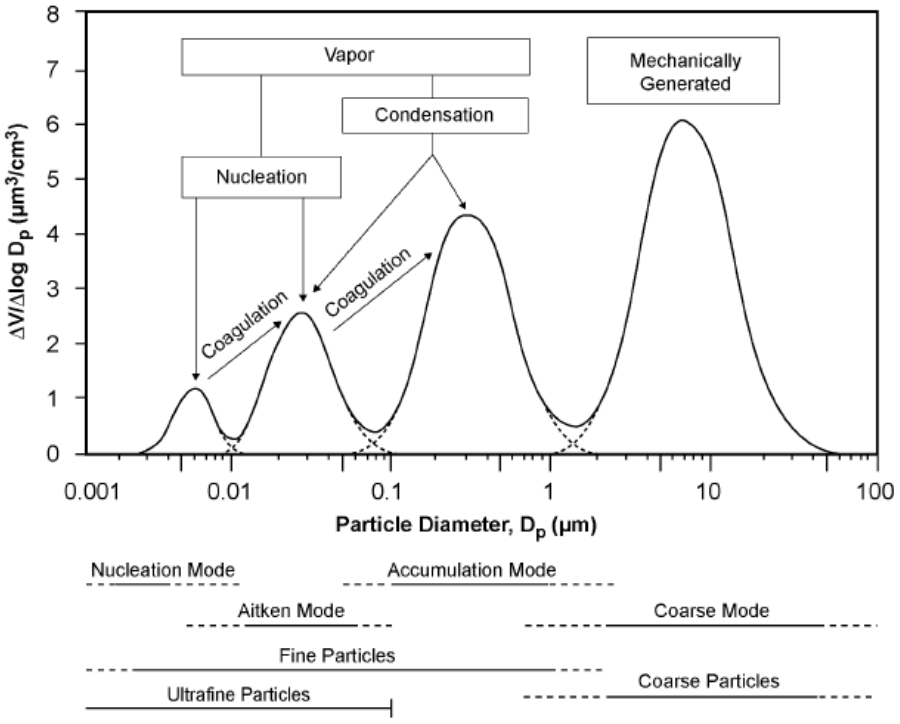

Figure 1.2: Example of volume size distrbution; main formation and growth mechanisms are also reported [12].

Atmospheric aerosol size distribution can be represented by the sum of log-normal distributions, each associated to specific formation, transformation, and deposition processes (see Figure 1.2). The analytical log-normal function is defined as [10]:

$$\frac{dN}{d\ln d_p} = \frac{N}{\ln \sigma_g \sqrt{2\pi}} \exp\left[-\frac{1}{2}\left(\frac{\ln d_p - \ln \overline{d_g}}{\ln \sigma_g}\right)^2\right] \tag{1.1}$$

where N is total particle number (in m^{-3}), d_p is the particle diameter, $\overline{d_g}$ is the geometric mean diameter, and σ_g id the geometric standard deviation.
The first detailed analysis of atmospheric aerosol size distribution was done by Whitby [13]. He observed that aerosol size distributions were typically characterised by three peaks that he called modes. Thanks to progresses in measurement techniques, observations later showed a fourth smaller peak.
Depending on particle size, atmospheric aerosol can be classified according to different conventions: major classifications (briefly described in the following) are based on:

modes; sampler cut-point; dosimetry or occupational health.
The *modal classification* [2] ideally divides aerosol particles according to the modal structure of their size distribution, as listed below:

- nucleation mode comprises particles with a diameter of about 10 nm; they are formed by nucleation processes from low-volatility vapours and are rapidly removed by coagulation (originating bigger particles);

- Aitken mode: particles belonging to this mode have diameters in the range 0.01-0.1 μm, mainly produced by high temperature combustion and coagulation of smaller particles; they are subject to Brownian diffusion and are removed by coagulation;

- accumulation mode: particles with diameters in the interval 0.1-1 μm are assigned to this mode. Typical formation processes are combustion, coagulation, and chemical reactions, whereas rain-out and wash-out are common removal pathways in this size range. Accumulation mode is usually divided into two submodes: the condensation mode, containing particles growing for condensation, and the droplet mode, with particles that grow hygroscopically.

- coarse mode: this mode is formed by particles with diameter larger than 1 μm, typically with natural origin and mechanically generated. These particles experience negligible diffusion and, due to their higher weight, the removal takes place mainly by gravitational settling.

Classification based on *cut-points* arises from the sampling of aerosol in a specific size range. Size-selective aerosol samplers are characterised by their 50% cut point size, i.e. the aerodynamic diameter (in μm) at which half of the particles penetrate and the remaining half is rejected. These samplers are commonly used for research and monitoring purposes, and the aerosol size fractions sampled are named PM_x, where "x" is the maximum aerodynamic diameter of considered aerosol population. Following European air quality standards, regulated aerosol fractions are $PM_{2.5}$, i.e. particles with $d_{ae} < 2.5\,\mu$m, and PM_{10}, i.e. the fraction of particles with $d_{ae} < 10\,\mu$m. In this work, $PM_{2.5}$ will be also referred to as *fine* aerosol fraction, whereas the difference between PM_{10} and $PM_{2.5}$ will be called *coarse* fraction.
Finally, atmospheric aerosol can be classified according to its *dosimetry or occupational health*. Depending on particle size, aerosol can penetrate human respiratory tract with smaller or larger efficiency [14, 9]. In particular, PM can be divided in three size fractions [15]: inhalable (entering the upper respiratory tract), thoracic (travelling past the larynx to the lungs), and respirable (reaching the alveoli, i.e. the gas exchange region).

Atmospheric aerosol is known to have effects on air quality and human health. Atmospheric particles exposure has been linked to both long-term and short-term biological effects: several epidemiological and toxicological studies (e.g. [16, 17]) are being carried out over the last years to assess aerosol health implications and their dependence on particle size and chemical composition. In 2013, the World Health Organization (WHO) declared PM carcinogenic to humans. Nevertheless, no consensus in the scientific community about which aerosol property (mass, size, number, surface area, composition, etc.) or which component is responsible for adverse health effects has been found yet [5].
Moreover, atmospheric aerosol has also implications on Earth energy balance and visibility: these effects will be briefly described in sub-sections 1.3.1 and 1.3.2.

1.2 Optical properties of atmospheric aerosol

The focus of this work is on atmospheric aerosol optical properties: visible radiation (commonly called light) is the part of the electromagnetic spectrum that is of interest, and a description of how it interacts with particles is given.
Light is considered as a superposition of electromagnetic waves, with electric and magnetic fields always perpendicular one another and perpendicular to the direction of propagation of the wave. To describe light interactions with particles, it is convenient to use the electric component.
Main properties of light are its *wavelength* λ and its *intensity* I (i.e. the rate at which electromagnetic energy is transferred across a unit surface perpendicular to the direction of propagation). Another important property, which is involved in the interaction with aerosol particles, is the *polarisation*. It is the given by the directions of oscillation of the electric waves: when they are randomly oriented, light is unpolarised (it is the case of sunlight); when electric waves oscillate in one direction, light is said to be linearly polarised; finally, when the electric vector rotates in a circle it is circularly polarised. A combination of linear and circular polarisation is called elliptical polarisation [10].

1.2.1 Scattering and absorption of light by a small particle

When a light beam of a given intensity I_0 impinges on an aerosol particle, it excites its electric charges so that they oscillate. If a detector is placed downstream, the power it receives is larger when the particle is removed: the presence of the particle results in *extinction* of the incident beam [18]. This phenomenon is caused by two processes arising from the interaction of radiation with the particle: excited charges reirradiate energy in all directions (*scattering*) and convert part of the incoming electromagnetic

energy to thermal energy (*absorption*). For energy conservation law, the rate at which energy is extinct (extinct power W_{ext}) is equal to the sum of scattered and absorbed power. The ratio W_{ext}/I_0 is a quantity with dimensions of an area (m^2) called *extinction cross section* C_{ext}; the same holds for scattering and absorption, therefore:

$$C_{ext} = C_{sca} + C_{abs} \tag{1.2}$$

To describe aerosol optical properties, another commonly used quantity is the *extinction efficiency*, i.e. the ratio between the extinction cross section and the particle cross-sectional area projected onto a plane perpendicular to the incident beam, G. For spherical particles of radius r_p, $G = \pi r_p^2$, therefore we have

$$Q_{ext} = \frac{C_{ext}}{G} \overset{spherical\,particle}{=} \frac{C_{ext}}{\pi r_p^2} \tag{1.3}$$

Similar relations hold for scattering and absorption.
The fraction of light extinction that is scattered is called *single scattering albedo*:

$$\omega = \frac{C_{sca}}{C_{ext}} = \frac{C_{sca}}{C_{sca} + C_{abs}} \tag{1.4}$$

(thus the *single scattering co-albedo* $1 - \omega$ is the fraction of light extinction that is absorbed). An analogous quantity can be calculated for a particle ensemble, as explained in sub-section 1.2.2.
In general, light extinction depends on: the chemical composition of the particle and the surrounding medium, particle size, the wavelength and the polarisation state of the incident light, the shape of the particle [18]. Since the analytical solution of the problem of the interaction of light with a particle is very complex, in this sub-section, a linearly polarised plane electromagnetic wave incident on a spherical particle is assumed. It will be shown in sub-section 2.3.4 that it is also possible to calculate scattering and absorption cross sections for particles of arbitrary shape. With the mentioned simplifications, fundamental parameters regulating scattering and absorption by a particle are:

- **wavelength** λ of the impinging radiation;
- **size** (i.e. particle diameter d_p), that is usually included in the so-called *size parameter* (adimensonal) $x = \pi d_p/\lambda$;
- **complex refractive index** $\alpha = n - ik$, where both terms (real part n and imaginary part k) are function of the wavelength; the real and imaginary parts at first order approximation are related to the non absorbing and absorbing behaviour of a particle, respectively [19]. It is common to use a refractive index

normalised to the one (α_0) of the mean in which the particle is contained: for atmospheric aerosol, α_0 is air refractive index; since $\alpha_{0,air} = 1.00029 - 0i \approx 1 - 0i$ at λ=589 nm, in most applications the effect of the normalisation is negligible. Table 1.2, reports complex refractive indices of some atmospheric components at the wavelength 589 nm.

Table 1.2: Complex refractive indices (at λ=589 nm) of some atmospheric components (adapted from Seinfeld and Pandis [8]).

Substance	n	k	
Water	1.333	0	
NaCl	1.544	0	
H_2SO_4	1.426	0	
NH_4HSO_4	1.473	0	
$(NH_4)_2SO_4$	1.521	0	
$Si0_2$	1.55	0	(λ=550 nm)
Carbon	1.96	0.66	(λ=550 nm)
Mineral dust	1.56	0.006	(λ=550 nm)

The theory that solves the classical problem of the interaction of light with a spherical particle is the Mie-Debye-Lorentz theory [18] (hereafter called Mie theory). It describes scattering and absorption by a particle of arbitrary size (i.e. x) and composition (i.e. α) expanding the electromagnetic field inside and outside the particle in vector spherical harmonics and then solving Maxwell's equations with appropriate boundary conditions. The Mie theory gives a complete picture of the phenomena arising from the interaction of radiation with a particle. An extensive discussion of the possible solutions is reported e.g. in Bohren and Huffman (1983) [18]. In the following, major results (and those that are relevant for this work) are explained.
The *scattering angle* θ is the angle between the direction of the incident beam and the direction of the scattered light; it is measured on the scattering plane defined by the incident and scattered beam themselves. Depending on θ, two scattering hemispheres are conventionally defined: the *forward* and the *backward*, including θ in the ranges 0-90° and 90-180°, respectively. Figure 1.3 represents the scattering plane, the scattering angle, and the polarised components of scattered light (P_1 is perpendicular and P_2 is parallel to the scattering plane). At a given wavelength, Mie theory retrieves the angular distribution of light scattered by a particle, called *scattering phase function* $P(\theta)$. It represents the scattered intensity $I_{sca}(\theta)$ at specific angle normalised by the integral of the scattered intensities at all angles in the scattering plane [8]; it depends on θ, x,

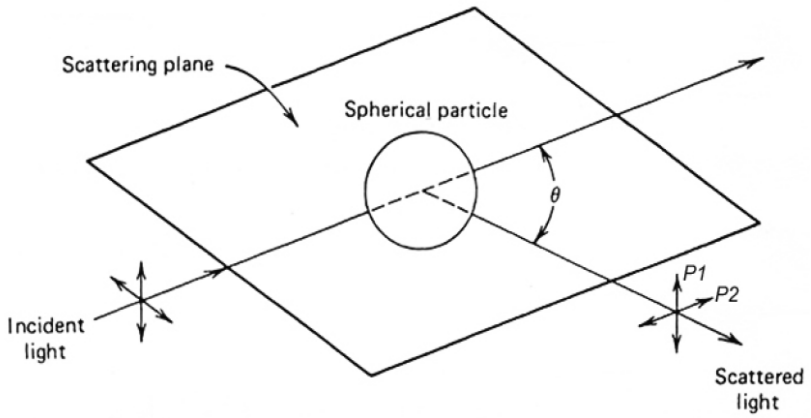

Figure 1.3: Scheme of the scattering plane, scattering angle, and polarised components of the scattered light [10].

and α (the dependence on the azimuthal angle ϕ is removed due to the assumption of spherical particle): for sake of simplicity, only the scattering angle dependence will be indicated in the following.

$$P(\theta) = 2\frac{I_{sca}(\theta)}{\int_0^\pi I_{sca}(\theta)\sin\theta\, d\theta} \tag{1.5}$$

The scattering phase function is normalised so that its integral over the unit sphere centered on the particle is 4π:

$$\int_0^{2\pi}\int_0^\pi P(\theta)\sin\theta\, d\theta\, d\phi = 4\pi \tag{1.6}$$

$P(\theta)$ can also be defined in terms of the *differential scattering cross section* $dC_{sca}/d\Omega$, i.e. the amount of light (per unit incident intensity) scattered into a unit solid angle $d\Omega = \sin\theta\, d\theta\, d\phi$ [18]:

$$\frac{dC_{sca}}{d\Omega} = \frac{C_{sca}}{4\pi}P(\theta) \tag{1.7}$$

The scattering phase function is used to derive other parameters depending on the angular distribution of scattered light, that are useful especially as inputs for models estimating atmospheric aerosol climate effects (briefly described in sub-section 1.3.1). The *asymmetry parameter* is defined as the intensity-weighed average of the cosine of the scattering angle [8]:

$$g = \frac{1}{2}\frac{\int_0^\pi \cos\theta I_{sca}(\theta)\sin\theta\, d\theta}{\int_0^\pi I_{sca}(\theta)\sin\theta\, d\theta} = \frac{1}{2}\int_0^\pi \cos\theta P(\theta)\sin\theta\, d\theta \tag{1.8}$$

where $1/2$ is a normalisation factor. Positive values of g indicate that light is scattered mainly in the forward hemisphere, while negative values represent light scattered mainly backward; $g = 1$ for radiation scattered totally forward, $g = -1$ for radiation

scattered totally backward, and $g = 0$ for radiation isotropically scattered.
Another relevant parameter is the *hemispheric backscatter ratio* (or simply backscatter ratio), which is the fraction of light scattered in the backward hemisphere compared to total scattered light:

$$b = \frac{\int_{\pi}^{\pi/2} P(\theta) \sin\theta \, d\theta}{\int_{0}^{\pi} P(\theta) \sin\theta \, d\theta} \tag{1.9}$$

The backscatter ratio can be measured directly with an instrument such as the Nephelometer (see sub-section 2.1.1), while the asymmetry parameter requires the measurement of the whole phase function, although some studies (e.g. [20, 21]) found out a one-to-one empirical relationship between b and g, allowing the retrieval of g from b measurements.
Mie theory gives exact solutions for the scattering and extinction cross sections [18]:

$$C_{sca}(\alpha, x) = \frac{2}{x^2} \sum_{j=1}^{\infty} (2j+1) \left[|a_j|^2 + |b_j|^2 \right] \tag{1.10}$$

$$C_{ext}(\alpha, x) = \frac{2}{x^2} \sum_{j=1}^{\infty} (2j+1) \Re \left({a_j}^2 + {b_j}^2 \right) \tag{1.11}$$

where a_j and b_j are the coefficients of the scattered field ($y = x\alpha$):

$$a_j = \frac{x\psi_j'(y)\psi_j(x) - y\psi_j'(x)\psi_j(y)}{x\psi_j'(y)\zeta_j(x) - y\zeta_j'(x)\psi_j(y)}$$

$$b_j = \frac{y\psi_j'(y)\psi_j(x) - x\psi_j'(x)\psi_j(y)}{y\psi_j'(y)\zeta_j(x) - x\zeta_j'(x)\psi_j(y)}$$

The functions $\psi(z)$ and $\zeta(z)$ are the Riccati-Bessel functions.
Depending on the size parameter x, three light scattering regimes can be identified:

- Rayleigh scattering: the particle is very small compared with the wavelength of incident light ($x \ll 1$);
- Mie scattering: particle size and wavelength of incident radiation are comparable ($x \simeq 1$);
- Geometric scattering: the particle is large compared with the wavelength ($x \gg 1$).

Rayleigh scattering

In the Rayleigh scattering regime (for instance, when $d_p < 0.1\,\mu$m in the visible range), it is possible to give an approximate solution of the scattering problem. In this regime the angular distribution of scattered light is symmetrical in the forward and backward hemispheres (see Figure 1.4) and more or less independent of particle shape [8].

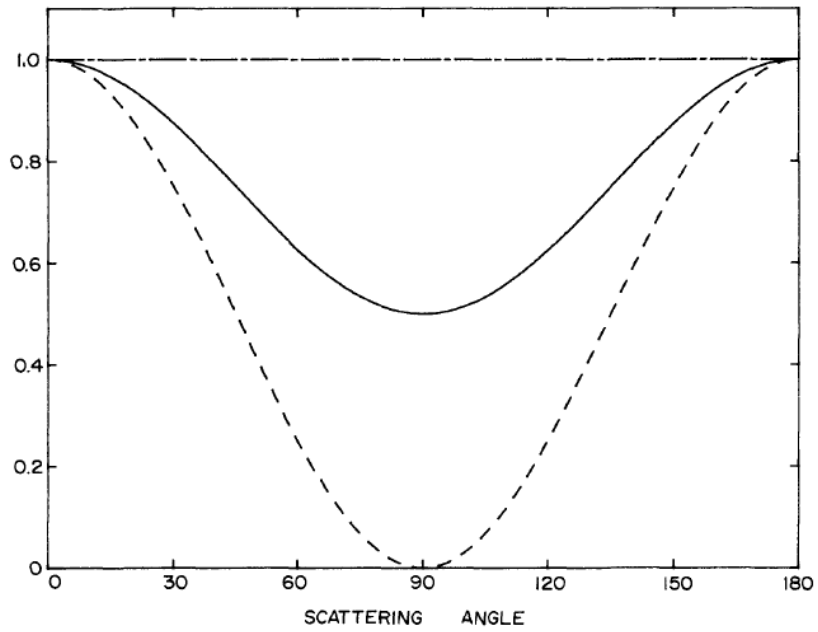

Figure 1.4: Normalised angular distribution of the light scattered by a sphere small compared with the wavelength for incident light polarised parallel (dashed line) and perpendicular (dashed-dotted line) to the scattering plane, and for unpolarised incident light (solid line) [18].

In the Rayleigh regime the scattered intensity at a given scattering angle and a distance R from a particle with diameter d_p is [18]:

$$I_{sca}(\theta) = \frac{\lambda^2}{8\pi^2 R^2} \left(\frac{\pi d_p}{\lambda}\right)^6 \left|\frac{\alpha^2 - 1}{\alpha^2 + 2}\right| \left(1 + \cos^2\theta\right) I_0 \tag{1.12}$$

$I_{sca}(\theta)$ is the sum of a circular component independent of θ, polarised perpendicular to the scattering plane, and of a component proportional to $\cos^2\theta$, polarised parallel to the scattering plane. In case the term $|(\alpha^2 - 1)\,/\,(\alpha^2 + 2)|$ is weakly dependent on the wavelength, the intensity of light scattered by a particle small compared with the wavelength is proportional to $1/\lambda^4$, a behaviour often called *Rayleigh scattering*. This explains, for example, the blue appearance of a clear sky, where sunlight is mainly scattered by the small air molecules.
The single-particle scattering and absorption efficiencies in the Rayleigh regime are [18]:

$$Q_{sca} = \frac{8}{3} x^4 \left|\frac{\alpha^2 - 1}{\alpha^2 + 2}\right|^2 \tag{1.13}$$

$$Q_{abs} = 4x\Im\left(\frac{\alpha^2 - 1}{\alpha^2 + 2}\right) \tag{1.14}$$

and since in this regime $x \ll 1$, $Q_{abs} > Q_{sca}$. To summarise, in the Rayleigh regime, if the particle refractive index does not strongly depend on the wavelength, the wave-

length dependencies of the scattering and absorption efficiencies are

$$Q_{sca} \approx \lambda^{-4} \tag{1.15}$$

$$Q_{abs} \approx \lambda^{-1} \tag{1.16}$$

Mie scattering

For a particle with size comparable with the wavelength of the incident light, no simplifications can be made to solve the problem: therefore, the exact solutions of Maxwell's equations must be found to compute the scattering (Eq. 1.10), absorption, and extinction (Eq. 1.11) cross sections and efficiencies.

The scattered intensity at a given angle θ and a distance R from a particle on which unpolarised light of intensity I_0 impinges is given by:

$$I_{sca}(\theta) = \frac{\lambda^2}{8\pi^2 R^2} (i_1 + i_2) I_0 \tag{1.17}$$

where i_1 and i_2 are Mie intensity parameters for light scattered with perpendicular and parallel polarisation to the scattering plane, respectively [10]. An example of Mie intensity parameters calculated for a water droplet (α=1.33) with size parameters 0.8, 2.0 and 10.0 is given in Figure 1.5.

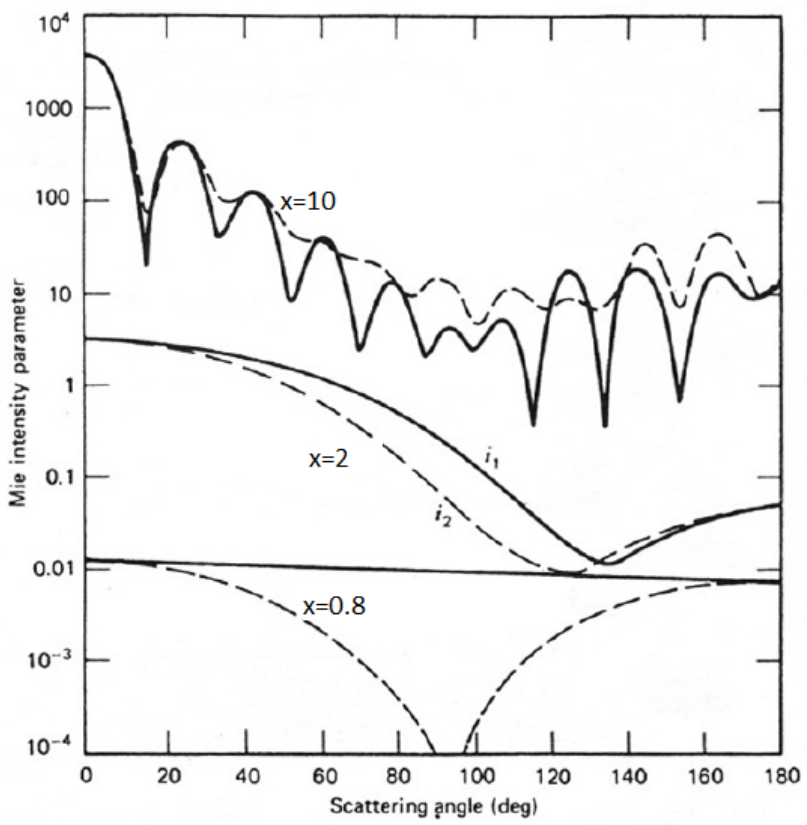

Figure 1.5: Mie intensity parameters i_1 (solid lines) and i_2 (dashed lines) for a water droplet with α = 1.33 and x=0.8, 2.0, and 10.0, as a function of the scattering angle (adapted from Hinds, 2006 [10]).

Major features observed in Figure 1.5 are that the importance of forward scattering compared to backward scattering increases as particles become larger, and that the bigger the particle is, the more complicated the scattering pattern becomes. Note that non-spherical particles generally show a smoother behaviour [10].

Geometric scattering

When particle size is much larger that the wavelength of the incoming light (i.e. for $x \gg 1$), its optical properties can be described using geometric optics principles of reflection, refraction, and diffraction. With these laws, the obtained absorption efficiency for a weakly absorbing sphere is [8]:

$$Q_{abs} = \frac{8}{3} x \frac{k}{n} \left[n^3 - \left(n^2 - 1 \right)^{3/2} \right] \tag{1.18}$$

When observing the extinction efficiency as a function of the particle size at a fixed wavelength, it can be noted that $\lim_{x \to \infty} Q_{ext}(x, \alpha) = 2$, which is twice as large as the one predicted by geometric optics. This result is called "extinction paradox" [18] and arises from the failure of geometric optics in the neighbourhood of the particle edge. Indeed, geometric optics is a good approximation for large objects, but it does not consider that, no matter how large the object is, it still has an edge. Qualitatively, the incident wave is influenced beyond the physical borders of the obstacle: the edge of the sphere deflects in its neighbourhood rays that, from the point of view of geometric optics, would have passed unimpeded. These rays are counted as having been removed from the incident beam and therefore they contribute to total extinction.

1.2.2 Optical properties of an ensemble of particles

A rigorous treatment of the scattering and absorption of light by an ensemble of particles is complicated. Nevertheless, the simpler single-particle scattering theory can be used if the average distance between particles is larger than the size of the particles themselves. This condition is generally fulfilled, in real ambient conditions, even when atmospheric aerosol concentration is very high [8]. In this case, the total scattering (absorption) intensity is computed as the sum of intensities scattered (absorbed) by each individual particle (denoted by the index j):

$$I_{sca} = \sum_j I_{sca,j} \tag{1.19}$$

For sake of simplicity, the treatment in the following will concern only scattering. The same description and equations hold for extinction and absorption.

For an ensemble of n particles, the *scattering coefficient* σ_{sp} (unit: Mm^{-1}) is the sum of individual single-particle scattering cross sections $C_{sca,j}$ divided by the volume V (in

m^3) occupied by the particle ensemble. In the simplest case of identical particles, σ_{sp} is the particle number density $N = n/V$ (unit: m^{-3}) multiplied by the total absorption cross section C_{sca}.

$$\sigma_{sp} = \frac{\sum_{j=1}^{n} C_{sca,j}}{V} = NC_{sca} \tag{1.20}$$

From Equations 1.3 and 1.20, it follows that for a monodisperse ensemble of spherical particles with radius $r_p = d_p/2$:

$$\sigma_{sp} = NQ_{sca}\pi r_p^2 = NQ_{sca}\pi\frac{d_p^2}{4} \tag{1.21}$$

More generally, if the aerosol ensemble is characterised by a number size distribution $n(\log d_p) = dN/d\log d_p$ (see Section 1.1):

$$\sigma_{sp} = \int_{-\infty}^{\infty} Q_{sca}(d_p)\pi\frac{d_p^2}{4}\frac{dN}{d\log d_p}\,d\log d_p \tag{1.22}$$

The scattering coefficient can be also written in terms of the *differential scattering coefficient*, also called *volume scattering function* $\gamma(\theta)$, as:

$$\sigma_{sp} = 2\pi\int_0^{\pi}\gamma(\theta)\sin\theta\,d\theta \tag{1.23}$$

Similar relations hold for extinction and absorption coefficients.
From Equations 1.22, 1.23 and 1.7, given that $C_{sca} = Q_{sca}\pi\frac{d_p^2}{4}$, it follows:

$$\gamma(\theta) = \int_{-\infty}^{\infty}\frac{d_p^2}{4}\frac{Q_{sca}(d_p)\pi}{4\pi}P(\theta)\frac{dN}{d\log d_p}\,d\log d_p \tag{1.24}$$

Likewise efficiencies and cross sections, the extinction coefficient is the sum of scattering and absorption coefficients:

$$\sigma_{ep} = \sigma_{sp} + \sigma_{ap} \tag{1.25}$$

Moreover, similarly to the single particle case, other important parameters to describe an aerosol population are the *single scattering albedo* (SSA) ω for an ensemble of particles:

$$\omega = \frac{\sigma_{sp}}{\sigma_{ep}} \tag{1.26}$$

and its complementary, the *single scattering co-albedo* (SSCA) $\bar{\omega}$:

$$\bar{\omega} = 1 - \omega = \frac{\sigma_{ap}}{\sigma_{ep}} \tag{1.27}$$

In the atmosphere, aerosol is always embedded in the surrounding medium (the air): similarly to particles, gaseous compounds are responsible for light extinction. Therefore, the total atmospheric light extinction is:

$$\sigma_{ext} = (\sigma_{sp} + \sigma_{sg}) + (\sigma_{ap} + \sigma_{ag}) = \sigma_{sca} + \sigma_{abs} \tag{1.28}$$

where σ_{sg} is the scattering coefficient due to gases (often called Rayleigh scattering - see sub-section 2.3.1) and σ_{ag} is the absorption coefficient due to gases.

Wavelength dependence

Although not always explicitly indicated, all optical properties are dependent on the wavelength of the incident radiation. The wavelength dependencies of some of the optical parameters defined are important to identify specific aerosol features (see subsection 3.1.2). Extinction, scattering, and absorption coefficients generally depend on λ following a power law, where the exponents are called Extinction, Scattering, and Absorption Ångström Exponents, respectively: EAE , SAE, and AAE; for instance, $\sigma_{ep} \approx \lambda^{-EAE}$. Therefore, considering a wavelength pair (it is the case of multi-wavelength optical measurements), it follows (for extinction):

$$\frac{\sigma_{ep}(\lambda_1)}{\sigma_{ep}(\lambda_2)} = \left(\frac{\lambda_1}{\lambda_2}\right)^{-EAE} \tag{1.29}$$

where $\lambda_1 < \lambda_2$; the Extinction Ångström Exponent EAE can be calculated as:

$$EAE = -\frac{\ln\left(\sigma_{ep}(\lambda_1)/\sigma_{ep}(\lambda_2)\right)}{\ln\left(\lambda_1/\lambda_2\right)} \tag{1.30}$$

From Equations 1.26 and 1.27, it can be derived that

$$\omega = \frac{\sigma_{sp}}{\sigma_{ep}} \approx \frac{\lambda^{-SAE}}{\lambda^{-EAE}} = \lambda^{-(SAE-EAE)} \tag{1.31}$$

$$1-\omega = \frac{\sigma_{ap}}{\sigma_{ep}} \approx \frac{\lambda^{-AAE}}{\lambda^{-EAE}} = \lambda^{-(AAE-EAE)} \tag{1.32}$$

Therefore, the wavelength dependencies of single scattering albedo and co-albedo for a wavelength pair (λ_1, λ_2) are defined as:

$$SSAAE\left(\lambda_1, \lambda_2\right) = SAE\left(\lambda_1, \lambda_2\right) - EAE\left(\lambda_1, \lambda_2\right) \tag{1.33}$$

$$SSCAAE\left(\lambda_1, \lambda_2\right) = AAE\left(\lambda_1, \lambda_2\right) - EAE\left(\lambda_1, \lambda_2\right) \tag{1.34}$$

Mixing state

Atmospheric aerosol optical properties strongly depend on how absorbing and scattering components are distributed in the particles themselves (i.e. the *mixing state*) as shown in Figure 1.6. In particular:

- **external mixing** represents an ensemble of homogeneous particles, in which the absorbing and the scattering components are separated in different particles (and only the first type contributes to k);
- **internal mixing** represents the co-existence of both absorbing and scattering components in the same particle: in this case, all particles contribute to both n and k. The most simplified models for internal mixing are:
  - *volume* internal mixing: absorbing and scattering components are assumed to be perfectly mixed inside the particles (which appear homogeneous);

– *core-shell* internal mixing: particles are formed by a core of one chemical species surrounded by a shell of another species; for instance, this is the case of a Black Carbon (BC) particle coated by purely scattering material. Such a mixing state can strongly influence optical properties of the particle: indeed, the scattering shell can enhance the absorption by the carbonaceous core deviating part of the incident radiation towards the absorbing nucleus (this phenomenon is known as *lensing effect* [22, 23]).

For internal mixing state, the complex refractive index of the particle ensemble can be calculated with different *mixing rules* (examples can be found in Bond and Bergstrom [24]). The simplest one is the linear mixing that, assuming a volume mixing state, infers the real and imaginary parts of the refractive index as the linear average of n and k of each component weighed on their volume fractions.

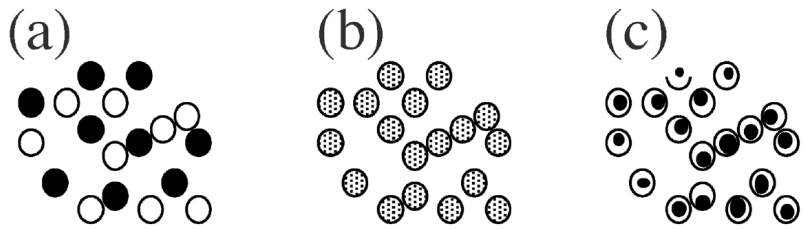

Figure 1.6: Types of aerosol mixing states: (a) external mixing, (b) volume internal mixing, (c) core-shell internal mixing [24].

In the majority of models the properties of a particle ensemble are computed as the sum of the properties of each aerosol type comprised in the ensemble. This is a crucial assumption influencing the results of algorithms inferring optical properties of a particle ensemble: this needs to be taken into account when interpreting results themselves.

1.3 Effects of atmospheric aerosol related to optical properties

Aerosol optical properties have effects both at global scale on the Earth radiation balance and at local scale on visibility, as described in the following sub-sections.

1.3.1 Effects on the Earth radiation balance

The effect of atmospheric components on the Earth radiation balance (reported in Figure 1.7) is quantified by the Radiative Forcing (RF), defined as the net change in

the energy balance of the Earth system in response to an external perturbation [25]; positive RF leads to a warming effect, while negative RF to a cooling one. Moreover, the recently introduced Effective Radiative Forcing (ERF) takes into account rapid adjustments to perturbations.

Atmospheric aerosol affects the Earth radiation balance both directly (via scattering and absorption of radiation - see Section 1.2) and indirectly (acting as cloud condensation nuclei - CCN - and ice nuclei - IN - with impacts on cloud albedo and lifetime). These effects on RF are called RF_{ARI} (Aerosol-Radiation Interaction) and RF_{ACI} (Aerosol-Cloud Interaction), respectively. Figure 1.7 highlights that atmospheric aerosol is a significant contributor to RF: indeed, only major greenhouse gases such as CO_2 and CH_4 are more important. Nevertheless, it is noteworthy that the estimate of RF due to aerosol and its precursors is still affected by a large uncertainty (comparable with the RF itself); moreover, the net effect (warming or cooling) has not been assessed yet.

In this work, the focus is on the interaction of atmospheric aerosol with radiation, via the experimental and modelling analysis of aerosol optical properties (described in Section 1.2).

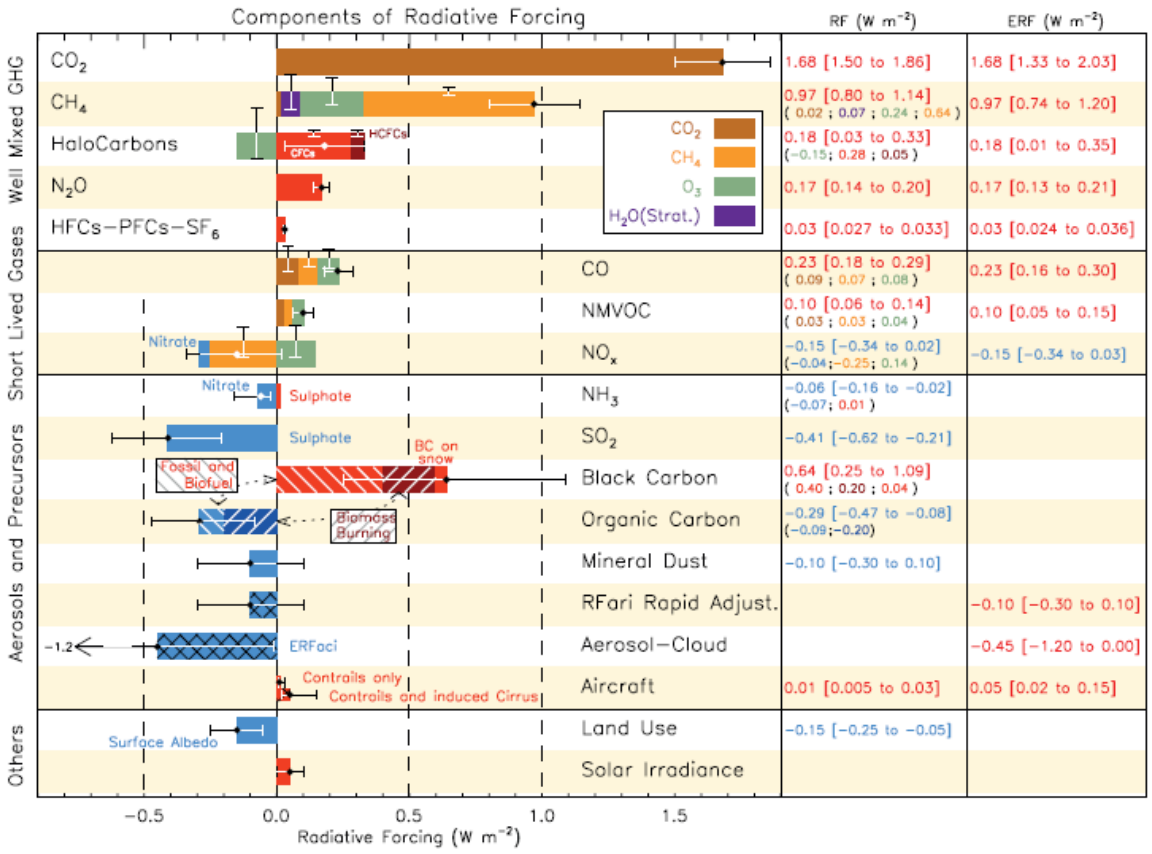

Figure 1.7: Radiative forcing during the industrial Era shown by emitted components from 1750 to 2011 [25].

1.3.2 Visibility

Visibility impairment is likely the most readily perceived effect of air pollution. Being subjective, visibility has no precise scientific definition. It is due to the interaction of light with the atmosphere, to the human eye sensitivity and to the interpretation of its signals by the brain [26]; the eye-brain system distinguishes two objects by their contrast. Visibility is generally defined as the maximum distance at which a suitably large black object can be distinguished against the horizon [27].
Several factors determine visibility, including atmospheric optical properties, the amount and distribution of light, the characteristics of the observed object and those of the human eye. Visibility reduction is due to scattering and absorption by both aerosol particles and atmospheric gases, even though aerosol light scattering is the main responsible phenomenon [8].
In order to study the effect of atmospheric components on visibility, the case of a black object observed against a background is considered. The visual contrast at a distance y from the object is defined as the relative difference between the intensity of the background (I_B) and the one of the object (I):

$$C_V(y) = \frac{I_B(y) - I(y)}{I_B(y)} \tag{1.35}$$

It follows that $C_V(0) = 1$: at the object $I(0) = 0$, since the object is assumed to be black and thus it absorbs all the light incident on it. At a given distance y, $I(y)$ is due to two phenomena [8]: light absorption by aerosol and gases and the addition of light scattered into the line of sight; indeed, scattered light is not lost from the system (it is not the case for absorbed light) and can contribute to observed intensity due to multiple scattering. The intensity of the object follows the Beer-Lambert law $dI(y) = -\sigma_{ext} dy$, while $dI_B(y) = 0$ by definition. Therefore, also $C_V(y)$ follows the Beer-Lambert law, that gives (via integration over the distance):

$$C_V(y) = \exp\left(-\sigma_{ext} y\right) \tag{1.36}$$

The minimum perceivable brightness contrast is called the *threshold contrast* [8], whose value is generally agreed to be 0.02 for typical daylight conditions. The distance y at which the visual contrast equals the threshold contrast is called *visual range* VR:

$$VR = \frac{-\ln(0.02)}{\sigma_{ext}} = \frac{3.912}{\sigma_{ext}} \tag{1.37}$$

Equation 1.37 is commonly called *Koschmieder equation* [28]: it can be used to estimate visibility from σ_{ext} or viceversa.
In Section 2.3 a method to evaluate light extinction and visibility using atmospheric chemical speciation data is presented.

Chapter 2

Methodologies

Introduction

In this thesis, on-line and off-line instrumentation was employed to investigate aerosol optical properties. All instruments, both in-situ and filter-based, need corrections to account for the effects of e.g. non-idealities in the set-up, assumptions in the measurement principle and retrieval algorithm, and the collection of suspended particles on a filter matrix. Moreover, aerosol properties could impact on their measurements. In this work, several approaches were developed and exploited to investigate biases affecting outputs of widespread instrumentation and to optimise both experimental methodologies and algorithms based on measured data.

2.1 On-line instrumentation

Several in-situ and filter-based on-line instruments have been developed in the last decades to measure aerosol optical properties. In the following sub-sections, brief descriptions of those used in this PhD work are given.

2.1.1 In-situ instruments

In-situ instrumentation measures properties of aerosol particles suspended in the air. These techniques are often preferred since aerosol is not altered by the deposition on a filter matrix, and because they usually perform measurements at high time resolution. Nevertheless, in-situ instruments generally have higher Limits of Detection (LOD) compared to filter-based ones [29]. In the following paragraphs, two in-situ instruments used to retrieve aerosol extinction and scattering coefficients are introduced.

CAPS PM_{SSA}

The Cavity Attenuated Phase Shift - Single Scattering Albedo Monitor CAPS PM_{SSA}

(Aerodyne) [30] simultaneously measures aerosol extinction and scattering coefficients at one wavelength, hence allowing for a direct retrieval of the Single-Scattering Albedo SSA (i.e. the ratio between the scattering and the extinction coefficients - see Section 1.2).
Light source used in the CAPS PM_{SSA} is a LED. To measure the extinction coefficient σ_{ep}, the phase shift between the input square wave modulated light and the output distorted waveform caused by the presence of particles is exploited, since it is only a function of instrument fixed properties and σ_{ep}. The measurement cell incorporates two high reflectivity mirrors (reflectivity R $\gg$ 0.9999) centered at the wavelength of the LED, thus providing a long effective optical path. Conversely, the scattering measurement is performed via an integrating sphere [31] incorporated into the optical cell.
More details about this instrument can be found in Onasch et al. [30].

Integrating Nephelometer
The integrating Nephelometer [32] is an instrument used to measure aerosol scattering coefficient σ_{sp}. It is equipped with a near-Lambertian light source illuminating the measurement cell that contains aerosol particles in air; light scattered in a wide range of scattering angles (from about 10° to about 170° depending on the model) is detected by a photomultiplier orthogonal to the light source. In addition, a shutter allows to measure radiation scattered in the backward hemisphere only, thus obtaining the backscattering coefficient.
Due to the instrument geometry, that prevents the detection of light scattered in the extreme forward and backward regions, the instrument output needs to be corrected for truncation error. Several correction schemes have been developed for different Nephelometer types and models (e.g. [33, 34, 35, 36]). In this work, a TSI and an Aurora 3000 (Ecotech) integrating Nephelometers were used, as described in the following. Moreover, the truncation correction of the polar Nephelometer Aurora 4000 (Ecotech) was investigated in a dedicated experiment (see sub-section 2.2.5).

2.1.2 Filter-based instruments

Filter-based methods are a commonly used alternative to in-situ techniques, especially for light absorption assessment. Aerosol particles are collected on-line on a filter matrix and the transmitted (or transmitted and scattered) light is simultaneously detected. These instruments typically show lower detection limits compared to in-situ ones, even though they need to be corrected for two major effects arising from the interaction of sampled particles with the filter matrix and among each other:

- *scattering effects*: since absorbing aerosol also scatters light, a cross-sensitivity

to particle-related scattering and multiple scattering caused by the filter matrix can bias σ_{ap} obtained by filter-based methods;

- *loading effect*: as aerosol particles are deposited on the filter, they "cast a shadow" over particles already sampled, leading to an underestimation of σ_{ap}.

Filter-based instruments mentioned in this thesis are briefly described in the following paragraphs.

MAAP

The Multi-Angle Absorption Photometer (MAAP [37], Thermo) is a filter-based instrument measuring aerosol absorption coefficient (σ_{ap}) at one wavelength (typically 637±2 nm [29]). Aerosol is continuously sampled on a filter tape and a light source (a LED or a laser) impinges perpendicularly on a loaded spot; three photodiodes simultaneously measure light transmitted (θ=0°) and scattered at two fixed scattering angles (130° and 165°). The retrieval of σ_{ap} is performed via a radiative transfer scheme that takes into account multiple scattering effects, thus limiting the cross-sensitivity of this technique to scattering contribution [38]. This radiative transfer model is described more in detail in sub-sections 2.2.1 and 2.2.2 and in Appendix A.

PSAP

The Particle Soot Absorption Photometer (PSAP, Radiance Research) is a filter-based instrument retrieving aerosol absorption coefficient σ_{ap} from the attenuation of light through a loaded filter spot compared to the one through a blank (reference) spot. The progressive reduction of light transmitted through the loaded spot as aerosol particles are sampled on it is related to σ_{ap} applying corrections to take into account scattering and loading effects. The former leads to an apparent aerosol absorption coefficient larger than the true one, and the latter causes a reduction of the optical path length (and of apparent absorption) (see e.g. [39, 40]).
The attenuation is obtained from the ratio of light intensity through the loaded spot I to the one (I_0) passing through the reference spot; taking into account the sampled spot area S and the flow rate F, the quantity measured by the PSAP in the time interval Δt is:

$$\sigma_{meas} = \frac{S}{F \cdot \Delta t} \cdot \ln\left(\frac{I(t)}{I(t+\Delta t)}\right) \tag{2.1}$$

The instrument output ($\sigma_{ap,PSAP}$) includes an empirical correction for loading effects [39], that depends on real-time transmission:

$$\sigma_{ap,PSAP} = f(T) \cdot \sigma_{meas} = (1.079 \cdot T + 0.71)^{-1} \cdot \sigma_{meas} \tag{2.2}$$

where the transmittance is defined as $T(t) = I(t)/I_0$.
In the PSAP, particles are sampled on a standard 47-mm diameter filter, that needs to be manually changed when the transmittance is below 0.7.
Several correction schemes have been developed for PSAP [39, 41, 42, 43, 44], based on the basic equation

$$\sigma_{ap,PSAP} = K_1 \cdot \sigma_{sp} + K_2 \cdot \sigma_{ap} \tag{2.3}$$

where K_1 and K_2 are empirical constants representing the cross-sensitivity to particle-related scattering and to multiple scattering, respectively.
Considering Equations 2.1, 2.2, and 2.3, the correction equation becomes

$$\sigma_{ap} = \frac{0.873}{K_2} \cdot f(T) \cdot \frac{S}{F \cdot \Delta t} \cdot \ln\left(\frac{I(t)}{I(t+\Delta t)}\right) - \frac{K_1}{K_2} \cdot \sigma_{sp} \tag{2.4}$$

The multiplicative factor of 0.873 was added to account for a mismatch between the filter spot area set in the PSAP and the one measured on the manufacturer's reference instrument [43].
If no simultaneous measurements of aerosol scattering coefficient are available, the second term in the second member of Equation 2.4 is neglected. The effect of this approximation on the retrieved σ_{ap} can not be estimated *a priori*, since it depends on the value of aerosol scattering coefficient.
The PSAP, originally operating at 567 nm, was recently equipped with 3 LEDs to perform multi-wavelength measurements. Note that the empirical constants in the PSAP correction schemes were derived at 550 nm and are usually applied at all operating λs; Virkkula et al. [41] compared σ_{ap} from PSAP and from a reference method and suggested that correction factors do not strongly depend on the wavelength.

TAP

The Tri-color Absorption Photometer (TAP, Brechtel) measures aerosol absorption coefficient at three wavelengths using the same principle as the PSAP. The main difference is that aerosol can be sampled on 8 different spots on the same 47-mm filter; the spot is automatically changed when a threshold attenuation value is reached. Moreover, 2 spots on the filter are used to sample particle-free air and are considered as reference spots.
Like all instruments based on the measurement of light transmission to retrieve the absorption, the TAP output needs to be corrected for biases arising from scattering and loading effects. In the TAP, the correction scheme described by Ogren [43] is typically used.

Aethalometer

The Aethalometer is based on a principle similar to the one used in the PSAP and in

the TAP. The major difference is that in the Aethalometer particles are sampled on a filter tape, on which the spot is automatically changed when the attenuation reaches a threshold value; this allows for an extended unattended operation time, making this instrument suitable for long-term monitoring.
This instrument was originally developed for broadband absorption using a white lamp; latest models perform multi-wavelength measurements and are equipped with LEDs at different λs (up to 7). Correction schemes and factors applied to Aethalometer outputs are described in detail in sub-section 2.2.4.

2.2 Methodological advancements

2.2.1 PP_UniMI set-up and measurement principle

The polar photometer developed by the Environmental Physics research group of the University of Milan (hereafter called PP_UniMI) is a home-made instrument for the off-line measurement of multi-wavelength absorption coefficient of aerosol samples collected on different supports. Figure 2.1 reports a scheme of PP_UniMI, that is thoroughly described in Vecchi et al. [45] and Bernardoni et al. [46]; its measurement principle is summarised in the following. For nomenclature about quantities related to aerosol optical properties see Section 1.2.

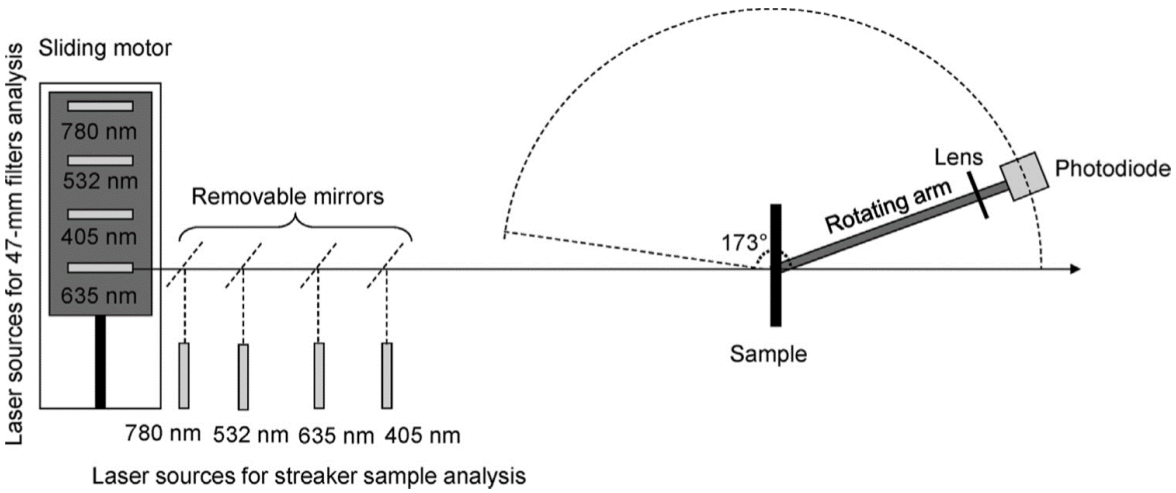

Figure 2.1: Scheme of the PP_UniMI. Photodiode acquisition occurs on the horizontal scattering plane [46].

A laser beam impinges (directly or after 90° reflection depending on the set-up used) perpendicularly on a filter so that the particle layer is hit first. Light scattered at scattering angles from 0° to 173° (with steps of about 0.4°) is continuously collected by a photodiode located on a rotating arm whose centre of rotation coincides with the centre of the sample. The analysis is performed at four wavelengths (405, 532,

635, 780 nm) making use of different laser diodes, and it is done both on the non-sampled (blank) and sampled filter. The laser intensities are monitored before and after each measurement session and values registered during the blank and sampled filter analyses are normalised to a reference value: this normalisation procedure allows to avoid biases arising from lasers instabilities, both long-term (estimated in the range 1-9% depending on the wavelength) and short-term (intra-day variability <1% at 405, 635, and 780 nm and of about 3% at 532 nm); the latter variations are accounted for in the measurement uncertainties [46]. Two set-ups are built in the system in order to perform measurements of both standard 47-mm diameter filters (or with lower diameter using filter holders made on purpose) of any material and type and of streaker samples collected at 1-h time resolution on specific supports [46]. Up to seven 47-mm filters can be placed in a rotating wheel mounted perpendicularly to the laser beam in order to automatise the analysis; the eighth hole in the wheel is usually occupied by a blank reference filter for stability checks. Conversely, streaker samples require a dedicated set-up and the whole support containing samples collected during one week is assembled in place of the filter-holder wheel. Hourly samples are very tiny streaks (1.25×8 mm^2) obtained via the 1.8°/h rotation of a cartridge and the streaker sampler: therefore, PP_UniMI laser beam (circular or elliptical shape, size up to 4.5 mm on the major axis) has to be collimated to allow for the analysis of these samples. A couple of lenses with proper focal lengths are employed to focus the beam, which is sent to the sample via removable mirrors. Indeed, in order to be able to quickly switch from one set-up to the other, laser diodes are always fixed as are the focusing lenses; each laser diode dedicated to streaker samples analysis is coupled with a pair of lenses, whose alignment and positioning are finely adjusted, that are located between the laser source and the mirror (see Figure 2.1)

The angular distributions of light transmitted and scattered by the blank and by the sampled filter are directly measured by PP_UniMI and employed to calculate integrals of the light scattered in the forward and in the backward hemispheres. In order to retrieve the aerosol absorption coefficient from these quantities, a radiative transfer model developed by Hänel [47] is used. This method is briefly described in the following; details about the calculations can be found in Appendix A.

The algorithm is based on a two-layer radiative transfer model that describes the interaction between particles and filter matrix taking into account multiple scattering effects typically occurring in case of filter-based optical measurements. This radiative transfer model allows to calculate the optical depth τ_p and the single scattering albedo ω_p for particles collected on a membrane filter, on which ideally the aerosol forms a surface layer. In the case of fibre filters, instead, particles can also penetrate the matrix up to a thickness of 10-15% of the whole filter (see Figure 2.2). For both filter types,

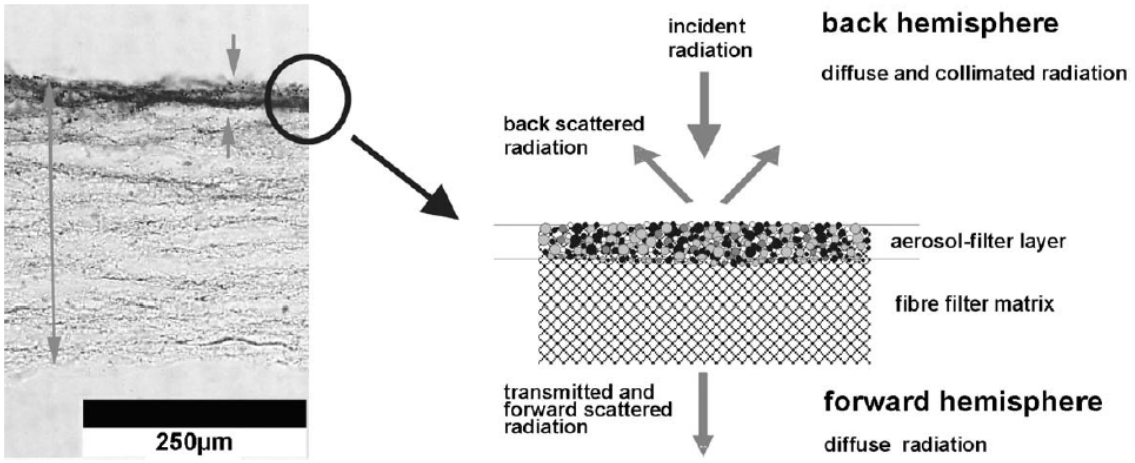

Figure 2.2: Microscopy image (left) and scheme of the two layers considered in the PP_UniMI retrieval algorithm (right) [37].

the matrix does not contribute to light absorption since its material is transparent to visible radiation [37]. The model by Hänel was generalised by Petzold and Schönlinner [37] to be applied also to optical measurements performed on fibre filters, for which the two layers are the so-called "aerosol-filter layer" and "particle-free filter matrix" (hereafter referred to as "filter layer" for sake of simplicity) (see Figure 2.2); in this case, the quantities τ_p and ω_p are those of the aerosol-filter layer.
Basically, the relevant radiative processes in the two-layer system are:

- interactions of light inside the aerosol-filter layer, described by a two-stream approximation model developed by Coakley and Chýlek [48];
- radiative interactions between particles and filter, described via the so-called adding method [47].

Interactions of light inside the filter matrix are not considered since optical properties of this layer are not affected by those of collected particles, hence remain unchanged after sampling [37]. Via the two-stream approximation and the adding method, the amounts of light forward transmitted and scattered in the two hemispheres for both blank and sampled filter are obtained. The only unknown quantity in the model (except for τ_p and ω_p) is the aerosol asymmetry parameter g, that has to be assumed. An average value (g=0.75) [37] is employed at all wavelengths and the fundamental equations of the algorithm are solved iteratively to finally derive $\omega_p(\lambda)$ and $\tau_p(\lambda)$. The combination of these two quantities is used to retrieve the absorbance at each of the operating wavelengths as:

$$ABS(\lambda) = (1 - \omega_p(\lambda)) \cdot \tau_p(\lambda) \tag{2.5}$$

The sensitivity of the model to variations of the assumed value of g have been tested, resulting ABS changes smaller than 10% at all wavelengths if g is reduced to 0.50 [49]. Limits of detection (LOD) for absorbance are estimated to be in the range 0.02-0.07 on 47-mm filters and 0.03-0.07 for streaker samples, depending on the wavelength. Uncertainties are ± 0.01 if $ABS < 0.1$ and 10% if $ABS \geq 0.1$ [46].
Finally, taking into account the sampled area A on the filter and the volume V of air sampled through it, the aerosol absoption coefficient is obtained as:

$$\sigma_{ap}(\lambda) = ABS(\lambda) \cdot \frac{A}{V} = ABS(\lambda) \cdot \frac{A}{F \cdot t} \tag{2.6}$$

where F is the volumetric flow rate and t is the sampling time.
It is noteworthy that optical measurements performed with PP_UniMI are non-destructive, therefore this analysis is always possible on filters to provide additional information, and it can be carried out on stored filters for retrospective analysis as well. Moreover, since the angular distribution of scattered light is directly measured and no assumptions on its shape are needed (see also sub-section 2.2.2), it can be applied on all kind of filters or supports, provided that they are not absorbing and not completely opaque.
Another home-made absorption photometer, based on a principle similar to the one of the MAAP as it measures light transmitted and scattered at fixed angles, is the 5-wavelength Multi-Wavelength Absorbance Analyzer (MWAA) developed at the Physics Department of the University of Genoa (Italy) [50]. This instrument was successfully employed for several applications and in different collaboration works (see e.g. [51, 52, 53]).

2.2.2 Inter-comparison experiment

In a previous work [45], the polar photometer PP_UniMI was validated at 635 nm for the analysis of samples collected on quartz-fibre filters against a Multi-Angle Absorption Photometer (MAAP, see Section 2.1), that is currently considered as the reference instrument for filter-based measurements of aerosol absorption coefficient [29]. It has to be noted that MAAP is a single wavelength (637±2 nm [29]) instrument, while PP_UniMI, originally developed with only one laser source (635 nm), operates at four λs (405, 532, 635, and 780 nm) [46].
During this PhD work, an inter-comparison exercise was performed in November 2018 in collaboration with the Jülich Forschungszentrum FZJ (Jülich - Germany) and the University of Genoa. A laboratory experiment was carried out at FZJ in order to compare the aerosol absorption coefficient (σ_{ap}) and its wavelength dependence (AAE) as measured by on-line instrumentation (both in-situ and filter-based) and retrieved by off-line PP_UniMI and MWAA analyses of samples of the same laboratory-generated

aerosol particles [113]. The inter-comparison was designed as a blind exercise in order to minimise biases: the experiment was carried out following procedures that had been agreed upon by the two research groups and only after all analyses completion, the results were compared. As for off-line analyses, only PP_UniMI results are reported in this thesis.

In-situ instrumentation has the advantage of providing very high-time resolved data (up to a few seconds), although often operating at only one wavelength, whereas filter-based techniques are more commonly used (for instance by monitoring networks) even though they usually need corrections for multiple scattering and loading effects (see sub-section 2.1.2). In particular, the latter category can be distinguished in two types of instruments: (1) polar photometers that retrieve the aerosol absorption coefficient by measuring light transmitted and scattered in the forward and in the backward hemispheres and exploiting radiative transfer models to account for multiple scattering effects (examples are MAAP, PP_UniMI, and MWAA); (2) instruments based on light transmission, that require empirical correction schemes containing assumptions on scattering and loading effects to obtain aerosol absorption coefficient (e.g. [41, 43, 44]).

Pure aerosol particles of different types (Cabot industrial soot; ammonium sulphate; soot produced by a Miniature Inverted Soot Generator - Argonaut Scientific [55, 56] fueled with propane ($CH_3CH_2CH_3$) - hereafter called flaming soot) and mixtures of Cabot soot and ammonium sulphate were produced, mixed in a chamber and sent to a sampling line with several instruments connected and where temperature (T) and pressure (P) were monitored and recorded. Note that for flaming soot two different combustion conditions were tested, the closed tip and the partially open tip flame, reached with higher and lower ratios of air-to-fuel flow rates, respectively [55, 56].

A scheme of the set-up used in the experiment is reported in Figure 2.3; similar set-ups had already been developed at FZJ to perform other inter-comparison, validation, and closure studies [57, 58, 59]. When flaming soot was generated instead of Cabot soot, the Miniature Inverted Soot Generator was connected to the mixing chamber in place of the nebulising system containing the Cabot soot solution (see Figure 2.3).

In our laboratory experiment, instruments measuring on-line aerosol optical properties at different wavelengths were (see Figure 2.3):

- two single-λ CAPS PM_{SSA} (Aerodyne) [30, 58] (wavelengths: 450 nm and 630 nm) both measuring in-situ the aerosol extinction coefficient (σ_{ep}). As explained in the following, the scattering channel of these instruments was not considered but for real-time estimation of aerosol absorption coefficient;

- one three-λ integrating Nephelometer (TSI) measuring in-situ the aerosol scattering coefficient (σ_{sp}) at 450 nm, 550 nm, and 700 nm. Truncation error (see

also sub-section 2.1.1) was corrected following the approach by Massoli et al. [35];

- one MAAP (Thermo) measuring aerosol light absorption coefficient (σ_{ap}) at 632 nm;
- one TAP (Brechtel) to obtain σ_{ap} at 467 nm, 528 nm, and 652 nm. As already mentioned in sub-section 2.1.2, TAP is a filter-based instrument relying on light transmission: multiple scattering and loading effects were corrected according to Virkkula [42].

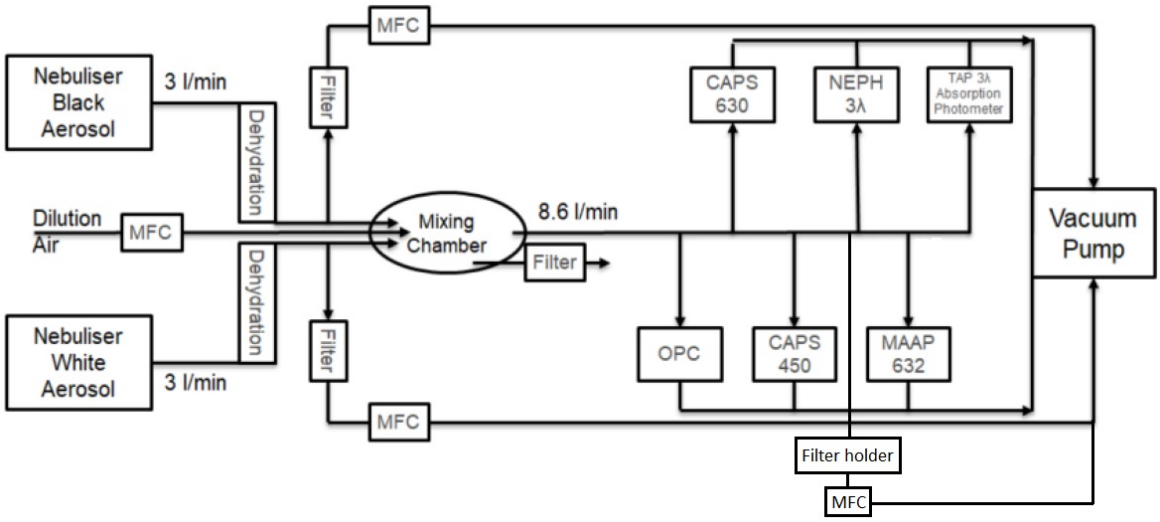

Figure 2.3: Scheme of the set-up used in the inter-comparison exercise at FZJ (adapted from [59]).

47-mm quartz-fibre filters to be analysed off-line by PP_UniMI and MWAA were placed in a filter holder and sampled at a standard (20°C, 1013 hPa) flow rate of 5 l/min controlled by a Mass Flow Controller (MFC) (see Figure 2.3). The sample spot diameter on each filter was reduced to 8 mm to ensure absorbance values higher than LOD also on brief sampling times (shorter than 2 h). In order to explore PP_UniMI response to different ABS values, ABS at 635 nm were targeted to the range 0.1-1.0. Aerosol absorption coefficient σ_{ap} at 630 nm and its stability all the experiment long were estimated on-line by CAPS PM_{SSA} output values; knowing the flow rate and considering a suitable time interval, ABS values were evaluated using Eq. 2.6. In total, 22 samples were produced; the sample with ammonium sulphate only resulted in ABS<LOD at all four wavelengths, thus confirming that absorption coefficients by PP_UniMI are not biased by the effects of scattering particles, i.e. the algorithm used is able to account for such effects.

In this study, the so-called "Ext-Sca", i.e the difference between σ_{ep} by CAPS and

σ_{sp} by Nephelometer (see Eq. 1.25 in sub-section 1.2.2) was considered as the in-situ method for the measurement of σ_{ap}; since low Single Scattering Albedo (Eq. 1.26) values were used to quickly obtain suitable filter loadings (i.e. high ABS), the difference of the two quantities employed was expected to be significantly higher than zero, therefore diminishing the uncertainty of this approach compared to cases (common in ambient conditions) in which extinction and scattering have very similar values (i.e high SSA). Furthermore, in-situ instruments are often considered more representative of real conditions as they directly measure aerosol properties in the air, thus excluding possible modifications induced by particle deposition on the filter matrix and avoiding assumptions about parameters included in correction schemes (see Section 2.1). For these reasons, all values were reported to 450 nm and 630 nm (the wavelengths of the two CAPS) making use of Ångström Exponents calculated with the two nearest original wavelengths for each instrument (see sub-section 1.2.2 and Equation 1.29). Conversely, 4-λ PP_UniMI values of aerosol absorption coefficient were reported to the two reference wavelengths using for each sample an AAE value obtained by a power-law fit over the four σ_{ap} (see sub-section 1.2.2), in order to better exploit the whole spectral range available and the information provided by each wavelength.
For all multi-wavelength methods, the comparison of the absorption wavelength dependence was made considering AAE calculated using (see Eq. 1.30) the 405-635 nm wavelength pair for PP_UniMI and 450-630 nm for "Ext-Sca" and TAP.

Results of the inter-comparison exercise

As for the aerosol absorption coefficient σ_{ap}, we compared PP_UniMi with the "Ext-Sca" method at the two λ 450 nm and 630 nm, first of all taking into account all the available data; data from on-line instruments were averaged over filter sampling intervals for direct comparison. Results showed that the two methods gave wavelength-independent responses, but exhibited significant differences between samples with Cabot soot (and its mixtures with ammonium sulphate) and of flaming soot (independently of the combustion conditions). Figure 2.4 reports the comparisons between $\sigma_{ap}(\lambda)$ by PP_UniMI and by the "Ext-Sca" method.
It can be noted that in general the correlation was good in all cases (correlation coefficient r$<$0.9 only for flaming soot at 450 nm), and that the agreement was excellent (within few percents) when Cabot soot was sampled. Conversely, flaming soot produced a difference of about 50% between the two methods, with a lower response by PP_UniMI compared to the "Ext-Sca" technique.

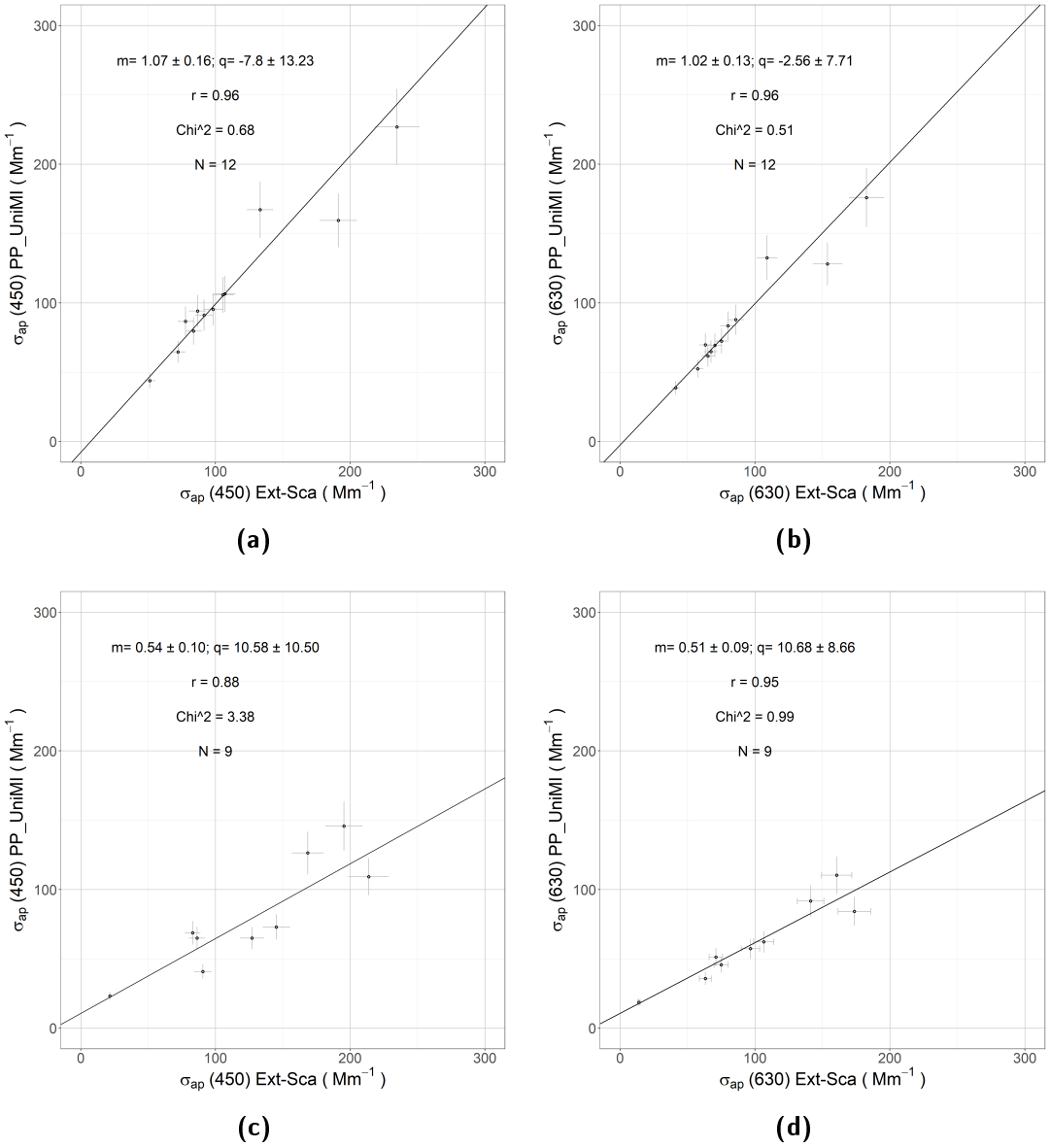

Figure 2.4: Scatter-plots of $\sigma_{ap}(\lambda)$ measured with PP_UniMI versus $\sigma_{ap}(\lambda)$ obtained on-line by the "Ext-Sca" method. (a) and (b): Cabot soot and mixtures; (c) and (d); flaming soot. Statistics of Deming linear regression analyses are reported.

To investigate possible causes of this discrepancy, we examined also results obtained by the other filter-based instruments (MAAP and TAP), considering the wavelength at which all measurements were available (i.e. 632 nm for MAAP and 630 nm for TAP). Linear regression analyses were performed between couples of instruments, using the MAAP as the reference filter-based instrument [29]. This comparison showed that all filter-based instruments gave similar responses, and that they did not exhibit different behaviours when measuring Cabot soot or flaming soot. Statistics of the linear regression analyses performed considering all data are reported in Table 2.1.

Table 2.1: Statistics of the linear regression analyses performed comparing filter-based instruments, considering all data (Cabot soot, flaming soot, and mixtures). Note that both regressions showed an intercept compatible with zero within 3 standard deviations, therefore they were forced to 0.

$\sigma_{ap}(630)$	PP_UniMI vs MAAP	TAP vs MAAP
Slope	0.85±0.03	0.89±0.05
r	0.94	0.90
χ^2	2.56	3.68
N	21	19

Considering only polar photometers (PP_UniMI and MAAP), it can be noted that there is still a non negligible difference in the response of the two instruments: this result was investigated to find possible explanations. In this case, the discrepancy could not be ascribed to sampling artefacts originating by the interaction of volatile organic compounds (typically present in ambient atmosphere) with the filter matrix, that can enhance measured optical properties; indeed, these effects largely depend on the type of filter (membrane or fibrous) used and in this experiment both MAAP and PP_UniMI employed fibre filters (see Vecchi et al. [45] for details about artefacts effects on optical measurements). The reason for the different response was attributed to the specific set-up and data analysis of the two techniques. Even though PP_UniMI and MAAP are based on the same general measuring principle, a relevant difference exists in the way they calculate integrals of light scattered in the forward and in the backward hemispheres, used to infer σ_{ap} via a two-layer radiative transfer model (see sub-section 2.2.1). Indeed, while PP_UniMI is able to measure the angular distribution of light transmitted and scattered by the sample over the whole scattering plane (from 0° to 173°), MAAP performs measurements of the scattered light intensity only at three fixed angles and the whole angular distribution is reconstructed from these data via analytical functions as reported in Petzold and Schönlinner [37]. Figure 2.5 shows angular distributions of light scattered by two filter samples collected in Jülich (one with Cabot soot and one with flaming soot), normalised to the maximum reached in each hemisphere, as directly measured by PP_UniMI at 635 nm and reconstructed with the MAAP approach from PP_UniMI data. It can be noted that the hypotheses used in the MAAP are not fully consistent with the shape of the angular distribution, especially in the forward hemisphere. In addition to assumptions about the angular distribution of scattered light, the integral of the light scattered by the blank filter in the backward hemisphere B_f is assumed to have a fixed value in the MAAP software

[37] while it is directly measured by PP_UniMI (see Appendix A). To evaluate the effects of these assumptions, PP_UniMI data were analysed with the same approach of the MAAP, i.e. considering only the same three angles, reconstructing the angular distribution with the same analytical functions, and using the same value for B_f. Repeating the comparison PP_UniMI vs MAAP with data analysed in the same way, the linear regression analysis obtained had a slope of 0.97±0.03 and an intercept compatible with zero; the correlation coefficient r was 0.95, and $\chi^2 = 1.62$. Therefore, the reason for the observed difference was proved to be the data analysis procedure, thus evidencing a bias in MAAP measurement not previously singled out by literature works.

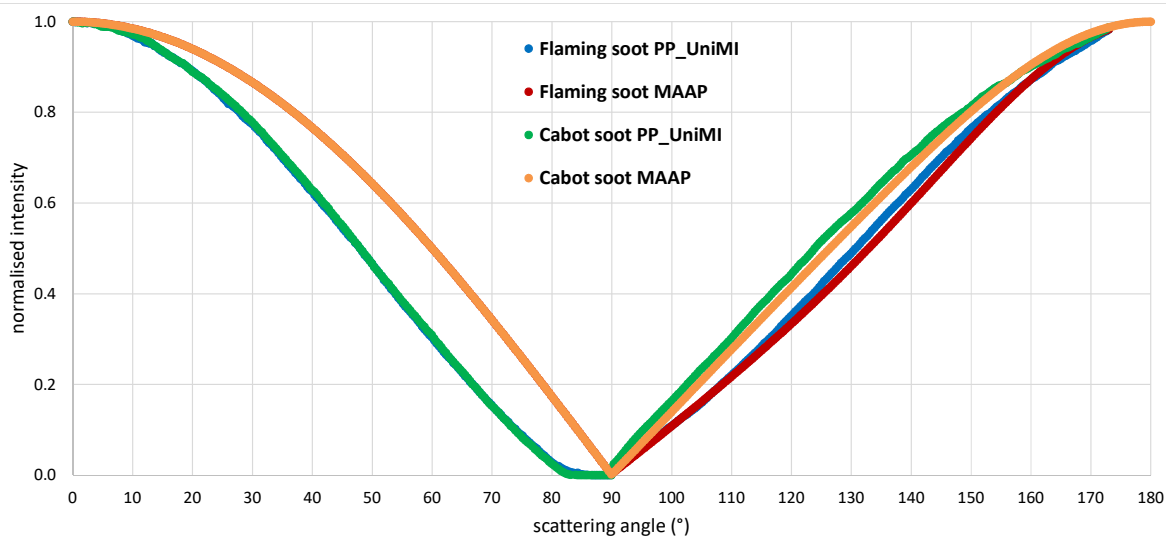

Figure 2.5: Normalised angular distributions of light scattered by Cabot soot and flaming soot collected on filters as measured by PP_UniMI and reconstructed using MAAP approach.

Taking into account considerations made above, a possible reason for the results showed in Figure 2.4 could be the different particle morphology of the two soot types: Cabot soot specifications report that it is made of spheres with nominal diameter of 105 nm (geometric standard deviation 1.55), whereas elecron microscopy analyses of flaming soot performed in recent studies [55, 56] show that the Miniature Inverted Soot Generator generally produces fractal-like aggregates with variable length, reaching 2 μm, depending on the combustion conditions. This difference in aerosol morphology could generate biases arising from particle deposition on the filter matrix, or cause effects in in-situ instruments that are not considered in the standard correction schemes (e.g. the truncation error); this could explain the homogeneous response of filter-based instruments. Further studies are needed to clarify how the morphology impacts on absorption measurements

As far as the wavelength dependence is concerned, it was already noted (Figure 2.4) that a similar response was shown by PP_UniMI at 450 nm and 630 nm compared to the "Ext-Sca" method, provided that the same soot (Cabot or flaming) is considered. To further compare results of all multi-wavelength methods, average AAE values for each aerosol type were calculated (Table 2.2).

Table 2.2: Average (± standard deviation) AAE values calculated for each aerosol type using wavelength pairs (450-630 nm for Ext-Sca and TAP; 405-635 nm for PP_UniMI). "Mixtures" represent mixtures of Cabot soot and ammonium sulphate.

Aerosol type	AAE		
	Ext-Sca	PP_UniMI	TAP
Cabot soot	0.74±0.06	0.74±0.08	1.21±0.02
flaming soot	0.74±0.30	0.70±0.25	0.87±0.21
Mixtures	0.66±0.04	0.62±0.12	1.26±0.03

It can be noted that both "Ext-Sca" and PP_UniMI show AAE values lower than those retrieved from TAP data. According to scattering theory, these lower values would be compatible with particle sizes larger than e.g. Cabot soot nominal diameter (105 nm), whereas AAE given by the TAP is consistent with small black particles with $d_p \approx 100$ nm (see e.g. [60]). Flaming soot produced the highest AAE variability, likely due to the different combustion conditions used. As for mixtures, ammonium sulphate particles were the smallest (nominal geometric diameter 40 nm) and produced a shift towards a weaker absorption wavelength dependence.
Overall, the inter-comparison exercise confirmed that PP_UniMI agrees with the in-situ "Ext-Sca" method at the tested wavelengths as well as with other filter-based methods. In addition, it revealed that when particles with a very complex morphology are sampled, in-situ and filter-based methods can show significantly different responses. These findings require further investigation and comparisons, also with ambient aerosol, for which the effects of particle composition and morphology are expected to be not as strong as for laboratory-generated aerosols.

2.2.3 Set-up for non conventional filters

During this PhD work, several collaborations were carried out to national and international projects to which the Environmental Physics research group took part. In these frameworks, different kinds of samples collected during several campaigns with various goals were analysed as for multi-λ aerosol absorption coefficient with PP_UniMI, and

some of them required an optimsation of the instrument set-up for suitable measurements, as described in the following paragraphs.

Set-up realised for low-cost smart samples analysis

The University La Sapienza (Rome - Italy) and the Institute for Atmospheric Pollution of the National Research Council (IIA-CNR), in collaboration with the Regional Environmental Protection Agency (ARPA) of the Umbria region (central Italy), designed and realised a 1-year sampling campaign aiming at monitoring and evaluating the air quality in Terni (Umbria), a city heavily impacted by different anthropogenic aerosol sources [61].

During this campaign, in order to obtain high-spatially resolved data over the whole city surface, low-cost smart samplers HSRS (High Spatial Resolution Sampler - Fai Intruments) were employed. These instruments provided PM_{10} samples collected of PTFE filters with 37 mm diameter (Pall), that were characterised afterwards with different analyses (see Section 3.2). It has to be noted that, since filters from this campaign did not have the standard 47 mm diameter (for which PP_UniMI has a dedicated set-up) and blank filters were not available before sampling, some devices listed in the following had to be implemented in order to be able to perform reliable optical measurements also in this case.

- Customised adapters were designed and then realised by the Mechanical Workshop of the University of Milan Physics Department to be able to analyse 37 mm filters.

- As no measurement of each blank filter was possible, eight blank filters of the same lot as those sampled during the campaign were used as representatives. The available blanks were measured and the angular distributions of scattered light obtained were averaged (after normalising them to a reference laser intensity for each wavelength) in order to calculate a fictitious "average blank filter" distribution. This angular distribution was then employed in the data analysis of all samples as the one of the blank filter.

- Since membrane filters (like the PTFE used here) are thinner than fibre filters (e.g. quartz or glass), a procedure similar to the one developed by Bernardoni et al. [46] to increase multiple scattering effects and hence the system sensitivity was applied, putting a blank glass-fibre filter below each PTFE filter for optical measurements. Indeed, the algorithm used to retrieve σ_{ap} from PP_UniMI measurements efficiently corrects for these effects. Moreover, the use of additional fibre filters reduces the consequences of filter-to filter variability, which is higher for membrane filters compared to fibre ones.

Results of measurements performed on filters from the Terni campaign are reported in Section 3.2.

Set-up realised for ACTRIS-2 – Mt. Cimone and Po Valley Field Campaign

In July 2017, the international Mt. Cimone and Po Valley Field Campaign was launched in the framework of the European project ACTRIS-2 (Aerosol, Clouds and TRace gases InfraStructure).
During this PhD work, multi-wavelength measurements of aerosol absorption coefficient σ_{ap} were performed with PP_UniMI on 24-h 47 mm quartz-fibre filter samples collected at an urban background site in Bologna and in San Pietro Capofiume, a rural location in the Po Valley; in addition, samples with varying time resolution were collected at the remote site of Mt. Cimone at 2165 m asl on 90 mm diameter quartz-fibre filters. Due to their size, filters from Mt. Cimone were punched to obtain spots with a diameter of 33 mm, that were analysed with PP_UniMI using the custom-made adapters employed for Terni filters. Moreover, also in this case, for samples of each site some blank filters of the same lot were measured and their scattering angular distribution was averaged to obtain a representative blank filter to be used in data analysis.
Results obtained by the analysis of the ACTRIS-2 – Mt. Cimone and Po Valley Field Campaign filters samples with PP_UniMI are reported in Section 3.3.

2.2.4 Investigation of the scattering enhancement factor

In the last years, the Aethalometer has become one of the most common filter-based instruments to assess on-line multi-wavelength aerosol absorption coefficient [62]. Its principle of operation is similar to other instruments such as the PSAP and the TAP (see sub-section 2.2.2). Different models of Aethalometer have been developed in the last decades, the most recent being the AE33 [63], on which this work is focused.

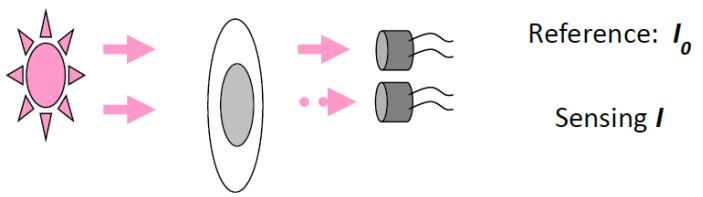

Figure 2.6: Scheme of the Aethalometer operation [64].

As already mentioned, the Aethalometer is based on the measurement of the attenuation of a light source, determined via the ratio of light intensity I transmitted

through the sampled spot to the one (I_0) passing through a non-sampled (reference) filter area (see sub-section 2.1.2 and Figure 2.6):

$$ATN = -100 \cdot \ln(I/I_0) \tag{2.7}$$

Considering the spot area S and the sampled volume $F_{in} \cdot \Delta t$ (where F_{in} is the flow and Δt is the sampling time), the attenuation coefficient (σ_{ATN}) is obtained as the change in light attenuation during the sampling:

$$\sigma_{ATN} = \frac{S \cdot (\Delta ATN/100)}{F_{in} \cdot \Delta t} \tag{2.8}$$

The spot is automatically changed when the attenuation reaches a fixed value. Latest Aethalometer models have been developed as multi-wavelength instruments equipped with LED light sources. The AE33 performs measurements at a 7 λ (370, 470, 520, 590, 660, 880, 950 nm).

In order to obtain the aerosol absorption coefficient ($\sigma_{ap,AE}$) from σ_{ATN}, some corrections have to be applied to take into account scattering and loading effects (see sub-section 2.1.2). The Aethalometer correction scheme [40] can be expressed as

$$\sigma_{ap,AE}(\lambda) = \frac{\sigma_{ATN}(\lambda)}{C \cdot R(\lambda)} \tag{2.9}$$

where C is the so-called scattering enhancement factor (>1) and $R(\lambda)$ is the loading factor (<1). Following Virkkula et al. [65], the loading factor can also be written as $R(\lambda) = 1 - k \cdot ATN(\lambda)$, where k is called loading compensation parameter, which depends on the sampled aerosol only.

In the AE33, the loading compensation has been implemented as a real-time correction by means of the dual-spot system, whose scheme is reported in Figure 2.7.

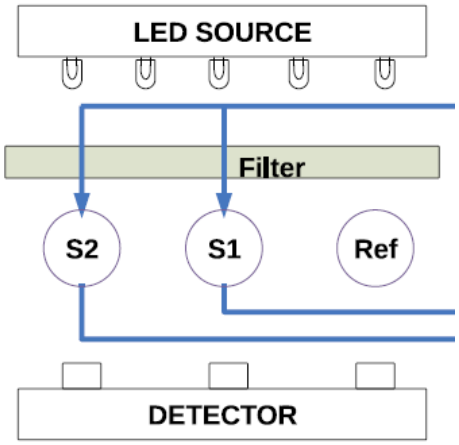

Figure 2.7: Scheme of the AE33 dual-spot system (adapted from [63]).

Aerosol is simultaneously sampled with two different flow rates on two filter spots (S1 and S2), so that two different aerosol loadings but the same value of the loading

compensation parameter k are obtained. Therefore, k is optimised real-time (for details, see Drinovec et al. [63] and references therein) and the AE33 corrective algorithm can be written as [63]:

$$\sigma_{ap,AE}(\lambda) = \frac{S \cdot (\Delta ATN(\lambda)/100)}{F_1(1-\zeta) \cdot C \cdot (1 - k \cdot ATN_1(\lambda)) \cdot \Delta t} \tag{2.10}$$

where subscript "1" indicates the spot sampled with the highest flow rate, and ζ is a leakage factor that accounts for lateral flow in the filter matrix under the optical chamber.

Finally, AE33 gives as output the equivalent Black Carbon (eBC) [66] concentration calculated as:

$$[eBC(\lambda)] = \sigma_{ap,AE}(\lambda)/MAC(\lambda) \tag{2.11}$$

where $MAC(\lambda)$ is the Mass Absorption Cross-Section, relating aerosol absorption to the concentration of the main absorber in particulate form in the atmosphere, i.e Black carbon (BC). In particular, in AE33 the 880 nm channel is the one used to infer eBC concentration, using $MAC(880) = 7.77$ m^2/g.

Based on considerations by Weingartner et al. [40], in the AE33 the scattering enhancement factor C is a wavelength-independent parameter; moreover, it is assumed to have a fixed value of 1.57 for the latest filter tape typology used in this instrument. Nevertheless, some studies (e.g. [67, 53, 68, 69]) have pointed out that this value of C can be underestimated, thus leading to overestimation of the aerosol absorption coefficient, and that it may depend on the wavelength. Moreover, even though Drinovec et al. [63] speculated on the effect of the filter matrix only, an impact of the properties of sampled aerosol is possible, therefore highlighting the need of a deeper investigation of this factor in order to find out tailored values to be used for different sampling sites.

Sometimes, the C factor is determined by the comparison between the Aethalometer and a reference instrument simultaneously measuring aerosol light absorption coefficient, some others applying also *a posteriori* correction algorithms based on data of co-located instruments that measure aerosol scattering (multi-λ) and absorption (usually 1-λ) coefficients (e.g. [67, 70]). In this PhD work, AE33 data were analysed in the frame of the CARE project (see Section 3.1); therefore, different methodologies were explored to find suitable $C(\lambda)$ values to be used to correct AE33 output. The two investigated approaches were:

- measurements of AE33 sample spots with PP_UniMI, to be used as a reference instrument for multi-wavelength aerosol light absorption;
- application of correction algorithms [67, 70] making use of simultaneous measurements performed with a Nephelometer and a MAAP.

These methodologies are described in the following paragraphs.

Measurements of AE33 spots with PP_UniMI

In order to evaluate a suitable, and possibly wavelength-dependent, C for AE33 to be used for data of the CARE experiment (see Section 3.1), some pieces of the AE33 filter tape employed during this campaign were cut and measured off-line with PP_UniMI. On these spots, aerosol with different characteristics was collected at an urban background site in Rome (Italy). To perform the AE33 spot analyses, a dedicated set-up was designed: indeed, as AE33 produces a couple of sample spots with a small relative distance and a tiny space between a couple and the next one, it was not possible to punch the filter tape to have single spots to be measured. Therefore, a customised support was built by UniMI Mechanical Workshop to carry out the optical analysis of two couples of spots at a time. Figure 2.8 shows a picture of the dedicated AE33 set-up assembled in PP_UniMI.

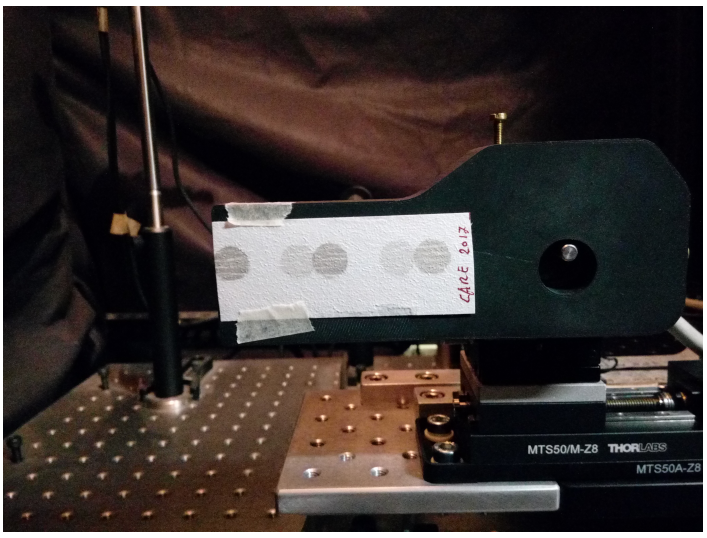

Figure 2.8: Picture of the PP_UniMI set-up dedicated to measurements of AE33 sample spots.

With this approach, $C(\lambda)$ can be determined as:

$$C(\lambda) = \frac{\sigma_{ATN,k}(\lambda)}{\sigma_{ap}(\lambda)} \tag{2.12}$$

where $\sigma_{ap}(\lambda)$ is the aerosol absorption coefficient obtained by PP_UniMI and $\sigma_{ATN,k}(\lambda)$ is the loading-corrected attenuation coefficient by AE33, obtained as:

$$\sigma_{ATN,k}(\lambda) = \sigma_{ap,AE}(\lambda) \cdot C = [eBC(\lambda)] \cdot MAC(\lambda) \cdot C \tag{2.13}$$

as can be derived combining equations 2.9 and 2.11, and using C=1.57 as defined in AE33 software. To obtain $\sigma_{ap}(\lambda)$ from PP_UniMI (see equation 2.6), AE33 spot area was calculated measuring the spot diameter; the sampled volume was taken

from raw AE33 data file. Note that, due to the mismatch between AE33 operating wavelengths and PP_UniMI lasers and in order to avoid data extrapolation beyond PP_UniMI wavelentgh range, in this feasibility study AE33 data were reported to PP_UniMI wavelengths using an Ångström Exponent calculated as a 7-λ power law fit of $\sigma_{ATN,k}(\lambda)$.

It has to be noted that some issues had to be faced during these measurements. Indeed, AE33 sample spots from the CARE campaign had non-homogeneous deposits, characterised by the presence of some white stripes and scratches; in addition, due to a problem in the setting of the distance between spots of two consecutive couples, the S1 spot of a couple overlapped with the S2 spot (see Figures 2.7 and 2.9) of the contiguous couple in almost all cases. Finally, the blank space in between a couple was measured and considered as the blank to be employed in data analysis. A scheme of overlapping spots and of the filter area used for the "blank" measurement is represented in Figure 2.9.

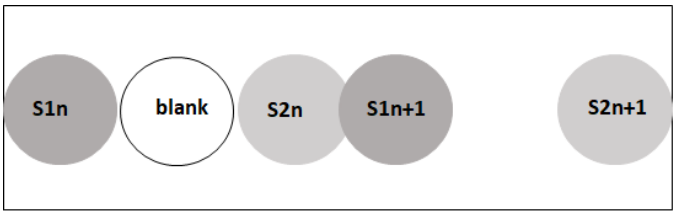

Figure 2.9: Scheme of overlapping AE33 spots with indication of the tape area used for the blank measurement. n and n+1 indicate two consecutive couples.

Due to the issues cited above, only preliminary results are given here; an optimisation of PP_UniMI set-up to measure AE33 spots and a more systematic data analysis comprising also spots from other campaigns is in progress at the UniMI Environmental Physics research group.

Table 2.3: Average ($\pm$ standard deviation) values of $C(\lambda)$ obtained from the analysis of the 11 spots couples taken from the CARE AE33 filter tape and measured with PP_UniMI.

C(405)	**C(532)**	**C(635)**	**C(780)**
4.7±0.6	5.6±1.7	4.9±0.9	4.6±0.8

Table 2.3 reports average ($\pm$ standard deviation) values of $C(\lambda)$ obtained according to Eq. 2.12 from the analysis of 11 spot couples taken from the CARE AE33 filter tape and measured with PP_UniMI. For each couple, the spot sampled with the highest

flow rate was considered as it presented ABS values well above LODs.
It can be noted that all $C(\lambda)$ values are about three times higher than the fixed value used in the AE33 internal software $C = 1.57$, although no systematic wavelength dependence was observed. These values are larger than those reported by some studies (e.g. [67, 53, 68, 69]) dealing with the possible C underestimation. This can be caused by the issues described above, that affected AE33 spot measurements with PP_UniMI. More reliable values could be obtained via an optimisation of PP_UniMI set-up for AE33 spots and the analysis of a large number of spots collected at different sites and in different seasons.

Application of correction algorithms based on simultaneous scattering and absorption measurements

In this PhD work, some algorithms developed in the literature to correct Aethalometer data *a posteriori* were investigated and applied to the CARE dataset (see Section 3.1). These methods are based on aerosol absorption and scattering coefficients (possibly multi-wavelength) simultaneously measured by reference instruments co-located with the Aethalometer. During the CARE campaign, multiple on-line instruments measured aerosol optical properties: a MAAP for $\sigma_{ap}(637)$, a Nephelometer measuring σ_{sp} at 450, 525, and 635 nm, and one AE33, all running with 1-min time resolution.
In particular, correction schemes proposed by Segura et al. [70] and by Collaud Coen et al. [67] were implemented using available data. An important difference between these two algorithms is the assumption about C wavelength dependence: the Segura et al. model (hereafter called "SEG") assumes that the scattering enhancement factor depends on the wavelength, whereas the Collaud Coen et al. scheme ("CC") is based on the hypothesis of a fixed C at all wavelengths.
The SEG algorithm was developed for the AE31, an Aethalometer model that did not include the real-time loading compensation. It relies on the empirical relationship found by Arnott et al. [71]:

$$\sigma_{ATN}(\lambda) = C^*(\lambda) \cdot R(\lambda) \cdot \sigma_{ap}(\lambda) + m_s(\lambda) \cdot \sigma_{sp}(\lambda) \tag{2.14}$$

where $C^*(\lambda)$ is the so-called multiple scattering factor and $m_s(\lambda)$ represents the scattering offset, i.e. the fraction of scattered light erroneously attributed to absorption. In the SEG model, $m_s(\lambda)$ and the wavelength dependence of $C^*(\lambda)$ are assumed to be the same as those found by Arnott et al. [71] for laboratory-generated particles (ammonium sulphate and kerosene soot), even though the latter study explicitly warned not to use values obtained under controlled conditions and on a specific filter type. Combining Equations 2.9 and 2.14 and assuming $R(\lambda) \approx 1$ [72], it follows:

$$C(\lambda) = C^*(\lambda) + m_s(\lambda) \cdot \frac{\omega(\lambda)}{1 - \omega(\lambda)} \tag{2.15}$$

$\omega(\lambda)$ can be obtained by MAAP and Nephelometer data (see Segura et al. [70] for details). An iterative procedure allows to retrieve $C(\lambda)$ at all Aethalometer wavelengths starting from $C(637) = \frac{\sigma_{ATN}(637)(ATN<10)}{\sigma_{ap,MAAP}(637)}$, being $\sigma_{ATN}(637)$ calculated from Aethalometer data using an Ångström Exponent obtained as a 7-λ power law fit of $\sigma_{ATN}(\lambda)$. Only data with $ATN < 10$ are considered because in this range the effect of the loading is negligible and does not bias the result of the calculation.
The SEG algorithm was applied to the CARE data only at those wavelengths that were more similar to those of the Nephelometer, in order to reduce biases arising from extrapolations; in addition, λ=880 nm was considered, since it is the reference Aethalometer wavelength used to obtain eBC concentration. Results are shown in Table 2.4. The sensitivity of the model to assumed input parameters was tested by varying the $m_s(\lambda)$ values suggested by Arnott et al. [71] of 10%. Variations of 1% at 470, 520, and 660 nm and of 3% at 880 nm were obtained; the higher value at 880 nm is likely due to the extrapolation.

Table 2.4: Average ± standard deviation $C(\lambda)$ values for the CARE campaign, obtained by the application of the Segura et al. [70] correction algorithm.

C(470)	**C(520)**	**C(660)**	**C(880)**
2.77±0.08	2.87±0.11	3.11±0.25	3.48±0.79

The $C(\lambda)$ values obtained with the SEG algorithm were all compatible with each other, and all values obtained were significantly higher than 1.57. This algorithm was not considered in this PhD work but for a test, due to the numerous assumptions and the use of fixed parameters obtained for a filter type different from the one of AE33.
In contrast to the SEG correction scheme, the CC algorithm, developed for AE31 as well, is based on optimised $C^*(\lambda)$ and $m_s(\lambda)$ values obtained using real-time data acquired in parallel to AE33. In this model, the scattering enhancement factor C is calculated from MAAP data and loading-corrected Aethalometer attenuation at 660 nm, and it is assumed to have the same value at all wavelengths.
Since both preliminary measurements performed on AE33 spots with PP_UniMI and results of the SEG correction did not give a clear indication of C wavelength dependence, and in order to avoid possible biases caused by assumptions on input parameters, the CC algorithm was chosen for the analysis of the CARE dataset, as explained is sub-section 3.1.2, giving $C = 2.66 \pm 0.02$.

2.2.5 Investigating Nephelometer truncation correction

During my 6-months Erasmus+ Traineeship carried out at the Department of Physics of the University of Vienna (Austria), I gained knowledge on on-line instrumentation measuring aerosol scattering coefficient (i.e. Nephelometers - see sub-section 2.1.1), focusing on the investigation of the truncation issue by means of a laboratory experiment and optical simulations, thus coupling experimental and modelling activities. The experiment design and realisation and data analyses were performed in collaboration with members of the University of Vienna Aerosol Physics and Environmental Physics research group.

The truncation issue in polar Nephelometers

Polar Nephelometers are designed to retrieve aerosol scattering coefficient σ_{sp} from light scattered by particles measured in an enclosed air volume at more than one scattering angle. In this work, the commercial Aurora 4000 polar Nephelometer (Ecotech) and the home-made polar Nephelometer developed by Univ.-Prof. i.R. Dr. Helmuth Horvath at the University of Vienna were employed and compared to investigate the truncation correction.

Aurora 4000 polar Nephelometer

The Aurora 4000 polar Nephelometer (Ecotech) is a commercial instrument operating at high time resolution (up to 1 s) measuring aerosol scattering coefficient at three wavelengths (450, 525, 635 nm) thanks to three LED sources. A scheme of the instrument internal structure is shown in Figure 2.10. It is defined as polar since it

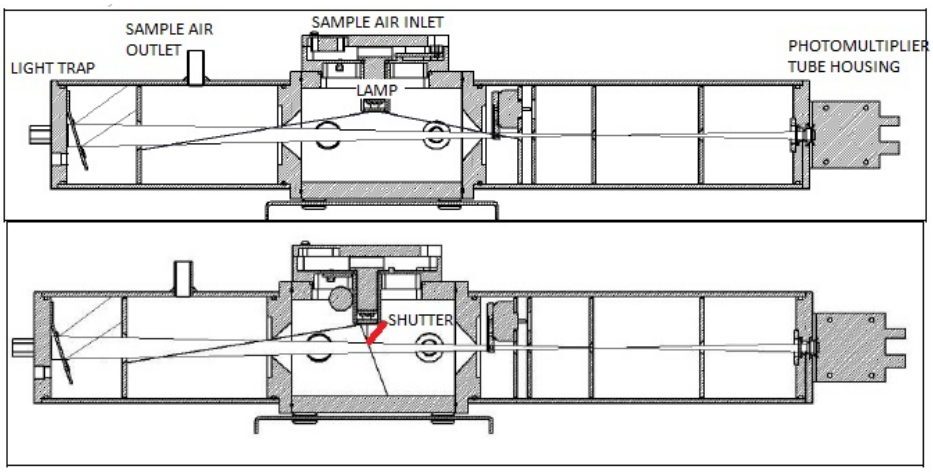

Figure 2.10: Scheme of the Aurora 4000 polar Nephelometer (adapted from [73]).

is equipped with a shutter that can be positioned at several angles to measure the integral of light scattered from different (up to 17) scattering angles in the forward

hemisphere (between 10° and 90°) up to 170°, thus allowing to estimate the angular distribution of the light scattered in the forward hemisphere. Opposite, integrating Nephelometers have the possibility to switch the shutter between two positions only, to obtain the total scattering coefficient σ_{sp} and the back-scattering coefficient σ_{bsp}.
In the Aurora 4000, a truncation correction is needed due to the following limitations:

- the instrument geometry prevents the detection of light scattered at scattering angles $<10°$ and $>170°$;
- the angular intensity distribution of the light source is not perfectly Lambertian;
- the shutter blockage is not perfectly sharp.

The last two points can be easily observed in Figure 2.11, showing the angular intensity function of the light source without the shutter and with the shutter in different positions.

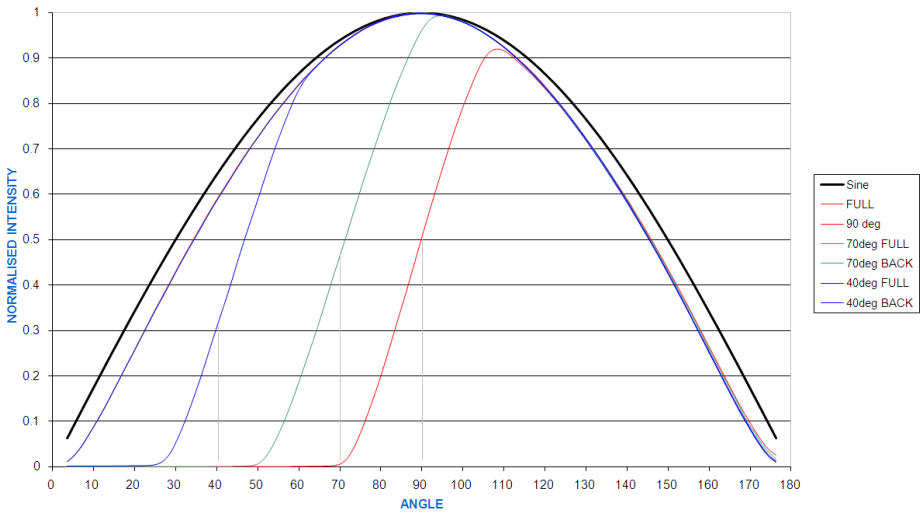

Figure 2.11: Angular intensity function of the Aurora 4000 polar Nephelometer light source without and with the shutter in different positions [73].

These limitations require a correction to obtain the true scattering coefficient σ_{sp} from the instrument output.
Scattered light directly measured by the Nephelometer is a geometrical integration of the volume scattering function $\gamma(\theta)$ (see sub-section 1.2.2); note that in this case, since the instrument sensing volume contains both particles and the carrier gas (usually air), $\gamma(\theta)$ takes into account the two contributions: $\gamma(\theta) = \gamma_p(\theta) + \gamma_{air}(\theta)$, where subscript "p" stands for particles. $\gamma_p(\theta)$ can be calculated from light scattering theory using codes based e.g. on exact Mie theory (see Section 1.2) or on the discrete-dipole approximation [74]; if the instrument is properly calibrated so that air contribution is

known, the scattering and back-scattering coefficients measured by a Nephelometer at the wavelength λ are:

$$\sigma_{sp}^{Neph}(\lambda) = 2\pi \int_0^{\pi} \gamma_p(\theta, \lambda) Z_{ts}(\theta)\, d\theta \tag{2.16}$$

$$\sigma_{bsp}^{Neph}(\lambda) = 2\pi \int_0^{\pi} \gamma_p(\theta, \lambda) Z_{bs}(\theta)\, d\theta \tag{2.17}$$

where Z_{ts} and Z_{bs} are the Nephelometer *angular sensitivity functions* for total and back-scattering, respectively. For an ideal Nephelometer, the angular sensitivity functions would be:

$$Z_{ts}(\theta) = \sin\theta \tag{2.18}$$

$$Z_{bs}(\theta) = \begin{cases} \sin\theta & \text{for } 90^\circ{<}\theta{<}180^\circ \\ 0 & \text{otherwise} \end{cases} \tag{2.19}$$

and the so-called "Nephelometer scattering and back-scattering coefficients" would equal the true ones: $\sigma_{sp}^{Neph}(\lambda) = \sigma_{sp}(\lambda)$ and $\sigma_{bsp}^{Neph}(\lambda) = \sigma_{bsp}(\lambda)$.
Müller et al. [36] studied the design and performance of the Aurora 3000 Nephelometer (Ecotech), that is basically identical to Aurora 4000 but being not polar. For Aurora 3000, Müller et al. developed a parametrisation of the angular sensitivity functions Z_{ts} and Z_{bs} that takes into account non-idealities:

$$Z_{ts}(\theta) = \begin{cases} 0 & \text{for } 0^\circ{\leq}\, \theta \leq \alpha_1 \\ \beta_1 \cdot (\sin\theta)^{\beta_2} & \text{for } \alpha_1 < \theta < \alpha_2 \\ 0 & \text{for } \alpha_2 \leq \theta \,{\leq}180^\circ \end{cases} \tag{2.20}$$

$$Z_{bs}(\theta) = \begin{cases} 0 & \text{for } 0^\circ{\leq}\, \theta \leq \alpha_1 \\ \max\left(0, \beta_1 \cdot (\sin\theta)^{\beta_2} \cdot \min\left(1, \frac{\theta-\gamma_1}{\gamma_2}\right)\right) & \text{for } \alpha_1 < \theta < \alpha_2 \\ 0 & \text{for } \alpha_2 \leq \theta \,{\leq}180^\circ \end{cases} \tag{2.21}$$

where:

- α_1 and α_2 represent the upper and lower truncation angles, respectively (α_1=10° and α_2=170° for Aurora 3000 and 4000);
- β_1 is a normalisation factor and β_2 accounts for the decrease in relative illumination at small and large angles (i.e. near 0° and 180° - see Figure 2.11);
- γ_1 and γ_2 account for the shadowing of the shutter (see red line in Figure 2.11).

Correction factors to be applied to obtain the true scattering and back-scattering coefficients from Nephelometer measurements are [36]:

$$C_{ts}(\lambda) = \frac{\sigma_{sp}(\lambda)}{\sigma_{sp}^{Neph}(\lambda)} \cdot \frac{\sigma_{sg,R}^{Neph}(\lambda)}{\sigma_{sg,R}(\lambda)} \tag{2.22}$$

$$C_{bs}(\lambda) = \frac{\sigma_{bsp}(\lambda)}{\sigma_{bsp}^{Neph}(\lambda)} \cdot \frac{\sigma_{bsg,R}^{Neph}(\lambda)}{\sigma_{bsg,R}(\lambda)} \tag{2.23}$$

where the second ratios compensate for the non-ideal illumination when calibrating the Nephelometer with known Rayleigh (subscript "R") scattering gases (clean air and CO_2). Correction factors $C_{ts}(\lambda)$ and $C_{bs}(\lambda)$ depend on aerosol size and composition and can be simulated for particles of known diameter and complex refractive index. Anderson and Ogren [33] found a relationship between the Scattering Ångström Exponent SAE^* (superscript * indicates that it is calculated from raw $\sigma_{sp}^{Neph}(\lambda)$) and the correction factor for total scattering C_{ts}:

$$C_{ts} = a + b \cdot SAE^* \tag{2.24}$$

Conversely, no correlation was found between C_{bs} and SAE^*. The parameters a and b were obtained from true and Nephelometer scattering coefficients computed via Mie theory for several ranges of particle sizes and refractive indices. Anderson and Ogren performed the calculations for the Integrating Nephelometer TSI 3563; the same approach was adopted by Müller et al. to re-calculate a and b for the Aurora 3000, and the same parameters are commonly used to correct also the output of Aurora 4000. Owing to the fact that the Nephelometer operates at three wavelengths, $SAE^*(450, 525)$, $SAE^*(450, 635)$, and $SAE^*(525, 635)$ are used for truncation corrections at 450, 525, and 635 nm, respectively. Moreover, different a and b values were computed for aerosol sampled without any size cut and with a size cut of 1 μm; indeed, different relationships were found in the two cases [33, 36]. The uncertainty introduced by the truncation correction is reported to be smaller than 3% when the single scattering albedo ω is higher than 0.8, whereas for $\omega < 0.8$ it can increase a lot [34, 35, 36].

Home-made polar Nephelometer

The polar Nephelometer developed at the University of Vienna is a home made instrument measuring aerosol scattering coefficient at one wavelength (532 nm) with a maximum time resolution of 35 minutes. It is calibrated daily with CO_2 and particle-free air. A scheme of the instrument principle is shown in Figure 2.12. The detector is placed on a rotating arm and measures the volume scattering function $\gamma(\theta)$ in the range of scattering angles 5-175° with an angular resolution of 5°, increased to 1° towards the extreme forward and backward regions (5-10° and 170-175°). For this instrument,

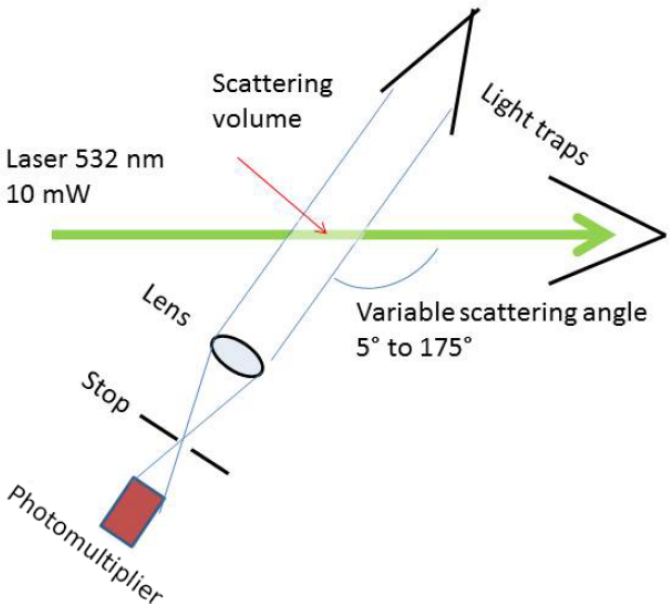

Figure 2.12: Scheme of the principle of the home-made polar Nephelometer developed at the University of Vienna [75].

the truncation is corrected for via an extrapolation of $\gamma(\theta)$ to 0° and 180°; this is accomplished by a stepwise procedure based on the slope of the measured signal at small and large scattering angles, exploiting the higher angular resolution in these regions [76]. The reconstructed volume scattering function is then integrated over the whole solid angle to obtain the scattering coefficient according to Equation 1.23. Moreover, with the home-made polar Nephelometer it is possible to calculate the asymmetry parameter g and the backscatter fraction b (see Section 1.2). The uncertainty introduced by this correction on σ_{sp}, g, and b is reported to be smaller than 1% [76].

Design and realisation of a laboratory experiment to evaluate truncation correction schemes

During the traineeship, a laboratory experiment was realised to investigate multi-wavelength aerosol scattering coefficient measured with polar Nephelometers, with a focus on the truncation corrections. The experiment was carried out in collaboration with MSc. Marilena Teri for the design, the laboratory activity, and data analysis; with Univ.-Prof. Dr. Bernadett Weinzierl for the planning, with Univ.-Prof. i.R. Dr. Helmuth Horvath for measurements with the home-made Nephelometer; and with Dr. Josef Gasteiger for the modelling part.
Several instruments were deployed for this purpose:

- an atomizer and a Vienna-type Differential Mobility Analyser (DMA) [77] for aerosol generation and size selection;

- a mixing chamber;
- the two polar Nephelometers previously described, one Ultra-High Sensitivity Aerosol Spectrometer (UHSAS - Droplet Measurement Technology), and a Condensation Particle Counter (CPC - TSI) to measure aerosol properties.

Due to the different time resolution of the instruments, all data were averaged over the same time intervals to be directly compared. A scheme of the set-up realised is reported in Figure 2.13.

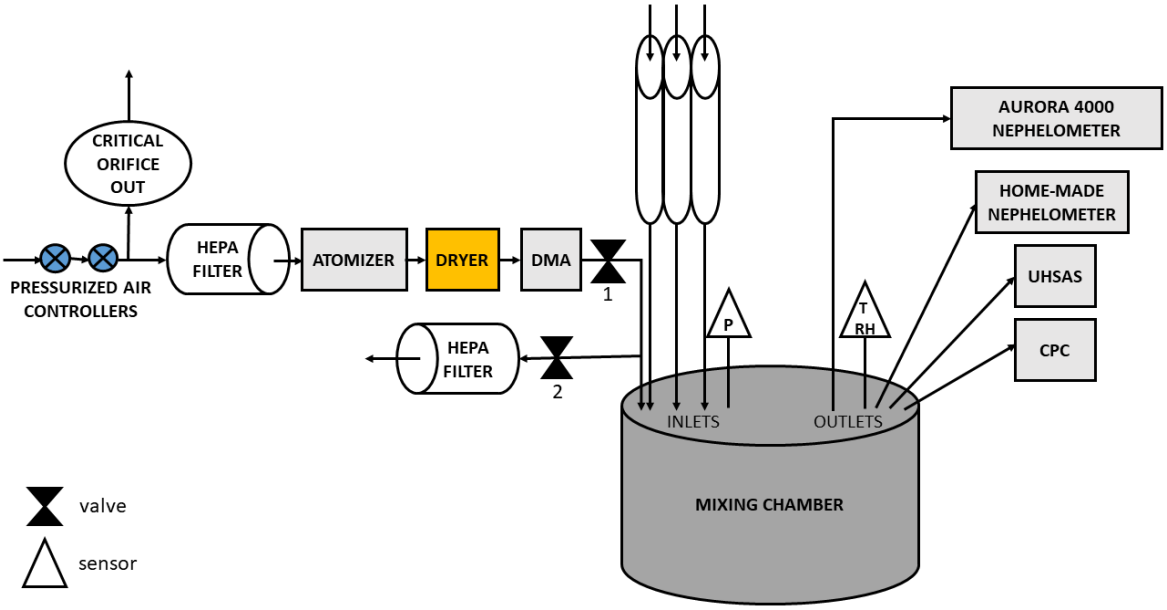

Figure 2.13: Scheme of the set-up of the experiment performed at the University of Vienna.

Particles of ammonium sulphate (AMSUL) and Polystyrene Latex (PSL) spheres were used: they were dissolved in water and atomised; afterwards, a dryer was employed upstream the DMA, whose voltage was varied to select different quasi-monodisperse aerosol sizes in the range 150-500 nm for AMSUL and 200-800 nm for PSLs. Particles exiting the DMA were sent to the mixing chamber to dilute them and to ensure that the same aerosol was sampled by all instruments downstream. Different instruments were connected via stainless steel tubing to the chamber; note that, in order to reduce biases when comparing all instruments, particle losses in the tubes were calculated with the Particle Loss Calculator (PLC) software [78] and taken into account. Nephelometer scattering coefficient $\sigma_{sp}^{Neph}(\lambda)$ at 450, 525, and 635 nm was measured by Aurora 4000, and the truncated volume scattering function $\gamma(\theta)$ at 532 nm was retrieved by the home-made polar Nephelometer; note that in this case Aurora 4000 was set to measure at all possible angles. Moreover, the CPC measured the total particle number concentration in the size range 7 nm-10 μm and the aerosol number size distribution in

99 size bins in the range 60 nm-1 μm was obtained from UHSAS; from UHSAS data, the number of particles N, the geometric mean diameter $\overline{d_g}$ and the geometric standard deviation σ_g of each log-normal size distribution (see Section 1.1) were calculated [10]. Indeed, also particles with the same electrical mobility of the desired aerosol but with double and triple charge were selected by the DMA, and produced additional modes at larger sizes. Parameters of the size distributions and aerosol refractive indices given by AMSUL and PSLs manufacturers were used as input of the MOPSMAP tool (Modelled Optical Properties of enSeMbles of Aerosol Particles - `https://mopsmap.net/` [79]), that combines several approaches for the analytical calculation of aerosol optical properties, assuming spherical particles. MOPSMAP outputs were the scattering coefficient $\sigma_{sp}(\lambda)$ and the scattering phase function $P(\theta, \lambda)$ (see Section 1.2); the latter, for an ensemble of particles, is related to the aerosol volume scattering function $\gamma_p(\theta, \lambda)$ through $P(\theta, \lambda) = 4\pi\gamma_p(\theta, \lambda)/\sigma_{sp}(\lambda)$. Modelled $\sigma_{sp}(\lambda)$ was compared to the same quantity measured by the two polar Nephelometers corrected for truncation as explained in the following. Moreover, $P(\theta, \lambda)$ from MOPSMAP was used to calculate $\gamma_p(\theta, \lambda)$ that was integrated with Aurora angular sensitivity functions to get $\sigma_{sp}^{Neph}(\lambda)$ according to Equation 2.16. In addition, σ_{sp} by MOPSMAP and the one computed from the home-made polar Nephelometer measurements were compared.
Analysis of all data collected in the experiment is still in progress. In particular, my focus was on an *a posteriori* correction of UHSAS data according to a modification of the instrument calibration curve for ammonium sulphate to have a better agreement with DMA nominal sizes; indeed, a calibration check demonstrated that there had been deviations of the measured size distributions from selected particle sizes, especially for d_p>600 nm, that did not occur for PSLs. Moreover, I contributed to data analysis running the MOPSMAP tool for all measured particle types and sizes and evaluating the uncertainties in the model outputs starting from the calculation of uncertainties on input parameters and exploring MOPSMAP sensitivity to changes of inputs in their variability ranges. The assessment of Aurora 4000 uncertainties, its correction for calibration drift and truncation, in addition to corrections for particle losses were performed by MSc. Marilena Teri. Data analysis of the home-made polar Nephelometer were carried out by Univ.-Prof. i.R. Dr. Helmuth Horvath.

Results of the laboratory experiment

Figure 2.14 reports comparisons between multi-wavelength aerosol scattering coefficient measured by Aurora 4000 and modelled with the MOPSMAP tool. Different points represent different particle sizes selected with the DMA. The left panel shows the comparison between the raw (not corrected for truncation) $\sigma_{sp}^{Neph}(\lambda)$ measured by Aurora 4000 and $\gamma_p(\theta, \lambda)$ by MOPSMAP integrated with the Aurora 4000 angular sensitivity function Z_{ts} to obtain a theoretical $\sigma_{sp}^{Neph}(\lambda)$. The right panel, instead, shows

Aurora 4000 scattering coefficient corrected for truncation with $C_{ts}(SAE^*)$ (Equation 2.24) compared to $\sigma_{sp}(\lambda)$ obtained by MOPSMAP.

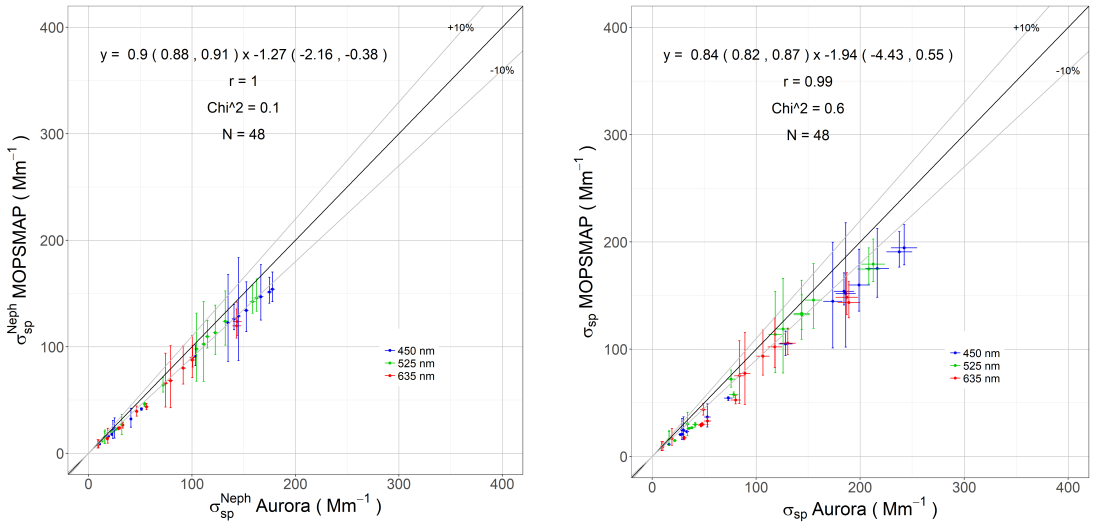

Figure 2.14: Comparison of of $\sigma_{sp}^{Neph}(\lambda)$ (raw data, left) and of $\sigma_{sp}(\lambda)$ (corrected data, right) measured with Aurora 4000 and modelled with the MOPSMAP tool. The parameters of the Deming regressions are shown with their 95% confidence intervals in brackets.

It can be noted that in both cases the modelled values are lower than measured ones, and that the truncation correction produces a larger difference; uncertainties on the modelled scattering coefficients are quite large, but likely a better estimate of them could be achieved with a Montecarlo method. However, the observed discrepancies could be due to both uncertainties in the model inputs obtained by UHSAS data and in the parametrisation of Z_{ts} and C_{ts}. Moreover, some differences can be observed among data at the three wavelengths, probably due to the unique Z_{ts} parametrisation at all λs and to the assumptions on the particles refractive index. Indeed, for ammonium sulphate, the nominal value was retained at 525 nm, whereas it was slightly changed at 450 nm and 635 nm; PSLs, instead, were assumed to have a constant refractive index over the visible spectrum. Deming regression parameters for the separate comparisons at the wavelengths 450, 525, and 635 nm are reported in Table 2.5.

Table 2.5: Deming regression parameters (with 95% confidence intervals in brackets) for the comparison of $\sigma_{sp}^{Neph}(\lambda)$ and $\sigma_{sp}(\lambda)$ modelled by MOPSMAP and measured by Aurora 4000 at the three Nepehelometer operating wavelengths 450, 525, and 635 nm.

Quantity	Parameter	Wavelength (nm)		
		450	525	635
$\sigma_{sp}^{Neph}(\lambda)$	slope	0.89 (0.87-0.90)	0.92 (0.90-0.95)	0.87 (0.84-0.90)
	intercept	-1.16 (-2.60-0.27)	-0.86 (-2.27-0.55)	-1.21 (-2.79-0.37)
$\sigma_{sp}(\lambda)$	slope	0.82 (0.81-0.84)	0.90 (0.82-0.97)	0.82 (0.75-0.88)
	intercept	-2.39 (-4.62-0.16)	-1.80 (-7.22-3.61)	-2.17 (-7.82-3.48)

Figure 2.15 reports comparisons between aerosol scattering coefficient measured by Aurora 4000 at 525 nm and the one retrieved at 532 nm from data of the home-made polar Nephelometer developed by Univ.-Prof. i.R. Dr. Helmuth Horvath. Different points represent different particle sizes selected with the DMA.

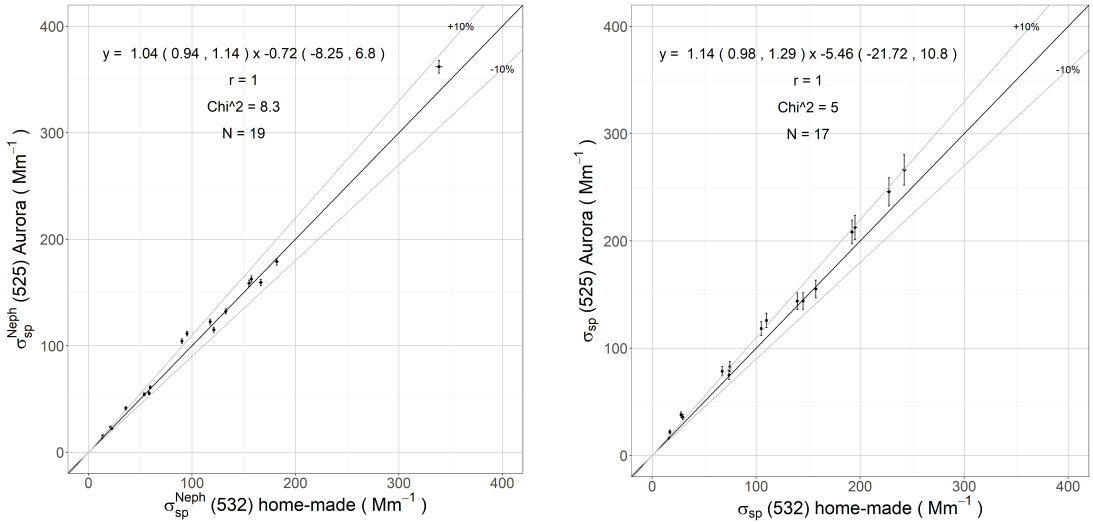

Figure 2.15: Comparison of of $\sigma_{sp}^{Neph}(\lambda)$ (raw data, left) and of $\sigma_{sp}(\lambda)$ (corrected data, right) measured with the home-made polar Nephelometer and with Aurora 4000. The parameters of the Deming regressions are shown with their 95% confidence intervals in brackets.

The left panel shows the comparison between the raw (not corrected for truncation) $\sigma_{sp}^{Neph}(525)$ measured by Aurora 4000 and $\gamma_p(\theta, 532)$ measured by the home-made Nephelometer integrated with the Aurora 4000 angular sensitivity function Z_{ts}. The right panel, instead, shows Aurora 4000 scattering coefficient at 525 nm corrected for

truncation with $C_{ts}(SAE^*)$ (Equation 2.24) compared to $\sigma_{sp}(532)$ obtained by the home-made polar Nephelometer. No corrections for wavelength differences between the two instruments were applied. Aurora 4000 measures a scattering coefficient that is slightly higher than the one by the home-made polar Nephelometer. Similarly to what observed about the comparison between Aurora 4000 data and MOPSMAP outputs, the truncation correction appears to increase the discrepancy between the two instruments results.
The comparison between aerosol scattering coefficient measured by the home-made polar Nephelometer and the one modelled by MOPSMAP from size distribution parameters is shown in Figure 2.16.

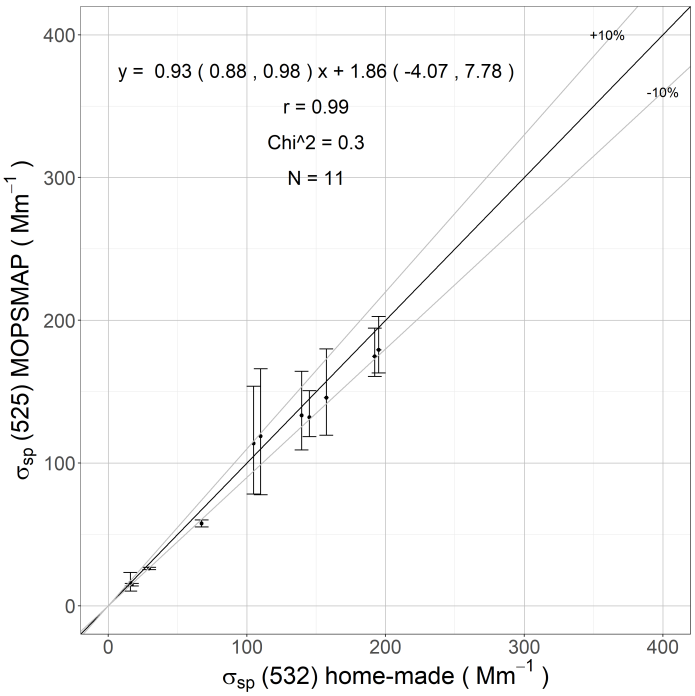

Figure 2.16: Comparison of of $\sigma_{sp}(\lambda)$ measured with the home-made polar Nephelometer and modelled with the MOPSMAP tool. The parameters of the Deming regression are shown with their 95% confidence intervals in brackets.

It can be observed that the modelled σ_{sp} is lower than the corresponding one measured by the home-made Nephelometer. This can be due to input parameters used in MOPSMAP, to Z_{ts} parametrisation, and to the extrapolation procedure employed to correct data of the home-made Nephelometer for truncation.
Similar results are obtained when considering other scattering angles ranges (20-170° or 50-170° have been considered so far), whereas back-scattering shows larger discrepancies among different methods/instruments, and is affected by bigger uncertainties. As already mentioned, analysis of data collected in the described laboratory experiment is still in progress, in particular to refine the retrieval of size distribution parameters

to be used as input in MOPSMAP, and to achieve a better estimation of uncertainties of modelled scattering coefficient. Moreover, data at other angles, that may be useful to understand the truncation issue, still have to be analysed in detail.
It has to be noted that truncation correction for Aurora 4000 is affected by aerosol refractive index [36, 80], thus the particles employed may have affected the results. Investigation of Nephelometer truncation using other aerosol types, also absorbing (e.g. BC or desert dust) could help data interpretation. To meet this point, an additional experiment was carried out at the University of Vienna also in collaboration with Dr. Thomas Müller (Leibniz Institute for Tropospheric Research - TROPOS), sampling resuspended mineral and desert dust; collected data are currently being analysed. Conversely, when only scattering particles are used like in the experiment performed in this work, the use of an extinction monitor such as the CAPS (see sub-section 2.2.2) could give a more complete set of information to analyse the issue. Finally, employing other instruments measuring aerosol size distribution, also in a wider size range, may allow to investigate the problem also in the super-micron fraction, for which the relationship between C_{ts} and SAE^* is less clear and the truncation correction introduces larger uncertainties [33, 36].

2.3 Tailoring the IMPROVE algorithm to retrieve atmospheric light extinction

For the first time, visibility was declared an air quality related value [26] in the U.S. Clean Air Act (1977), also because it heavily influences people perception of air pollution. Therefore, a simple algorithm [26, 81] was developed by the U.S. Interagency Monitoring of Protected Visual Environments (IMPROVE) network [82] to estimate atmospheric light extinction coefficient (σ_{ext}) from concentrations of major PM components, NO_2, and clear-air Rayleigh scattering (i.e. scattering from gaseous species - see Section 1.2), with the final aim of estimating visibility (see sub-section 1.3.2) and analysing possible sources of its impairment at remote and rural sites. The so-called IMPROVE method was originally designed to evaluate visibility trends in U.S. natural parks, and it has been recently updated with a revised form taking into account possible biases occurring at extremely low and high σ_{ext} values. Indeed, both the original and revised IMPROVE methods have been commonly used in the last years to assess light extinction at heavily polluted urban sites such as densely populated Chinese cities (e.g. [83, 84, 85, 86, 87, 88, 89]), even though the algorithm was developed making use of aerosol properties typical of remote areas. It is noteworthy that efficiencies used as fixed coefficients in the IMPROVE algorithm actually vary depending on the location, season, and method used for their retrieval [90].

In this work, in order to robustly apply the IMPROVE algorithm reducing its possible biases when applied at polluted urban sites, an equation with tailored (i.e. site-specific) coefficients was implemented. Major differences of the algorithm developed in this work compared to the IMPROVE one are listed in the following and reported in Valentini et al. [91]:

- dry mass extinction efficiencies were calculated using a discrete dipole approximation code using as input data aerosol size distributions measured in Milan (Italy);
- site-specific water growth functions were computed separately for ammonium sulphate (AMSUL), ammonium nitrate (AMNIT), and organic matter (OM);
- fine soil concentration was evaluated with an equation previously adopted in Milan;
- aerosol absorption contribution was assessed directly through filter-based measurements of aerosol absorption coefficient (σ_{ap}).

The coefficients of the algorithm to reconstruct light extinction were tailored for a suitable application in Milan, a well-known European pollution hot spot [92]. Indeed, the various emission sources impacting on this area and its peculiar meteorological conditions (favouring atmospheric stability especially in wintertime) make atmospheric aerosol very complex in terms of optical and physical-chemical properties. Therefore, since aerosol characteristics in Milan are likely very different from those at the remote and rural IMPROVE sites, the impact of such peculiar PM properties on the application of the algorithm was investigated.
In the following sub-sections, details about the calculations performed are reported.

2.3.1 The IMPROVE algorithm: general approach

As described in Section 1.2, atmospheric light extinction is caused by the interaction of light with both particles and gases. Following the IMPROVE algorithm, extinction by gases can be accurately inferred from their concentration in the atmosphere and from meteorological data. In particular, the method takes into account NO_2 concentration (this gas is considered as the main absorber of visible light in the planetary boundary layer), atmospheric temperature (T) and pressure (P). Both T and P are necessary to calculate the clear-air scattering coefficient (Rayleigh scattering RS=σ_{sp}). It is more difficult to evaluate extinction by aerosol particles, due to their intrinsic complexity.
Reconstructed light extinction coefficient is also used for the estimate of visibility indicators such as the visual range (VR), i.e. the maximum distance at which a black

object can be distinguished against the horizon by an observer [27] (see sub-section 1.3.2).

2.3.2 The tailored approach vs. the IMPROVE revised algorithm

Light extinction coefficient (σ_{ext}) can be expressed as the sum of scattering and absorption coefficients of particles and gases in the atmosphere (see sub-section 1.2.2):

$$\sigma_{ext} = (\sigma_{sp} + \sigma_{sg}) + (\sigma_{ap} + \sigma_{ag}) = \sigma_{sca} + \sigma_{abs} \tag{2.25}$$

where subscripts "s" and "a" indicate scattering and absorption, respectively, while "p" and "g" denote particles and gases; σ_{sca} and σ_{abs} represent total atmospheric scattering and absorption coefficients, respectively.
The IMPROVE revised equation [81] is:

$$\begin{aligned}\sigma_{ext}(RH) = {} & 2.2 \cdot f_S(RH) \cdot [small\ AMSUL] + 4.8 \cdot f_L(RH) \cdot [large\ AMSUL] \\ & + 2.4 \cdot f_S(RH) \cdot [small\ AMNIT] + 5.1 \cdot f_L(RH) \cdot [large\ AMNIT] \\ & + 2.8 \cdot [small\ OM] + 6.1 \cdot [large\ OM] + 10 \cdot [EC] + [FS] \\ & + 1.7 \cdot f_{SS} \cdot [SS] + 0.6 \cdot [CM] + RS(site - specific) \\ & + 0.33 \cdot [NO_2(ppb)]\end{aligned} \tag{2.26}$$

Following the U.S. IMPROVE network prescriptions about aerosol monitoring, the algorithm was devepoled considering major $PM_{2.5}$ chemical components (concentration in $\mu g/m^3$ in square brackets): ammonium sulphate (AMSUL), ammonium nitrate (AMNIT), organic matter (OM), elemental carbon (EC), fine soil (FS), sea salt (SS), with the addition of a term for coarse mass (CM, i.e. $PM_{2.5-10}$).
The IMPROVE revised equation aims at reconstructing the ambient light extinction coefficient (in Mm^{-1}) at the wavelength λ=550 nm under some assumptions: 1) σ_{ext} can be estimated as the sum of six aerosol chemical components plus coarse mass, the Rayleigh scattering term for clear-air, and NO_2 absorption; 2) contributors to reconstructed light extinction are considered as separate terms and particles are assumed to be externally mixed (although it is known that they could be internally mixed - see sub-section 1.2.2); 3) for sulphate, nitrate, and organic matter, dry mass extinction efficiencies (i.e. multiplicative numerical factors in Equation 2.26) are calculated separately for small and large modes. The latter are determined using an empirical threshold value of 20 $\mu g/m^3$ for better reproducing the measured light scattering coefficient (for details see [81, 93]). The chosen wavelength corresponds to the region of maximum sensitivity of human vision and it is thus considered the most appropriate

for visibility estimates. The water growth functions $f_S(RH)$, $f_L(RH)$, and $f_{SS}(RH)$ (subscripts "S", "L" and "SS" stand for small, large, and sea salt, respectively) are defined as the ratio between ambient and dry aerosol scattering coefficients (σ_{sp}) of the individual component. Rayleigh scattering by gases (RS, in Mm^{-1}) depends on atmospheric density according to temperature and pressure values at the investigated site.

In this work, a tailored equation for σ_{ext} estimation is presented. On a conceptual basis, the proposed equation recalls the IMPROVE revised algorithm in ascribing different importance to various particle size classes. As already mentioned, the aim of this approach was to reduce any possible additional uncertainty rising from the application of the IMPROVE coefficients to PM datasets collected at sites with different aerosol properties compared to IMPROVE areas.

In detail, in the tailored approach developed in this work the following changes were implemented:

- Site-specific dry mass extinction efficiencies (c_i, in m^2/g) were calculated by discrete dipole approximation (see sub-section 2.3.3 for details) using aerosol size distributions previously measured in Milan as input data [94, 95].

- Component-specific water growth functions $f(RH)_i$ were derived (see sub-section 2.3.4) to take into account any discrepancy among AMSUL, AMNIT, and OM hygroscopic behaviour. In contrast, the IMPROVE method infers $f_S(RH)$ and $f_L(RH)$ from calculations based on AMSUL properties and applies it to both AMSUL and AMNIT (while OM is considered non hygroscopic).

- Clear-air Rayleigh scattering (RS=σ_{sg}) was estimated according to Watson [26] from atmospheric temperature (T) and pressue (P) registered for each sampling interval at Milan monitoring station. Conversely, in the IMPROVE revised algorithm it is usually calculated from site-specific annual mean data.

- $[AMSUL] = 1.375 \cdot [SO_4^{2-}]$ and $[AMNIT] = 1.29 \cdot [NO_3^-]$ as ionic balance demonstrates that in Milan sulphate and nitrate anions are typically completely neutralized by ammonium in atmospheric aerosol. At the IMPROVE sites, the neutralization assumption is made (only sulphate and nitrate concentrations are available), although spatial-temporal variations in the degree of sulphate neutralization can occur as reported by Hand et al. [96].

- $[OM] = 1.6 \cdot [OC]$ where the OC-to-OM conversion factor was 1.6, as the one applied in Milan by Vecchi et al. [92]. It is 1.8 in the IMPROVE revised algorithm (and it was 1.4 in the IMPROVE original equation).

- Fine soil [FS] was calculated according to Vecchi et al. [97]: $[FS] = 1.15 \cdot (1.89[Al]+2.14[Si]+1.4[Ca^*]+1.67[Ti]+1.2[K^*]+1.36[Fe^*])$, where X*=X/EF(X) is the natural component of the X-th element evaluated considering its enrichment factor EF(X) as reported in Marcazzan et al. [98].

- The aerosol absorption coefficient σ_{ap} (measured with PP_UniMI - see sub-section 2.2.1) was inserted in place of 10[EC]. The latter is used in the IMPROVE revised approach under the assumption that the absorption coefficient in atmospheric aerosol samples is entirely due to light-absorbing carbon.
  The aerosol absorption coefficient at the wavelength of 550 nm was derived from the one measured at 532 nm with PP_UniMI using an Absorption Ångström Exponent (AAE - see sub-section 1.2.2) of 1. It should be noted that thanks to the availability of direct σ_{ap} measurements, two main issues could be likely avoided. Besides the problems in EC quantification [99, 100], the difficulties in the assessment of the characteristics influencing its absorption properties (e.g. complex refractive index, size, shape, mixing state) make the direct measurement of σ_{ap} the easiest way to quantify aerosol absorption contribution. Note that in this way the contribution of absorbing species to scattering is neglected.

Finally, the reconstructed light extinction equation used in this work is:

$$\begin{aligned}\sigma_{ext} = {} & c_1 \cdot f(RH)_1 \cdot [AMSUL] + c_2 \cdot f(RH)_2 \cdot [AMNIT] + c_3 \cdot f(RH)_3 \cdot [OM] \\ & + c_4 \cdot [FS] + 0.60 \cdot [CM] + RS + \sigma_{ap} + 0.33 \cdot [NO_2(ppb)]\end{aligned} \tag{2.27}$$

where inputs in square brackets are concentrations (in $\mu g/m^3$) of the considered $PM_{2.5}$ components.
The tailored equation presented in this work was developed without the splitting of AMSUL, AMNIT, and OM between small and large modes. Indeed, since nephelometer data were not available at our sampling site nor in the regional monitoring network, it was impossible to verify that the empirical threshold value of 20 $\mu g/m^3$ suggested for U.S. sites was suitable also for the urban aerosol in Milan. As explained in sub-sections 2.3.3 and 2.3.4, both dry mass extinction efficiencies and water growth functions were modified tailoring them according to the specificity of Milan urban site and taking into account the mass fractions of each mode for every component of interest. Thus, a direct comparison between the IMPROVE revised and tailored coefficients was not straightforward while it was possible for σ_{ext}, obtaining a very small discrepancy (less than 5%).
In the following sub-sections, the methods used to obtain all the quantities in the tailored equation will be presented. Hereafter, subscripts "i" and "k" will denote each component and mode, respectively. Furthermore, whenever relative humidity (RH) dependence is not explicitly indicated in the right-hand of the equations, quantities are

referred to their dry state. Opposite, for sake of simplicity, $\sigma_{ext}(RH)$ is often indicated as σ_{ext} even though it always represents ambient (reconstructed) light extinction.

2.3.3 Calculation of the tailored dry mass extinction efficiencies

Dry single-particle extinction efficiencies $Q_{ext,i,k}$ were obtained applying the code ADDA (`https://code.google.com/archive/p/a-dda/`,[101]) to dry mass size distributions (hereafter called MSDs) of the considered aerosol components, and using complex refractive indices (α_i) taken from literature [26]. Briefly, ADDA implements the discrete dipole approximation (DDA), which is a general approach to calculate light scattering and absorption by particles of arbitrary shape and composition. This code is reliable only for r/λ ratios smaller than 2 [74], corresponding to $r \approx 1.1\,\mu$m at λ=550 nm. This condition is verified for dry geometric mean radii $r_{i,k}$ of all the modes used in the fine fraction (i.e. aerodynamic diameter $d_{ae} < 2.5\,\mu$m); the approximation is thus valid for $PM_{2.5}$ samples. Moreover, $Q_{ext,i,k}$ were calculated under the assumption that aerosol particles are homogeneous spheres, as done in Mie calculations performed to obtain coefficients in the IMPROVE revised formula.

Ambient size distributions measured in Milan were used to compute the tailored coefficients; in particular, MSDs for each component of interest were obtained as averages of multiple size-segregated samples collected at the same location a few years ago and already reported in [94, 95]. As no relevant changes in sources impacting on Milan monitoring site are expected, average ambient MSDs used in this work can be considered still representative of wintertime aerosol properties in Milan. In the computation, size distributions of sulphate, nitrate, OC and Ti were employed. Following literature works [102, 103, 104], Ti was chosen as tracer for the soil dust component as Si was not available in the dataset employed for the computation. It is noteworthy that - besides being in ionic balance with ammonium - sulphate and nitrate had MSD similar to that of ammonium confirming that AMSUL and AMNIT were the correct chemical form to be considered for wintertime aerosol collected in Milan (as done in sub-section 2.3.2). Dry MSDs were retrieved from ambient size distributions taking into account $\overline{RH}$, i.e. the average relative humidity during the sampling campaign in which MSDs used in this work were obtained. Dry geometric mean radii and standard deviations of the modes were respectively calculated from ambient aerodynamic (subscript "ae")

ones as:

$$r_{i,k} = \frac{r_{ae}(\overline{RH})_{i,k}}{\sqrt{\rho_{eff}(\overline{RH})_i}} \cdot \frac{1}{g(\overline{RH})_i} \tag{2.28}$$

$$\sigma_{i,k} = \frac{\sigma_{ae}(\overline{RH})_{i,k}}{\sqrt{\rho_{eff}(\overline{RH})_i}} \cdot \frac{1}{g(\overline{RH})_i} \tag{2.29}$$

where $g(\overline{RH})_i = \frac{r(\overline{RH})_i}{r_i}$ is the hygroscopic growth factor (that takes into account water uptake by some aerosol components), and

$$\rho_{eff}(\overline{RH})_i = v_i\rho_i + v_w\rho_w \tag{2.30}$$

is the effective species density (volume fraction $v_i = \left(\frac{1}{g(\overline{RH})_i}\right)^3$; subscript "w" stands for water).

For non-hygroscopic aerosol, g_i=1 and $\rho_{eff,i} = \rho_i$; densities of pure compounds were taken from Watson [26]. Hygroscopicity was here considered only for AMSUL, AMNIT, and water soluble OM (WSOM) since, as far as the author knows, for other PM components there is no clear evidence of such behaviour. $g(\overline{RH})_i$ were taken from literature ([8, 105, 106] for AMSUL, AMNIT and WSOM, respectively).

Data concerning geometric mean radii ($r_{i,k}$), geometric standard deviations ($\sigma_{i,k}$) and mass fractions of the modes ($m_{i,k}/\sum_k m_{i,k}$, where $\sum_k m_{i,k}$ represents the sum on modes in $PM_{2.5}$), along with densities (ρ_i) of the considered chemical components, were then combined to infer dry mass extinction efficiencies $c_{i,k} = \frac{\sigma_{ext,i,k}}{m_{i,k}}$ (where $m_{i,k}$ is the mass of the i-th component in the k-th mode).

For each mode of the i-th component, the dry extinction coefficient can be obtained as

$$\sigma_{ext,i,k} = Q_{ext,i,k}\pi r_{i,k}^2 N_{i,k} \tag{2.31}$$

(see equation 1.21), where

$$N_{i,k} = \frac{m_{i,k}}{\frac{4}{3}\pi\rho_i r_{i,k}^3 \exp\left(\frac{9}{2}\left(\log\sigma_{i,k}\right)^2\right)} \tag{2.32}$$

[107] is the number of particles of the i-th component in the k-th mode, assuming a log-normal distribution.

Summing up the contributions from each mode, the final expression for c_i (i.e. site-specific dry mass extinction efficiency) is then:

$$c_i = \sum_k \chi_{i,k} = \sum_k \frac{m_{i,k}}{\sum_j m_{i,j}} \cdot c_{i,k} = \sum_k \frac{m_{i,k}}{\sum_j m_{i,j}} \cdot \left[\frac{3}{4\rho_i} \cdot \frac{Q_{ext,i,k}}{r_{i,k}\exp\left(\frac{9}{2}\left(\log\sigma_{i,k}\right)^2\right)}\right] \tag{2.33}$$

where $\chi_{i,k}$ is hereafter called weighted dry mass extinction efficiency. As a first approximation, due to the lack of information about aerosol mixing state, WSOM and

the remaining water insoluble organic fraction (WIOM) were considered as externally mixed (as usually done for all other aerosol components in the IMPROVE algorithm). Data from a previous campaign performed in Milan during winter season showed that water soluble organic carbon (WSOC) and the OC insoluble fraction (WIOC) represented 75% and 25% of fine OC concentration, respectively (data not published). Thus, considering these percentages, OM was split in WIOM and WSOM, assuming an OM-to-OC conversion factor of 1.6 for both insoluble and soluble OC fractions. In addition, $c_{i,k}$ were calculated separately for WIOM and WSOM: for the former, OC ambient MSD was considered equal to dry MSD, and for the latter, dry MSD was evaluated as previously reported for AMSUL and AMNIT. Finally the value of OM dry mass extinction efficiency was obtained weighing these $c_{i,k}$ for the percentages (p) reported above:

$$c_{OM} = \sum_k \left[\left(m_{i,k} / \sum_j m_{i,j} \right) \cdot \left(p_{WIOM,k} c_{WIOM,k} + p_{WSOM,k} c_{WSOM,k} \right) \right] \tag{2.34}$$

Table 2.6 summarizes dry single-particle extinction efficiencies ($Q_{ext,i,k}$) computed for the aerosol modes reported in [94, 95].

Table 2.6: Dry (at RH=0%) single-particle extinction efficiencies ($Q_{ext,i,k}$) calculated in this work; d_{ae} stands for the ambient geometric mean aerodynamic diameter of each mode (k) of each component (i) retrieved by ambient size distributions measured in Milan at average relative humidity $\overline{RH}$.

Mode	$Q_{ext,i,k}$				
	AMSUL	AMNIT	WSOM	WIOM	Soil
mode 1 ($d_{ae} < 0.4\,\mu$m)	0.38	0.55	0.71	0.71	0.10
mode 2 ($0.4\,\mu\text{m} < d_{ae} < 0.8\,\mu$m)	3.43	3.73	3.77	3.88	
mode 3 ($d_{ae} \approx 1.0\,\mu$m)					3.84

For all components, mode 2 (droplet mode - see Section 1.1) is characterized by the largest extinction efficiency. This is consistent with results by Gao et al. [108], who found that the droplet mode was the main responsible for PM extinction. It should be considered that the weighted dry mass extinction efficiency of each species mode ($\chi_{i,k}$) is the quantity indicating the mode with the highest contribution to total extinction; indeed, it depends both on $Q_{ext,i,k}$ and on the species mass fraction explained by each mode (i.e. $m_{i,k} / \sum_k m_{i,k}$). Even observing $\chi_{i,k}$ (Table 2.7), the droplet mode appears to be the one which gives the major contribution to c_i for all species.

Table 2.7: Weighted dry (at RH=0%) mass extinction efficiencies ($\chi_{i,k}$) calculated in this work; d_{ae} stands for the ambient geometric mean aerodynamic diameter of each mode (k) of each component (i) retrieved by ambient size distributions measured in Milan at average relative humidity $\overline{RH}$.

Mode	$\chi_{i,k}$ (m^2/g)			
	AMSUL	AMNIT	OM	Soil
mode 1 ($d_{ae} < 0.4\,\mu m$)	0.60	0.69	1.01	0.09
mode 2 ($0.4\,\mu m < d_{ae} < 0.8\,\mu m$)	3.85	4.47	5.07	
mode 3 ($d_{ae} \approx 1.0\,\mu m$)				3.13

Total dry mass extinction efficiencies c_i are intensive quantities that represent the extinction properties of each atmospheric component.
In Table 2.8 dry mass extinction efficiencies obtained in this study are reported.

Table 2.8: Dry (at RH=0%) mass extinction efficiencies (c_i, in m^2/g) calculated in this work (value±uncertainty) and reported in Hand and Malm [90] (average±standard deviation); all calculations are referred to λ=550 nm.

Component	c_i (m^2/g)	
	this work	Hand and Malm, 2007 [90]
AMSUL	4.44±0.44	2.1±0.7
AMNIT	5.16±0.52	-
OM	6.08±0.61	5.6±1.5
FS	3.21±0.32	3.4±0.5

It is noteworthy that a comparison with individual coefficients used in the IMPROVE revised equation is not possible because the latter implements a split-component representation. However, dry mass extinction efficiencies calculated in this work and those reviewed by Hand and Malm [90] for the so-called theoretical method were obtained using a similar approach and a comparison can be exploited. Values shown in Table 2.8 fall within the range of those reported in the review as far as OM and FS are concerned, while for AMSUL the difference is larger than 3 standard deviations, and AMNIT is not considered in the review. The discrepancy in c_i calculated for AMSUL is likely to be ascribed to differences in mass relative contributions of the modes detected at a polluted urban site like Milan compared to U.S. locations where the studies

cited in the review were performed (mostly national parks). As far as other parameters involved in the computation are concerned, densities and refractive indices used in this work were taken from Watson [26] and they differed only slightly from those used by Pitchford et al. [81]. Moreover, although using different codes, the geometric mean radii of the size distributions used in this paper and those reported by Pitchford et al. [81] are fairly similar, even if there are differences in geometric standard deviations of modes.

2.3.4 Retrieval of tailored water growth functions

$f(RH)_i = \frac{\sigma_{sp}(RH)_i}{\sigma_{sp,i}}$ are water growth functions (also called relative humidity scattering enhancement factors [109] or humidification factors [110]), introduced because some aerosol components enhance their actual ambient scattering coefficient compared to the dry one as a consequence of particle increased size (represented by $g(RH)_i$). In order to calculate $f(RH)_i$, effective refractive indices $\alpha_{eff}(RH)_i = v_i\alpha_i + v_w\alpha_w$ and wet mass size distributions - derived varying RH from 0% to 85-95% (depending on the available information about $g(RH)_i$) with steps of 5% - were used for each hygroscopic component. The upper branch of $g(RH)_i$ hysteresis loop was taken into account as it corresponded to aerosol in its most hydrated state, internally and homogeneously mixed with water. Following Lowenthal et al. [93], this branch was assumed to be the most appropriate considering the typical atmospheric conditions occurring in the Po Valley during winter season, characterized by high RH (e.g. above 50% in more than 80% of cases in the period November-December 2015). Through the code ADDA, water growth functions were obtained as:

$$f(RH)_i = \frac{\sigma_{sp}(RH)_i}{\sigma_{sp,i}} = \frac{\sum_k \left[Q_{sp}(RH)_{i,k} r(RH)_{i,k}^2 \cdot \frac{m_{i,k}/\sum_j m_{i,j}}{r_{i,k}^3 \exp\left(\frac{9}{2}\left(\log\sigma_{i,k}\right)^2\right)} \right]}{\sum_k \left[Q_{sp,i,k} r_{i,k}^2 \cdot \frac{m_{i,k}/\sum_j m_{i,j}}{r_{i,k}^3 \exp\left(\frac{9}{2}\left(\log\sigma_{i,k}\right)^2\right)} \right]} \tag{2.35}$$

where Q_{sp} are single-particle scattering efficiencies. Resulting values were then fitted with proper functions and applied to data corresponding to RH up to 95%. In agreement with the IMPROVE approach, the highest RH value considered was RH=95% due to the large uncertainties affecting measurements at higher RH values.

In this study, the use of fitted values for $f(RH)_i$ rather than those theoretically obtained was preferred in order to retrieve $f(RH)_i$ smooth functions, thus applicable to all RH values. Note that hygroscopicity was considered active only for RH higher than the efflorescence point of each species. Following previous literature findings, efflorescence relative humidity (ERH) was considered to be 35% for AMSUL [8], whereas no ERH was used for AMNIT ([105] and references therein) and OM [106] since no efflorescence was observed in the majority of cases. Water growth functions obtained

in this work are represented in Figure 2.17. Again, no direct comparison was possible with the split-component $f(RH)$ given in the IMPROVE revised equation.

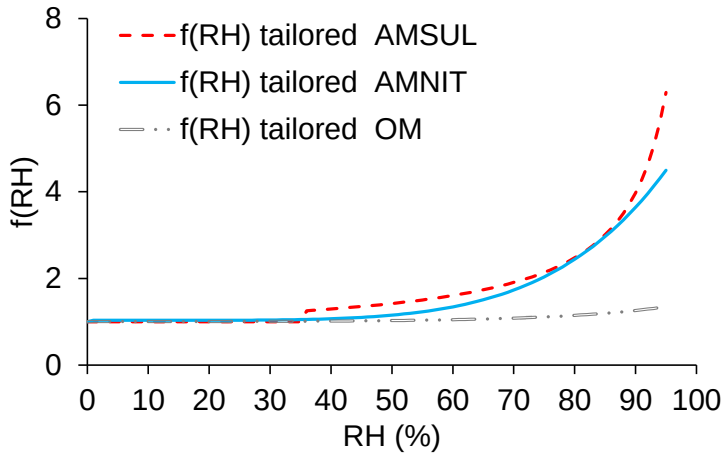

Figure 2.17: Tailored water growth functions derived in this work; all calculations are referred to λ=550 nm [91].

The tailored approach developed to reconstruct atmospheric light extinction at an urban site was applied to a completely characterised PM_1 dataset collected in 2012 in Milan [111]. The results obtained are extensively discussed in Section 3.4.

Conclusions

In this Chapter, several methodologies developed and exploited in this thesis were presented.
In particular, on-line instrumentation extensively used in sampling campaigns and laboratory experiments was analysed in detail; truncation error correction in scattering measurements was deeply investigated and in-situ techniques to measure aerosol absorption coefficient were compared to filter-based methods (both on-line and off-line), obtaining results that could be of large interest for the scientific community and deserve further investigation.
In addition, the tailoring of the widespread IMPROVE algorithm used to reconstruct atmospheric extinction and visibility highlighted the need to verify the model coefficients taking into account site-specific and season dependent aerosol properties.

Chapter 3

Applications

Introduction

In this Chapter, several applications of the methodologies reported in Chapter 2 are presented. In particular, on-line instruments data, analysed according to the investigated approaches, were employed and combined. Furthermore, results obtained from measurements performed with the polar photometer PP_UniMI on samples collected during various campaigns are reported. Finally, an application of the tailored approach for the reconstruction of atmospheric extinction to a PM_1 dataset and coupled with a source apportionment study is presented.

3.1 Optical properties during wintertime in Rome (Italy): the CARE experiment

The international collaborative project CARE (Carbonaceous Aerosol in Rome and Environs) was carried out in Rome (Italy) using a variety of instruments and techniques in order to obtain a comprehensive and highly time-resolved picture of the aerosol properties at a Mediterranean urban background site. An overview of measurements performed and methodologies applied during the CARE campaign is reported in Costabile et al. [112]. Thirteen research groups took part to the experiment. In particular, besides optical analyses performed at the Department of Physics of the University of Milan, data used in this work were acquired and analised by the Institute of Atmospheric Science and Climate of the National Research Council ISAC-CNR (Rome), the National Institute of Nuclear Physics - Laboratory of Nuclear Techniques Applied to Cultural Heritage INFN-LABEC (Florence - Italy), the ENEA – SSPT – MET – Atmospheric Pollution Laboratory INAT (Bologna - Italy), and the Leibniz Institute for Tropospheric Research TROPOS (Leipzig - Germany).

During this PhD work, a method was developed for the identification and classification of aerosol types and their phenomenology exploiting all the available information about high-time resolved optical properties, chemical composition, and size distribution of atmospheric aerosol. The main objective was to find out one or more possible combinations of intensive optical parameters that can be used as an original tool to identify aerosols with different origins, with the support of chemical and size information [113].
In addition, hourly $PM_{2.5}$ streaker samples and daily PM_{10} aerosol samples collected on quartz-fibre filters in the framework of the CARE experiment were analysed off-line with PP_UniMI in order to retrieve aerosol absorption coefficient at different time resolutions.

3.1.1 Measurement campaign and aerosol characterisation techniques

The CARE experiment took place from January 27th to February 28th 2017 at an urban background site in downtown Rome (Italy). Due to its geographical position (in the middle of the Mediterranean Sea) and its meteorological conditions, this site can experience the advection of air masses transported from the Sahara Desert [114, 115, 116, 117] or from the sea [118]. The CARE measurement site is also affected by local urban sources such as vehicular traffic and biomass burning for heating and cooking [112, 119].
A detailed list of the instruments deployed during the CARE experiment and of their operating conditions can be found in Costabile et al. [112]. Only a short summary of the techniques whose results were used in this work is reported in the following. Where not specified, instruments were operated at ambient relative humidity (RH).

Wavelength-dependent optical properties

On-line instruments continuously measured PM_{10} multi-wavelength scattering and absorption coefficients with a time resolution of 1 minute. In this work, 5-minute averages of each parameter were considered in order to reduce data noise.
A 3-wavelength integrating Nephelometer (Aurora 3000, Ecotech) measured dry aerosol scattering coefficient σ_{sp} at 450, 525, and 635 nm. Total scattering coefficients were corrected for truncation error according to Müller et al. [36].
On-line dry aerosol absorption coefficient σ_{ap} at 7 wavelengths (370, 470, 520, 590, 660, 880, and 950 nm) was retrieved by equivalent Black Carbon (eBC) concentrations measured by a dual-spot Aethalometer (AE33, Magee Scientific) [63].
Moreover, a Multi-Angle Absorption Photometer (MAAP, Thermo Scientific) was used to measure eBC concentration at RH$<$30%. From these data, $\sigma_{ap}(637)$ was retrieved

using the Mass Absorption Cross section (MAC) of 6.6 m^2/g set in the MAAP and a wavelength correction factor of 1.05 as reported in Müller et al. [29].
In addition to on-line instrumentation measuring aerosol optical properties, aerosol samples collected at hourly and daily time resolution (by a streaker sampler and a low-volume sampler, respectively) were analysed off-line as for multi-wavelength aerosol absorption coefficient by PP_UniMI (see sub-section 2.2.1).
As explained in sub-section 2.2.4, the AE33 Aethalometer gives eBC concentration using instrument specific MAC values at seven wavelengths (e.g. 10.35 m^2/g at 660 nm). The instrument internal software originally retrieves $\sigma_{ap,AE}(\lambda)$ starting from attenuation measurements and correcting them for loading (k parameter) and multiple scattering (C factor) effects (see Equation 2.10). Literature studies (e.g. [67, 70]) also pointed out the site-specificity and possible wavelength dependence of these effects. In particular, as evidenced by some recent works (e.g. [120]), the fixed C factor equal to 1.57 used in AE33 to convert attenuation into absorption can lead to a significant overestimation of the $\sigma_{ap}(\lambda)$ by this instrument. Aiming at reducing this bias, in this work the availability of parallel optical measurements was exploited and - following Collaud Coen et al. [67] - the loading-corrected C factor (here C_{corr}) was obtained via a linear regression analysis between the attenuation coefficient (loading-corrected) $\sigma_{ATN,k}(660)$ and $\sigma_{ap}(637)$ given by AE33 and MAAP, respectively. It is known from the literature [121] that when eBC concentration (and therefore $\sigma_{ap}(637)$) is high, the MAAP response lacks in linearity; in this case, a non-linear behaviour was observed at $\sigma_{ap}(637) > 100$ Mm^{-1}, thus only MAAP data giving $\sigma_{ap}(637) < 100$ Mm^{-1} were considered in the regression $\sigma_{ATN,k}(660)$ vs $\sigma_{ap}(637)$. The loading-corrected attenuation coefficient $\sigma_{ATN,k}(660)$ was retrieved following Equation 2.13: in particular, at 660 nm:

$$\sigma_{ATN,k}(660) = \sigma_{ap,AE}(660) \cdot C = [eBC(660)] \cdot MAC(660) \cdot C = [eBC(660)] \cdot 10.35 \cdot 1.57 \tag{3.1}$$

The linear fit (performed with a Deming regression) had intercept compatible with zero (within 95% confidence interval) and a slope (i.e. the C_{corr}) of 2.66 that was used to correct the AE33 absorption coefficients at all wavelengths.
The corrected $\sigma_{ap,corr}(\lambda)$ were calculated as:

$$\sigma_{ap,corr}(\lambda) = \sigma_{ap,AE}(\lambda) \cdot C/C_{corr} = \sigma_{ap,AE}(\lambda) \cdot 1.57/2.66 \tag{3.2}$$

For the sake of simplicity, $\sigma_{ap,corr}(\lambda)$ calculated with this procedure will be referred to as $\sigma_{ap}(\lambda)$ in the following.

Chemical analyses

Both on-line and off-line techniques were used in the experiment to characterise aerosol

chemical composition (elements, carbonaceous fractions, non-refractory components) with time resolutions from 30 minutes to 2 hours and on different size fractions.
$PM_{2.5}$ samples collected using a streaker sampler at 1 h time resolution were analysed off-line as for elemental composition by Particle Induced X-Ray Emission (PIXE) analysis [122]. This technique allows the detection and quantification of Z>10 elements.
A Sunset Field Thermal-Optical Analyser (Model-4 Semi-Continuous OC-EC Field Analyzer – Sunset Laboratory inc.) measured the concentrations of $PM_{2.5}$ carbonaceous fractions (i.e. elemental carbon – EC – and organic carbon – OC) with a time resolution of 2 hours.
An Aerodyne Aerosol Chemical Speciation Monitor (ACSM [123]) was used to obtain on-line the non-refractory chemical components (organic matter, sulphate, ammonium, nitrate, and chloride ions) of the PM_1 fraction. The instrument operated at RH<30% with 30-minute time resolution; here, hourly averages were considered. As an additional information, concentrations of organic aerosol (OA) apportioned by the SoFi software [124] among Hydrocarbon-like Organic Aerosol (HOA, often associated to traffic emissions), Oxygenated Organic Aerosol (OOA, typically related to secondary aerosol), and Biomass Burning Organic Aerosol (BBOA) were considered.

Particle Size distributions

Particle number size distribution (PNSD), was obtained combining data from a Scanning Mobility Particle Sizer (TROPOS-SMPS) and an Aerodynamic Particle Sizer (APS, TSI). Both instruments were operated with a time resolution of 5 minutes. The SMPS and APS covered the range 8-700 nm in electrical mobility diameter (d_m) and 0.5-20 μm in aerodynamic diameter (d_{ae}), respectively (see Section 1.1 for definitions of equivalent diameters). To obtain a unique size distribution in the range 8 nm $\leq d_m \leq$ 10 μm, APS data were converted to a d_m-based size distribution (i.e $dN/d\log(d_m)$) and then merged to those of the SMPS following the procedure described in Khlystov et al. [125]. More details about the PNSD calculation can be found in Costabile et al. [112] and in Alas et al. [126].

3.1.2 Classification of aerosol types

Direct measurements of aerosol optical properties are not usually carried out by by air quality (AQ) monitoring networks, although large uncertainties still affect estimates of the impact of atmospheric aerosol on Earth radiative budget. Aerosol optical properties are related to the size and composition of the particles, as well as to their mixing state (e.g. [24] - see Section 1.2). Spectral scattering and absorption properties depend on the aerosol type; therefore, simultaneous measurements of multi-wavelength aerosol optical properties, chemical composition, and size distribution can improve our

knowledge about atmospheric particles impact on both the radiative forcing and air quality.

Several classification schemes have been proposed in the literature to distinguish aerosol types. Most of these methods make use of column-integrated properties usually retrieved from remote-sensing data, such as those provided by the global network of ground-based sun and sky radiometers AERONET (Aerosol Robotic Network) or obtained by Sun photometers (e.g. [127, 115, 128, 129, 130, 131, 132, 133]). There are also fewer studies dealing with in-situ measurements of optical properties, both ground-based and airborne (e.g. [134, 135, 136, 137, 138]). As pointed out by Schmeisser et al. [139], the majority of the existing classification schemes work well at sites where the aerosol characteristics are fairly homogeneous, while their performance is worse in areas that experience a heterogeneity of particle sources and/or episodes characterised by aerosol transported from peculiar regions (such as deserts or oceans). The methods proposed to distinguish PM types are sometimes supported by chemical composition, size distribution data, or back trajectory analyses; however, these pieces of information are not usually included in the classifying approaches themselves.

In this work, a phenomenology of specific episodes characterised by aerosol with different characteristics is given exploiting all the available information about high-time resolved optical properties, chemical composition and size distribution of atmospheric aerosol. The main objective is to find out one or more possible combinations of intensive optical parameters that can be used as a tool to identify aerosols with different origin.

Several studies in recent literature (e.g. [140, 141, 112]) pointed out the importance of shorter time scale ($<$1h) to study atmospheric processes and source variability; the CARE experiment was based on highly time-resolved aerosol optical properties

In this work, graphical classification schemes reported in the literature were applied and some were newly developed to visually distinguish specific episodes and aerosol types via 2D plots of optical parameters. These representations appear useful to have a first hint on the typologies of particles observed during a campaign, even though they are not able to clearly disentangle different contributions, especially when atmospheric aerosol is dominated by mixtures of particles emitted by a variety of sources. In these cases, only the exploitation of multi-wavelength optical properties measured with high-time resolution allows to identify the dominant contributions, as it is shown in the following.

The novelties with respect to previous works and existing aerosol classification schemes are represented by: 1) the identification of an episode-discriminating intensive optical parameter; 2) the combined analysis of temporal patterns of several optical properties and their spectral behaviour; 3) the development of new graphical schemes, and 4) the

exploitation of high-time resolution measurements in addition to a complete chemical speciation and measured size distributions.

Calculation of intensive optical parameters

For the sake of clarity, Table 3.1 reports a synthesis of the optical parameters used in the following and their definitions (see also Section 1.2). A description of all quantities and details on how they were calculated is given in this paragraph.

Table 3.1: Intensive optical parameters used in this work.

Parameter name	Definition	Symbol
Single Scattering Albedo	$\sigma_{sp}(\lambda)/\sigma_{ep}(\lambda)$	$SSA(\lambda)$
Single Scattering co-albedo	$\sigma_{ap}(\lambda)/\sigma_{ep}(\lambda) = 1 - SSA(\lambda)$	$SSCA(\lambda)$
Scattering Ångström Exponent	$-\left[\ln\left(\sigma_{sp}(\lambda_1)/\sigma_{sp}(\lambda_2)\right)\right] / \ln\left(\lambda_1/\lambda_2\right)$	$SAE(\lambda_1, \lambda_2)$
Absorption Ångström Exponent	$-\left[\ln\left(\sigma_{ap}(\lambda_1)/\sigma_{ap}(\lambda_2)\right)\right] / \ln\left(\lambda_1/\lambda_2\right)$	$AAE(\lambda_1, \lambda_2)$
Extinction Ångström Exponent	$-\left[\ln\left(\sigma_{ep}(\lambda_1)/\sigma_{ep}(\lambda_2)\right)\right] / \ln\left(\lambda_1/\lambda_2\right)$	$EAE(\lambda_1, \lambda_2)$
Absorption spectral curvature	$2 \cdot \frac{AAE(\lambda_1,\lambda_2) - AAE(\lambda_2,\lambda_3)}{\ln(\lambda_3/\lambda_1)}$	$dAAE(\lambda_1, \lambda_2, \lambda_3)$
Single Scattering co-albedo Ångström Exponent	$AAE(\lambda_1, \lambda_2) - EAE(\lambda_1, \lambda_2)$	$SSCAAE(\lambda_1, \lambda_2)$

Wavelength dependencies of scattering and absorption coefficients have been used in literature (e.g. [132, 137]) to distinguish different aerosol types. Indeed, while Scattering Ångström Exponent SAE is mainly related to particle size, Absorption Ångström Exponent AAE is more linked to aerosol composition, even though it is influenced by particle size distribution as well. Consequently, the combination of these two parameters can provide information about the origin and properties of the studied aerosol.

In order to highlight possible stronger or weaker dependencies of optical properties in some spectral regions, SAE and AAE were here calculated using different wavelength pairs following Equation 1.30 and will be referred to as $SAE(\lambda_1, \lambda_2)$ and $AAE(\lambda_1, \lambda_2)$, respectively, where $\lambda_1 < \lambda_2$. Moreover, the Extinction Ångström Exponent $EAE(\lambda_1, \lambda_2)$ was inferred from extinction coefficient $\sigma_{ep}(\lambda)$ calculated at Nephelometer wavelengths (i.e. 450, 525, and 635 nm) as $\sigma_{ep}(\lambda) = \sigma_{sp}(\lambda) + \sigma_{ap}(\lambda)$.

Due to the difference in the operating wavelengths of instrumentation used for scat-

tering and absorption measurements, $\sigma_{ap}(\lambda)$ was reported to 450, 525, and 635 nm (i.e. the three operating λs of the Nephelometer). To do so, the quantity $AAE(fit)$ was computed via a power-law fit of all 7-λ $\sigma_{ap}(\lambda)$. For each of the three operating λs of the Nephelometer, the resulting $\sigma_{ap}(\lambda)$ was then obtained as $\sigma_{ap}(\lambda) = \sigma_{ap}(\lambda_{ref}) \cdot (\lambda/\lambda_{ref})^{-AAE(fit)}$ (see Equation 1.29), where λ_{ref} is the nearest wavelength at which absorption data were available (i.e. 470, 520, and 660 nm from the AE33).
Moreover, in order to better analyse the spectral behaviour of $\sigma_{ap}(\lambda)$, variation in AAE calculated employing different wavelength pairs was considered in the present work. Indeed, even though the absorption wavelength dependence is usually represented by a power law (see sub-section 1.2.2), it has to be noted that, especially when different aerosol components (e.g. Black Carbon, Brown Carbon and mineral dust) contribute to light absorption, the spectral behaviour can be more complicated yielding also curvature (high order terms) as pointed out e.g. by Eck et al. [142], Schuster et al. [143], and Moosmüller and Chakrabarty [144]. The parameter used to quantify this effect will be hereafter referred to as $dAAE(\lambda_1, \lambda_2, \lambda_3)$; it represents the spectral curvature of $\sigma_{ap}(\lambda)$ computed as the derivative of AAE as a function of $\ln(\lambda)$. This calculation is similar to the one performed to derive the curvature of Aerosol Optical Depth (AOD) often used by the AERONET network as a proxy for particle size [145, 142, 143]. $dAAE(\lambda_1, \lambda_2, \lambda_3)$ was calculated as:

$$dAAE(\lambda_1, \lambda_2, \lambda_3) = 2 \cdot \frac{AAE(\lambda_1, \lambda_2) - AAE(\lambda_2, \lambda_3)}{\ln(\lambda_3/\lambda_1)} \tag{3.3}$$

where $\lambda_1 < \lambda_2 < \lambda_3$.
It is noteworthy that several $dAAE$ were calculated using different λ combinations. Finally, $dAAE(450, 635, 880)$ was selected as it responded well to absorption spectral variations; the extremes of the spectral range (λ=370 nm and λ=950 nm) were avoided in order to limit the possible bias ascribed to organics due to sampling artefacts as reported by Zotter et al. [146] at the shortest wavelength of 370 nm, and because λ=880 nm is the reference one used by the Aethalometer to retrieve eBC concentrations.
Aerosol absorption coefficients corrected for multiple scattering and adjusted for wavelength discrepancies were also used to calculate the Single Scattering Albedo SSA, representing the fraction of light extinction that is scattered (see Section 1.2). In the present work, SSA was retrieved at 450, 525, and 635 nm.
As pointed out by some authors (e.g. [144, 136, 147, 148]) also the wavelength dependence of the SSA might be useful to give hints on variations in aerosol size and composition, as it responds to both physical and chemical properties. Specifically, $dSSA/d\lambda$ can serve as an indicator of the aerosol type especially at sites where Saharan dust transports are detected [149, 134, 136, 138]. For instance, Valenzuela et al. [150] exploited spectral SSA to distinguish between so-called dust or non-dust periods, i.e. periods influenced or not by advections of aerosol from the Sahara Desert.

In this work, also the Single Scattering Albedo Ångström Exponent ($SSAAE$) was considered, computed according to Equation 1.33 [144].
Since extinction is usually dominated by scattering, $SSAAE$ is likely the difference between two quantities (SAE and EAE) with similar values. Moreover, in most cases SSA is expected to have a weak wavelength dependence and it is expected to be determined with high uncertainties: thus, it was no longer considered here. Opposite, in this work the wavelength dependence of the Single Scattering co-albedo $SSCA$ (i.e. 1-SSA), represented by the Single Scattering Co-Albedo Ångström Exponent ($SSCAAE$), was calculated according to Equation 1.34 [144]. It is noteworthy that co-albedo wavelength dependence does not depend on the relative contribution of absorption to extinction but only on the difference in their wavelength dependence. Moreover, being EAE comparable with SAE in most cases, $SSCAAE$ is sensitive to both particle size (via EAE) and composition (through AAE), thus it is itself a combination of intensive optical properties describing different aerosol characteristics. Thanks to this feature, in this work the key role of $SSCAAE$ in discriminating aerosol with peculiar properties detected during specific episodes was proved.
Please note that, for all parameters calculated with two wavelengths, the widest Nepehlometer λ range (450-635 nm) was used and considered in patterns reported in the following; however, calculations performed with other couples of wavelengths did not show significantly different features.
To further confirm the classified aerosol types, the well-known Aethalometer model (for detail see e.g. [151]) was applied to get an estimate of the fossil fuel (FF) and biomass burning (BB) contributions to the measured absorption coefficient. Indeed, the availability of multi-wavelength absorption coefficients retrieved by the AE33 high-time resolved data allowed the apportionment of such contributions, which helped validating data interpretations. The AAE for the Aethalometer model application were AAE(FF)=0.9 and AAE(BB)=1.68, as suggested by Zotter et al. [146] when site-specific values are lacking.

Temporal patterns of aerosol intensive optical properties – episodes and aerosol types identification

Temporal patterns of 1-h averaged $SSCAAE(450, 635)$, $SAE(450, 635)$, $AAE(450, 635)$, $dAAE(450, 525, 635)$, and $dAAE(450, 635, 880)$ are shown in Figure 3.1.
As already discussed, $SSCAAE$ is sensitive to both particle size and composition, thus very high or low values are likely representative of conditions involving aerosol with particular properties.
During the CARE experiment, $SSCAAE$ had a median value of 0.2 and the 5^{th} and 95^{th} quantiles equal to -0.1 and 1.2, respectively. It is noteworthy that $SSCAAE$ values appear to be significantly higher than the campaign average (0.3 ± 0.4) in some

periods. Indeed, three events with $SSCAAE(450, 635)$ values larger than 1 occurred in the periods 3-6 February (hereafter referred to as first event), 24-25 February (hereafter referred to as second event), and for a few hours in the afternoon of February 26^{th} (hereafter referred to as third event).
Temporal patterns of SAE, AAE, and $dAAE$ calculated with different λ triads (exploring different wavelength ranges) are analysed aiming at singling out any discrepancy in responses of these intensive properties among the three identified periods, which appear similar in terms of $SSCAAE$ but can be probably separated and associated to specific events thanks to additional pieces of information as shown in the following.

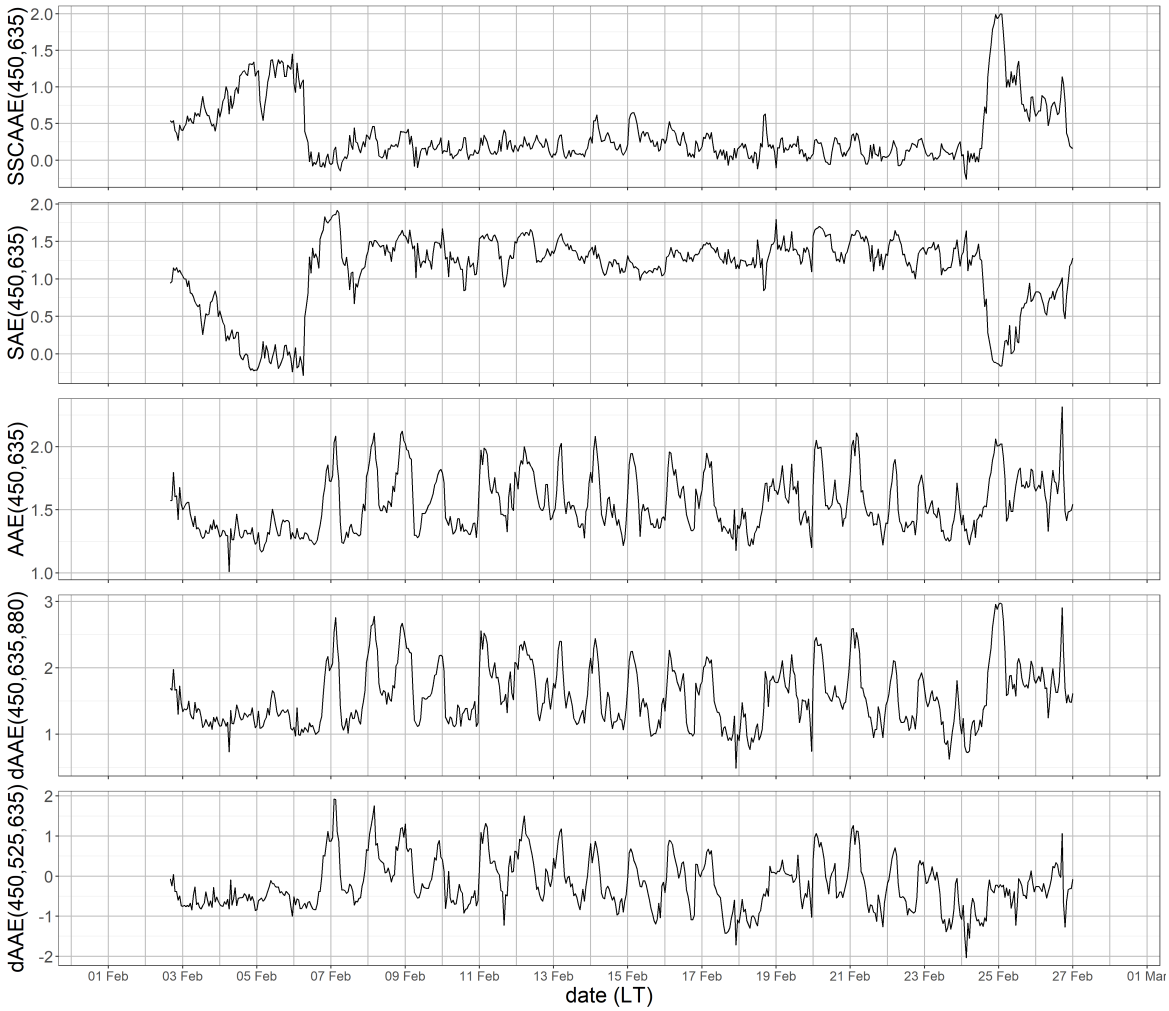

Figure 3.1: Temporal pattern of $SSCAAE(450, 635)$, $SAE(450, 635)$, $AAE(450, 635)$, $dAAE(450, 525, 635)$, and $dAAE(450, 635, 880)$ during the CARE campaign [113].

It is evident from the comparison of several intensive optical properties (Figure 3.1) that the three episodes identified via $SSCAAE$ temporal pattern represent events with different characteristics. Indeed, even though SAE is similar between the first two events and higher in the third one, AAE is low in the period 3-6 February, higher

during the second episode, and has its absolute maximum in correspondence to the last one. The absorption spectral curvature $dAAE(450, 635, 880)$ exhibits a pattern similar to the one of $AAE(450, 635)$, whereas $dAAE(450, 525, 635)$ appears to be not sensitive to the event occurring between February 24^{th} and 25^{th}.

In the following, the identified episodes and aerosol types will be analysed in detail making use also of chemical and size properties, in order to distinguish the aerosol origins and typologies responsible for the observed features in optical properties. In particular, periods characterised by advection-dominated and local sources-dominated aerosol types and aerosol with a mixed origin will be addressed.

As already mentioned, the first episode was characterised by high $SSCAAE$ values especially between February 3^{rd} and 6^{th}. As shown in Figure 3.1, $SAE(450, 635)$ was low (below 0.5), indicating the predominance of big particles. Moreover, $SSA(\lambda)$ was quite high (above 0.8) and exhibited a negative wavelength dependence thus further suggesting a significant contribution of large aerosol size, as also reported by Takemura et al. [152] for desert dust and (with a weaker wavelength dependence) sea salt. In addition, during this period $\sigma_{ap}(\lambda)$ was low and $AAE(450, 635)$ was small (about 1.3), thus suggesting that the absorption spectral behaviour was dominated by Black Carbon (BC) contribution from local fresh vehicular traffic sources, typically associated to AAE=1, as also shown by Costabile et al. [119] for the same campaign. Finally, both $dAAE(450, 525, 635)$ and $dAAE(450, 635, 880)$ were lower than the campaign average, confirming a weak wavelength dependence of absorption. Values of optical parameters registered during the first episode can be justified by findings by Costabile et al. [112, 119], who observed that the sub-micrometric aerosol fraction in this period was dominated by ultrafine BC-containing particles from fresh traffic emissions (typically characterised by small AAE), that were likely responsible for the measured values of $AAE(450, 635)$. Moreover, as pointed out by Costabile et al. [136], a mixture of ultrafine soot particles and coarse mode aerosol like the one observed in this case can show low SAE values.

Considering all these data together, a sea salt advection event occurring during the analysed period was hypothesised. Indeed, sea salt aerosol is generally characterised by quite large particles (from 0.5 to tens of micrometres [7]) and it does not typically contribute to $\sigma_{ap}(\lambda)$ wavelength dependence due its negligible absorption coefficient. The attribution of this event to desert dust (that can show similar SAE values) was excluded due to the higher AAE typically shown by this aerosol type.

To confirm the sea salt transport episode identified through optical parameters, also the particle number size distributions (PNSD) and chemical composition data were analysed.

From PNSDs, the number concentration of particles with aerodynamic diameters $d_{ae} <$

$1\,\mu$m, $d_{ae} < 2.5\,\mu$m, and $d_{ae} < 10\,\mu$m were calculated. From these values, total number of particles in the ranges $1\,\mu\text{m} < d_{ae} < 2.5\,\mu\text{m}$ and $2.5\,\mu\text{m} < d_{ae} < 10\,\mu\text{m}$, that will be referred to as intermodal and coarse fractions, respectively, were obtained. From February 3$^{\text{rd}}$ to February 6$^{\text{th}}$ a large increase in concentration of super-micrometric aerosol, i.e. intermodal and coarse fractions, was observed, in agreement with the indication given by SSA wavelength dependence and consistently with results shown by Costabile et al. [119].

During the sea salt episode the sub-micrometric-to-intermodal ratio was significantly lower (one order of magnitude) than in the rest of the campaign. It is noteworthy that during the period 3-6 February three sub-episodes were identified thanks to significant differences in measured aerosol properties. Indeed, the intermodal-to-coarse ratio was about 10 until the late afternoon of February 3$^{\text{rd}}$, reached 20 in the evening of February 4$^{\text{th}}$ and increased again from late morning in February 5$^{\text{th}}$ to the end of the same day. It is noteworthy that these sub-events can also be detected by a more detailed analysis of $SSCAAE$, which exhibits a first small peak contemporary to the period with intermodal-to-coarse ratio of 10, and in two longer periods is characterised by values higher than 1 interrupted by a minimum on February 5$^{\text{th}}$ corresponding to low SSA values and an increasing contribution by sub-micrometric particles.

A focus on chemical composition can be seen in Figure 3.2, that represents temporal patterns of Na, Mg, Cl, V, Ni and S concentrations measured by PIXE analysis on $PM_{2.5}$ streaker samples.

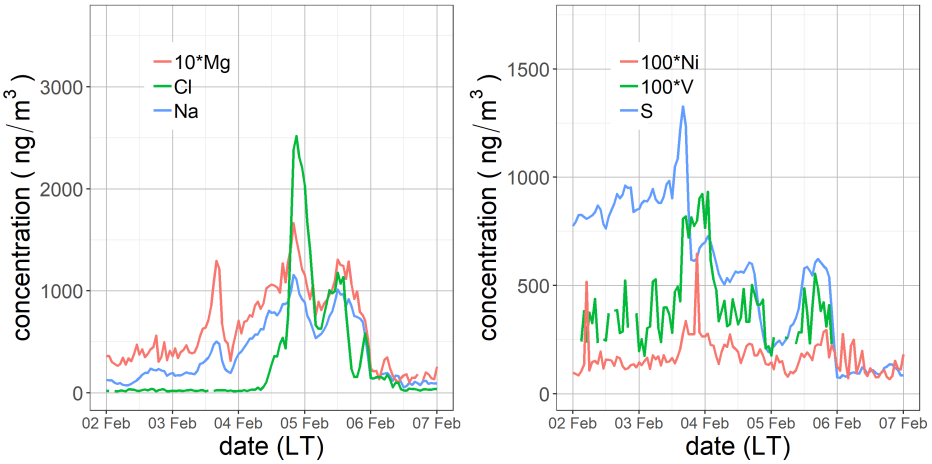

Figure 3.2: Concentrations of Na, Mg, Cl, V, Ni, and S in $PM_{2.5}$ during the CARE campaign [113].

The sea salt advection episode observed was characterised by a simultaneous increase in Na, Cl, and Mg concentrations (see Figure 3.2), reaching 1158, 2518, and 362 ng/m^3, respectively, whereas during the rest of the campaign their average values were 92, 38, and 33 ng/m^3. Sea salt aerosol fresh emissions are typically identified

through diagnostic ratios for bulk sea water [8], e.g. Cl/Na (1.8) and Mg/Na (0.12) (e.g. [153]). It has to be noted that sea salt Cl in aerosol particles can be depleted due to heterogeneous reactions with other compounds occurring in the atmosphere [8], whereas Mg and Na are not involved in these processes; as a consequence, the Cl-to-Na ratio measured in sea salt aerosol can be lower than the one calculated based on bulk sea water composition, while Mg-to-Na ratio is maintained. As Na and Mg can be originated by multiple sources (e.g. sea salt, crustal material, industrial processes), when using the above mentioned diagnostic ratio only the contribution to the concentration of these elements due to sea salt should be taken into account. In this work, the elemental concentration was assessed by PIXE, therefore the concentration of sea salt Na (ssNa) was calculated following Diapouli et al. [154]. During the first episode, the ssNa-to-Na ratio was on average 0.95±0.04, therefore the total Na concentration was used to calculate diagnostic ratios, to avoid further uncertainties related to assumptions in the ssNa calculation. In the first sub-episode (February 3rd) Mg-to-Na ratio was fairly indicative for sea salt aerosol (0.16±0.08) while Cl-to-Na ratio was much lower (0.06±0.02) than the one expected for fresh sea salt. The diagnostic ratios were thus suggesting that aged sea salt particles impacted on the sampling site and that Cl was likely depleted by atmospheric processing during the plume transport [8]. Indeed, on February 3rd (afternoon) peaks in V, Ni, and S concentrations - well known tracers for ship emissions [155] - were also registered (see Figure 3.2 - right). These chemical fingerprints confirmed that this first sub-event corresponded to a plume of aged and polluted marine aerosol at the sampling site.

An increase in $SSCAAE$ and peaks in Cl, Na, and Mg concentrations characterised the second sub-event (February 4th). The Cl/Na and Mg/Na ratios were 1.79±0.75 and 0.14±0.01, respectively, i.e. comparable to diagnostic ratios identifying fresh sea salt. In this episode no significant contribution from anthropogenic components (e.g. V, Ni, EC) was observed, thus indicating the advection of clean marine aerosol at the sampling site.

On February 5th, a third $SSCAAE$ peak was registered and the aerosol characteristics were similar to the previous period but for smaller Cl/Na ratio (0.88±0.38) and concentrations of S, V, and Ni, thus indicating the aging of the sea salt aerosol reaching the CARE site. The assignment of the observed properties to a marine aerosol advection is supported also by back trajectory analysis (not shown).

In between the second and third peak, a decrease in $SSCAAE$ (Figure 3.1), SSA, and concentrations of typical sea salt components, together with increases in EC and $\sigma_{ap}(\lambda)$, suggested a temporary predominance of local urban emissions, as further confirmed by a corresponding decrease in wind speed.

The $SSCAAE$ peak (Figure 3.1) registered between February 24th and 25th highlighted

the second event, when low $SAE(450, 635)$ (below 0.5) and high $AAE(450, 635)$ (above 1.5) were also observed. In addition, a different response was given by $dAAE(450, 635, 880)$ and $dAAE(450, 525, 635)$, which were characterised by high and low values, respectively, thus pointing at the smaller absorption spectral curvature at longer wavelengths compared to the shorter ones. In the literature, SAE with values of about or below zero have often been reported as an indication of desert dust detected at the studied site (e.g. [156, 134, 136, 147, 148, 157, 75, 138]). Indeed, SAE is linked to particle size and desert aerosol is generally characterised by a size distribution with a contribution of larger particles greater than in typical urban background PM. These air masses advection events have usually been associated with AAE significantly larger than one (in the range 1.2-3.5 as reported e.g. in [149, 158, 134, 135, 136, 157, 138]), in contrast to sea salt (exhibiting similar SAE but lower AAE). Moreover, it has been shown (e.g. [149, 134]) that a non-negligible SSA wavelength dependence, and more specifically negative $SSAAE$ values, can be attributed to the predominance of large particles, usually associated with desert dust.

All these considerations, together with the combined temporal patterns of different optical properties (see Figure 3.1), led to the attribution of the observed features described above to an episode of desert dust transported to the CARE sampling site and reaching the ground between February 24^{th} and 25^{th}. For further confirmation of this attribution, size distributions and chemical compositions were also investigated. The intermodal/coarse ratio was about 12 during the episode, and a significant reduction in contribution of sub-micrometric particles was observed; indeed, the sub-micrometric-to-intermodal ratio decreased of 1 order of magnitude compared to the rest of the campaign.

In this period, the concentrations of mineral dust elemental tracers (Figure 3.3) also showed a huge increase and some diagnostic elemental ratios confirmed the signature of a Saharan dust advection. During the episode, Si/Al and Fe/Ca ratios were consistent with values found in other studies [159, 160, 161, 162, 117] especially for dust coming from the central and northern Sahara regions, even though these works are not based on $PM_{2.5}$ samples but on larger size fractions.

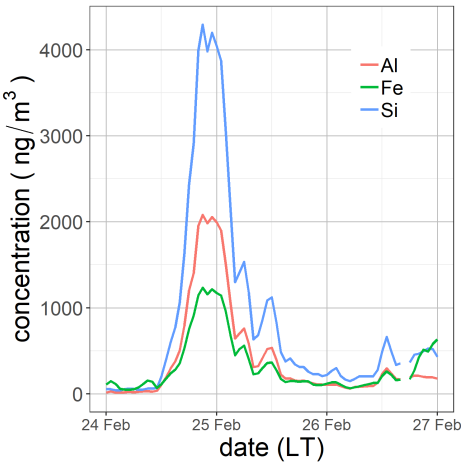

Figure 3.3: Concentrations of Al, Si, and Fe in $PM_{2.5}$ during the Saharan dust episode [113].

In addition, a back-trajectory analysis evidenced that the air mass reaching the CARE site during the night between February 24^{th} and 25^{th} had passed over the Sahara Desert at ground level on February 22^{nd} and then reached Rome after crossing the Mediterranean at higher altitudes.
Another feature shown by $SSCAAE$ was a narrow afternoon peak on February 26^{th} (Figure 3.1), when smoke was seen by researchers working at the CARE site. Indeed, around 13:00 (LT) a large amount of smoke was noticed at Caracalla Stadium and at 18:00 (LT) smoke was smelled at Terme di Caracalla, both places being near the CARE sampling site.
As shown in Figure 3.1, during this event $SAE(450, 635)$ was about 1 and the highest value of $AAE(450, 635)$ was registered. These parameters indicated the presence of small particles with an absorption wavelength dependence stronger than the one of BC, likely due to the presence of Brown Carbon (BrC). A confirmation of the dominant contribution of small particles (expected to be emitted by combustion processes) during the episode was given by the number concentration in each size fraction: a peak in sub-micrometric/intermodal ratio was registered, lasting a couple of hours (between 16:00 and 18:00 LT). Correspondingly, peaks in the biomass burning tracer BBOA was evident, as represented in Figure 3.4. Therefore, the observed patterns were attributed to a short-time biomass burning event. Opposite, the increase in BBOA concentration observed in the late evening is consistent with those registered during other days of atmospheric stability and ascribed to biomass burning for domestic heating (see later).

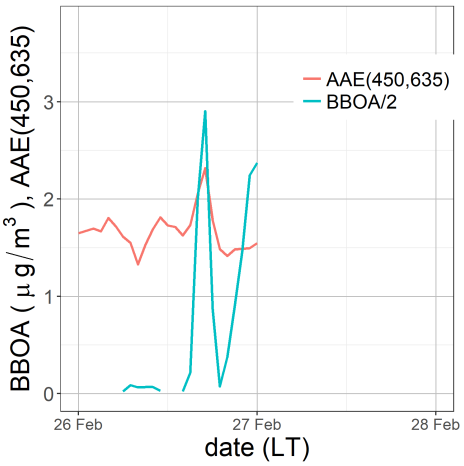

Figure 3.4: Temporal patterns of $AAE(450, 635)$ and of BBOA concentration during the biomass burning event of February 26$^{\text{th}}$, 2017 [113].

The central part of the CARE campaign (from February 7$^{\text{th}}$ to 23$^{\text{rd}}$) was characterised by atmospheric stability, with low wind speeds and clear sky. During this period, high $\sigma_{ap}(635)$ values (>50 Mm^{-1}) were recorded, especially in the evening. Increased concentration of EC and HOA, typically associated to traffic emissions, were detected as well.

In this period, low $SSA(635)$ values (very often below 0.8), $SSCAAE(450, 635) < 0.65$ and mean $SAE(450, 635)$ and $AAE(450, 635)$ of 1.32±0.23 and 1.56±0.24, respectively were also observed. These aerosol characteristics were thus considered as representative of a separate case study characterised by a mixture of local emissions from traffic rush hours and biomass burning used for domestic heating. Indeed, the SAE and AAE values registered indicated a dominance of small particles with a quite strong absorption wavelength dependence, as the one caused by BrC. The central period of the campaign showed low wind speeds (average±standard deviation: 0.75±0.48 m/s), confirming that observed features were due to the contribution of local aerosol sources. Exploiting multi-wavelength high-time resolved aerosol optical properties, an attempt was made to separate hours dominated by traffic and biomass burning contribution in the central part of the campaign, making use of the well-known Aethalometer model [151]. The two sources considered in the model (FF and BB) should have the highest contributions at 880 nm and 450 nm (i.e. the longest and the shortest wavelengths used in this study) due to the different absorption spectral dependence exhibited by FF and BB. Therefore, $\sigma_{ap}(880)(FF)$ and $\sigma_{ap}(450)(BB)$ were considered as the more representative parameters for periods dominated by traffic and biomass burning emissions, respectively (see sub-section 3.1.1). To confirm that these parameters could describe the predominance of fresh traffic emissions or biomass burning aerosol (mainly from domestic heating), their temporal patterns were analysed together with those of HOA

and BBOA concentrations during working days (when traffic signature is more evident). Indeed, these two organic aerosol components are representative of vehicular traffic and biomass burning emissions, respectively. Figure 3.5 reports the diurnal cycles of $\sigma_{ap}(880)(FF)$ and HOA (left panel) and of $\sigma_{ap}(450)(BB)$ and BBOA (right panel).

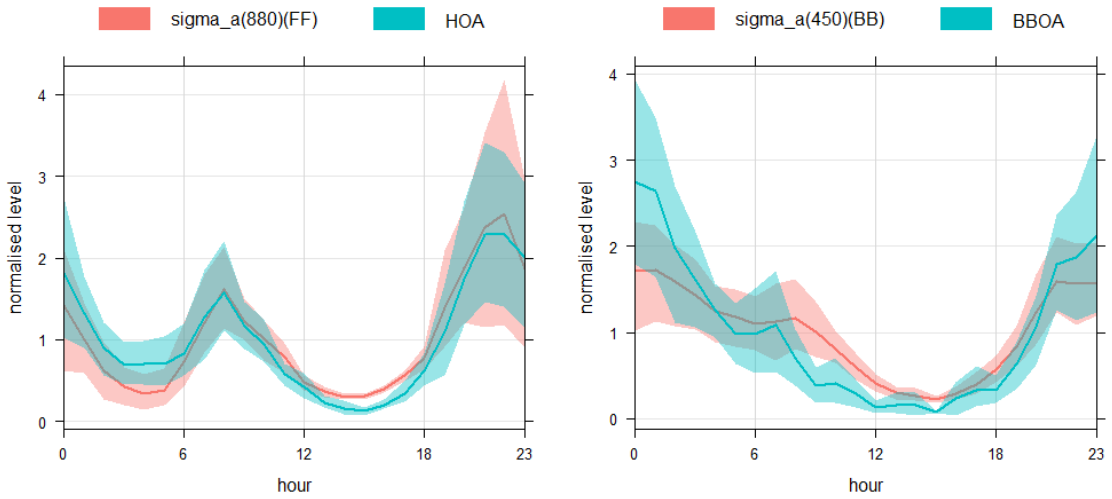

Figure 3.5: Diurnal variation (normalised, in local time) of $\sigma_{ap}(880)(FF)$ and HOA concentration (left panel) and of $\sigma_{ap}(450)(BB)$ and BBOA concentration (right panel). Absorption coefficients were averaged over 1 hour to match OA time resolution. Only data in the central part of the campaign (February 7-23) are considered [113].

It can be observed that the two apportioned absorption coefficients showed a pattern similar to those of the source-apportioned OAs, thus confirming that the Aethalometer model was able to separate the contribution of the two major aerosol sources impacting on absorption properties. This is also consistent with findings in Costabile et al. [119] who combined the Positive Matrix Factorization (PMF) analysis performed on ACSM OA data and the Principal Component Analysis (PCA) on the PNSD to apportion aerosol sources.

In addition, size distributions were used to calculate the total number of Ultrafine Particles (UFP – i.e. particles with aerodynamic diameter smaller than 100 nm) and those in the fraction between 100 nm and 1 μm. Figure 3.6 shows diurnal cycles of particle number in the UFP and 0.1-1 μm size fractions during working days: it can be observed that, as expected, UFPs peak during traffic rush hours, confirming that the dominant contribution during these hours was given by very small, fresh particles from vehicular emissions. In addition, particles in the 0.1-1 μm size fraction showed similar peaks but remained higher during the night, probably due to the effect of emissions

from domestic heating combined with longer residence times of such aerosols [163]. Similar daily patterns were shown by Costabile et al. [119] for PCA scores representing vehicular UFPs and BB fine particles.

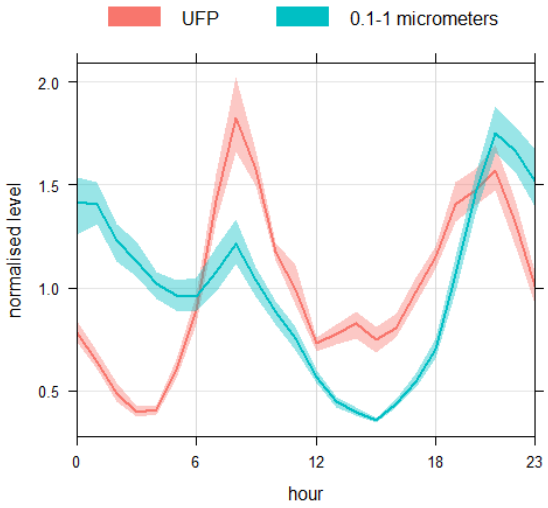

Figure 3.6: Diurnal variation (normalised, in local time) of particle number concentration for UFP and partcles in the 0.1-1 μm size fraction. Original data have a time resolution of 5 minutes. Only data in the central part of the campaign (February 7-23) are considered [113].

Graphical aerosol classification schemes

As shown in the previous paragraph, joining different aerosol intensive optical properties is mandatory to correctly identify separate episodes. Here, some aerosol classification schemes based on the combination of aerosol properties are proposed as graphical tools that can be useful to quickly distinguish specific events out of a complex dataset by combining various parameters together.

Ranges of intensive optical properties allowing to better discriminate among aerosol types identified during the CARE campaign were derived based on the comprehensive analyses previously reported.

Table 3.2 shows the ranges of the optical parameters used to classify each aerosol type; it is worth noting that all the reported conditions should be met for a robust identification.

It is noteworthy that even though there are some limitations because of possible site-specific features, the methodology here proposed could be useful to discriminate in near-real-time between pollution vs. natural sources-driven high PM events in environmental monitoring networks. Indeed, the current legislation (UNI EN 14907/2005) allows to eliminate exceedances of daily PM_{10} threshold due to natural events.

Table 3.2: Ranges of optical parameters useful to classify aerosol types. σ_{ap} is given in Mm^{-1}

Aerosol type	$SSCAAE$ $(450, 635)$	SAE $(450, 635)$	AAE $(450, 635)$	$dAAE$ $(450, 635, 880)$	$dAAE$ $(450, 525, 635)$	SSA (635)	σ_{ap} (450) (BB)	σ_{ap} (880) (FF)
Dust	>0.6	<0.4	>1.5	>1.6	<0.2	>0.8		
Sea	>0.6	<0.4	<1.5	<1.7	<0.2	>0.8		
Polluted marine	0.6-0.9	0.3-0.8	<1.5	1.0-1.5	-1.0-0.0	>0.9		
BB event (fire)	>0.8	>0.7	>1.8	>2.0	>0			
Traffic	<0.2					<0.85		>8
BB	<0.65						>20	

Together, the "polluted marine" and the "clean sea salt" (sea) advections occurred in 7.9% of the cases (i.e. whole CARE dataset); "dust" data covered the 2.7% of the cases; "fire" data were 0.3% of the cases; "traffic" and "BB" data represented the 20.6% and the 17.2% of the cases, respectively.

It has to be noted that episode-discriminating ranges for optical parameters identified here are in principle wavelength-dependent, thus they are expected to be different if other wavelengths are employed for the calculation of intensive optical properties. Moreover, they may differ depending on the location and season, due to the mixing of specific aerosol types with local emissions, that could affect measured properties. Therefore, for an application in monitoring networks, it is strongly suggested to perform a preliminary characterisation to check/identify the most suitable ranges of optical variables. In addition, graphical frameworks presented in the following can serve as guides to identify possible episodes simply observing where data are located in each plot.

Table 3.3 reports ranges of AAE, SAE, and SSA that were used in previous studies to classify aerosol types. Indeed, AAE and SAE were the most commonly employed parameters, usually combined to assess aerosol origin. In some works, information about SSA was added to help the distinction.

Table 3.3 shows that AAE and SAE values used in this work are generally in agreement with literature values; differences may be due to the wavelengths used in the calculation of intensive optical properties, as well as to the fact that columnar or in-situ properties are employed.

After identification and selection of the events, data were represented in some graphi-

Table 3.3: Literature AAE, SAE and SSA values used to classify aerosol types.

Reference	**Columnar /in-situ properties**	**Wavelengths (nm)**	**Aerosol type**	*AAE*	*SAE*	*SSA*
Bahadur et al. [164]	Columnar (AERONET)	440,675	Dust	>1.5	<0.5	
			Biomass Burning	0.5-2	1-2	
			Urban fossil	<1.5	0.5-2	
Cazorla et al. [132]	Columnar (AERONET)	440,675	Dust	>1.5	<1	
			Coated large particles	<1	<1.5	
			OC dominated	>1.5	>1.5	
			EC dominated	<1	>1.5	
Cappa et al. [137]	in-situ	532,600 (AAE)	Dust	>2	<0.2	
			Large particle/low absorption mix	<1	<1	
		450,550 (SAE)	Strong BrC	>2	>1.5	
			BC dominated	1.0-1.5	>1	
Costabile et al. [136]	in-situ	467,660 SSA at 530	Dust	>2	<0.5	>0.85
			Marine	>2	<0.5	>0.95
			BC dominated	<1.5	>2	<0.8
			Brown carbon	>2.5	0.5-2	>0.9
Schmeisser et al. [139]	in-situ	450,700	Biomass burning	<2	1-3	<0.85
			Dust	>1.5	<1	
			Polluted marine	0.9-1.4	0.7-1.7	
			Remote marine	0.5-1.5	<1	
Romano et al. [138]	in-situ	470,660	Continental polluted	1-1.5	>1.4	
			Dust	>2	<-0.2	
			Marine	<1.2	<0	
Rupakheti et al. [133]	Columnar (AERONET)	440,870 EAE instead of SAE SSA at 675	Dust	1.0-3.0	0.0-0.4	0.88-0.96
			Biomass Burning	1.1-2.3	0.8-1.7	0.82-0.91
			Urban/Industrial	0.6-1.3	0.8-1.6	0.89-0.96

cal schemes. The time resolution of represented data is 5 minutes. In Figures 3.7 and 3.8, the left panel represents data classified as a particular aerosol type according to the method described above, whereas the right panel shows the rest of the data (not classified). Data points belonging to each of the identified episodes are distinguished using different symbols.

AAE vs. SAE plot was originally developed in literature for data retrieved from the AERONET network [129] and then refined by Cazorla et al. [132]. Other authors (e.g. [137, 138]) applied the same methodology to in-situ, ground-based data. The graphical classification scheme in Figure 3.7 is the AAE vs SAE plot, colour-coded by $SSA(635)$ following Costabile et al. [136].

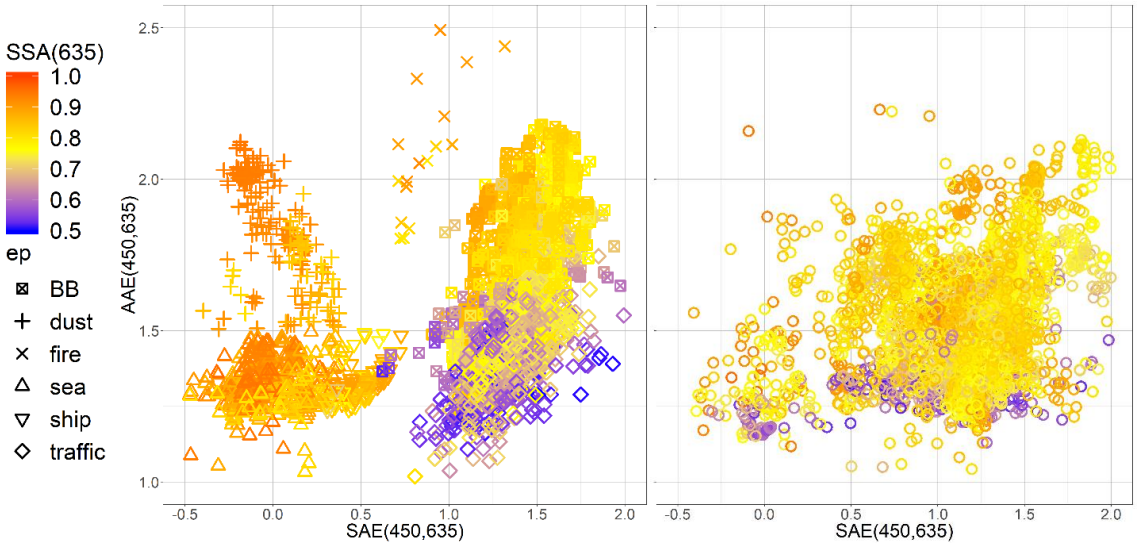

Figure 3.7: AAE vs SAE plot colour-coded by $SSA(635)$ of data classified in an episode (left) and of all the remaining – i.e. non classified – data (right). Different symbols represent data of identified aerosol types. BB stands for biomass burning. Note that "ship" stands for the polluted marine event and "fire" for the short biomass burning event. [113].

As expected by the analysis of temporal patterns of intensive optical properties and by their combination, when representing episodes in a plane, the corresponding data points are placed in different areas. It can be noted that "polluted marine", "sea", "dust" and "fire" (i.e. the short biomass burning event on February 26$^{\text{th}}$) data are basically not mixed with non-classified data in the respective plot areas, as emerges also from Figure 3.7 (right panel), where some zones of the graph are not covered by points. Indeed, points classified as "polluted marine" or "sea" are the majority of data in the area (SAE<0.8; AAE<1.5); they were considered together since they are mixed in the graphical scheme. "Traffic" and "BB" points, although not completely overlapped, are also mixed with each other, reflecting the mixture of local sources contributing to atmospheric aerosol during the central part of the experiment.

In general, the AAE vs SAE plot with the help of the third coordinate (SSA) appears to visually discriminate among episodes, even though no ideal SAE, AAE, and SSA ranges were found to correctly classify the polluted marine advection (dominated by ship emissions) without the combined use of $SSCAAE$ and $dAAE$, that allowed to distinguish this aerosol sub-type.

Therefore, a detailed analysis of temporal patterns of different intensive optical properties (first of all of $SSCAAE$, which is the parameter singling out episodes) gives a more complete set of information which can be used to distinguish all the particular events that may have occurred during a campaign. Moreover, for more complex

mixtures of aerosol from different sources (when atmospheric stability occurs), the additional information from high-time resolved extensive optical properties is necessary to separate the dominant contribution.
The second graphical framework proposed (Figure 3.8) is a SSCAAE vs dAAE plot, colour-coded by $SSA(635)$. It is not a common scheme to distinguish episodes and aerosol types; however, due to the importance of the two examined parameters in events identification, a combination of them into a plot that may allow a visual distinction of specific aerosol features was attempted.

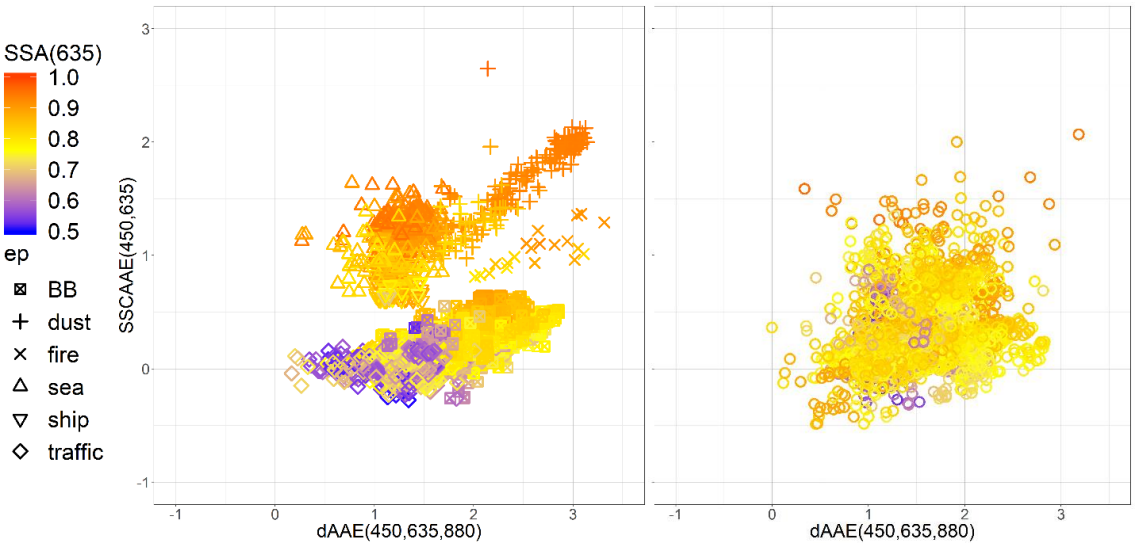

Figure 3.8: SSCAAE vs dAAE plot colour-coded by $SSA(635)$ of data classified in an episode (left) and all the remaining – i.e. non classified – data (right). Different symbols represent data of identified episodes. BB stands for biomass burning. Note that "ship" stands for the polluted marine event and "fire" for the short biomass burning event [113].

Figure 3.8 confirms the potential of $SSCAAE$ as a key parameter for episodes identification. Indeed, except for aerosol mixtures, all the other aerosol types are characterised by $SSCAAE(450, 635)$>0.5. Moreover, the combination with $dAAE$ $(450, 635, 880)$ helps in distinguishing events, since this parameter responds to non-uniform absorption spectral dependences, that can be different for episodes with similar $SSCAAE$ values. For instance, this is the case of "sea" and "fire" aerosol types, characterised respectively by mean $SSCAAE(450, 635)$ equal to 1.16±0.18 and 1.05±0.17 and mean $dAAE(450, 635, 880)$ of 1.25±0.21 and 2.65±0.39, respectively.
As already evident in the AAE vs SAE plot, also in this case episodes are placed in different regions of the plane, and some areas are not well covered by data points when considering only non-classified data (Figure 3.8 – right). In addition, in this graphical framework some aerosol types (in particular "dust", and to a less extent "fire") show

an almost linear relationship between $SSCAAE$ and $dAAE$. Finally, local-sources dominated periods are characterised by an almost λ-independent co-albedo and by an absorption spectral curvature increasing as the contribution of biomass burning emissions increases compared to the one from vehicular traffic.
The SSCAAE vs dAAE plot and AAE vs SAE plot are useful to provide a first hint about episodes and aerosol typologies. Nevertheless, separate 2D plots areas do not correspond uniquely to different aerosol types, and especially local sources dominated aerosol mixtures are not distinguishable from not classified data, since areas where the two populations are located in the plots overlap. In these more complex situations, it is the separate study of temporal patterns of all the intensive optical parameters ($SSCAAE$, SAE, AAE, and $dAAE$) that can provide further information to distinguish aerosol with different origins.

3.1.3 Multi-wavelength aerosol absorption coefficient measured by PP_UniMI

Aerosol absorption coefficient σ_{ap} was measured by PP_UniMI on $PM_{2.5}$ streaker samples, collected with 1-h time resolution on polycarbonate filters. As already mentioned in sub-section 2.2.3, a specific procedure developed by Bernardoni et al. [46] had to be used in this case due to the very small thickness of the membrane filter matrix. Moreover, standard 47-mm diameter quartz-fibre filters were analysed to obtain daily PM_{10} aerosol absorption properties. Multi-wavelength σ_{ap} measured on samples collected in the frame of the CARE experiment are reported in Figures 3.9 and 3.10. Uncertainties on $\sigma_{ap}(\lambda)$ values are 12%.

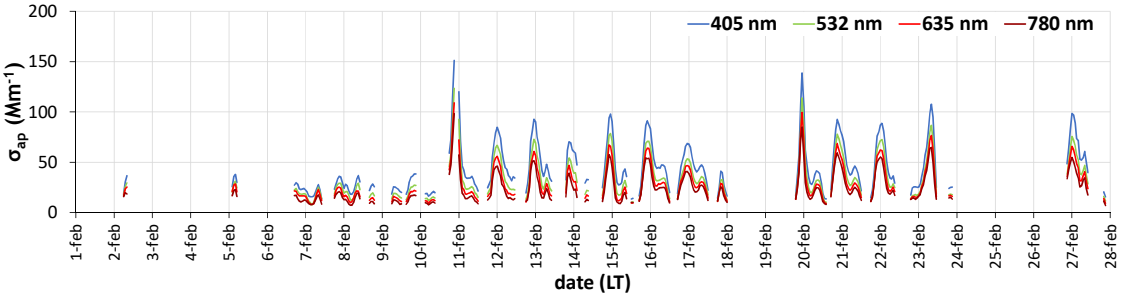

Figure 3.9: $\sigma_{ap}(\lambda)$ measured by PP_UniMI on $PM_{2.5}$ streaker samples collected in the CARE experiment.

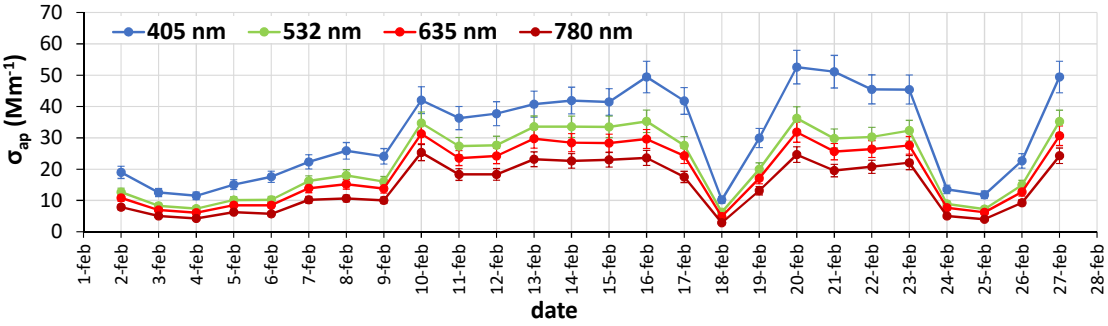

Figure 3.10: $\sigma_{ap}(\lambda)$ measured by PP_UniMI on PM_{10} filter samples collected in the CARE experiment.

It is noteworthy that having parallel measurements of multi-wavelength σ_{ap} collected at different time resolution could be of particular interest in view of applications of multi-time source apportionment models exploiting information about aerosol absorption, such as the one recently developed by the UniMI Environmental Physics research group [165]. Indeed, the use of optical properties in source apportionment models and the exploitation of data with different time resolution can reinforce results of the models themselves, leading to more robust sources identification.
Similarly to what done in the inter-comparison exercise described in sub-section 2.2.2, σ_{ap} measured by PP_UniMI for the CARE experiment was compared to the properly time-averaged one measured by the co-located MAAP at 637 nm; due to the very similar wavelengths, no corrections were made to report the two variables to the same λ. Note that streaker samples analysed with PP_UniMI are $PM_{2.5}$ samples, whereas PM_{10} was sampled on both filters and MAAP filter tape; nevertheless, since absorbing aerosol (mainly BC) is typically composed of small particles (often sub-micrometric), this discrepancy was not expected to cause significant differences in the measured aerosol absorption properties. Moreover, while streaker samplers collect $PM_{2.5}$ samples on a membrane, both 24-h filters and the MAAP tape are made of a fibrous matrix (quartz and glass fibres, respectively).
Figures 3.11 and 3.12 show scatter-plots of $\sigma_{ap}(635)$ retrieved with PP_UniMI on streaker and filter samples, respectively, versus $\sigma_{ap}(637)$ measured by MAAP, respectively averaged over 1 hour and 24 hours. Linear regression analyses were performed considering uncertainties associated to both x and y variables.
It is noteworthy that $\sigma_{ap}(635)$ measured on streaker samples is well correlated to the one by MAAP, although being always lower; this is likely an effect of sampling artefacts on optical measurements, as pointed out by Vecchi et al. [45]. Indeed, artefacts due to organics adsorbed on the filter fibres cause an enhancement of absorption coefficient (estimated as high as 40%). This hypothesis is confirmed by the better agreement between σ_{ap} measured on daily samples and the 24-h average of MAAP data (see Figure

3.12).

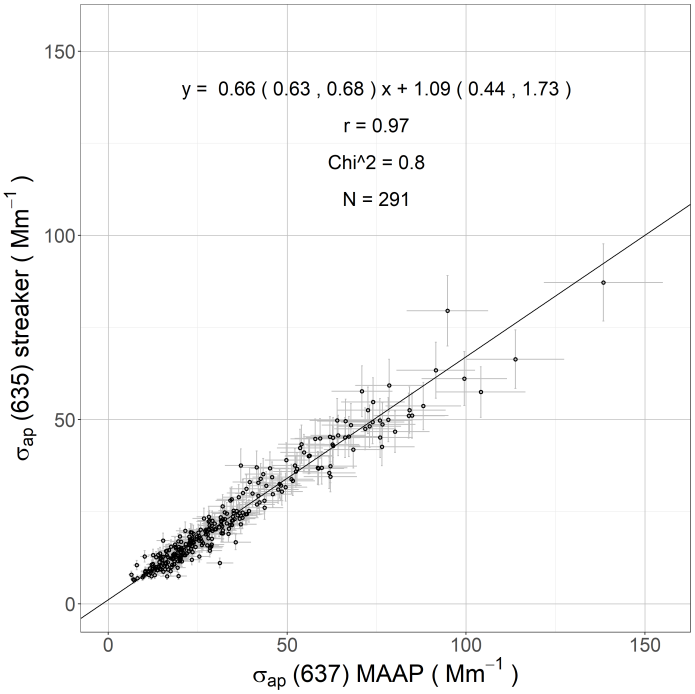

Figure 3.11: Comparison of aerosol absorption coefficient measured by PP_UniMI on streaker samples and by MAAP. Ranges in brackets are 95% confidence intervals of the Deming regression parameters.

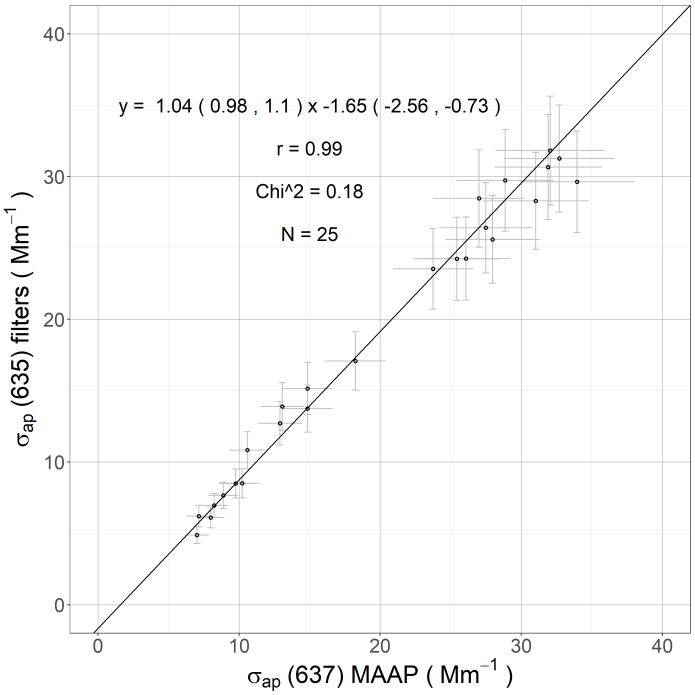

Figure 3.12: Comparison of aerosol absorption coefficient measured by PP_UniMI on filter samples and by MAAP. Ranges in brackets are 95% confidence intervals of the regression parameters.

So far, the effect of sampling artefacts on aerosol absorption coefficient has been investigated only at $\lambda = 635\,\text{nm}$ [45, 46]; since during the CARE campaign a 7-λ Aethalometer AE33 measured multi-wavelength σ_{ap}, it was possible to extend the evaluation at more wavelengths. In particular, as explained in sub-section 3.1.1, the wavelengths 450, 525, 635, and 880 nm were considered for aerosol optical properties measured in the experiment. Details about the data elaborations are described in sub-sections 3.1.1 and 3.1.2. Figure 3.13 represents the comparison of $\sigma_{ap}(\lambda)$ measured by PP_UniMI on streaker samples and the same quantity obtained by hourly averaged AE33 data (note that AE33 outputs were corrected *a posteriori* for scattering enhancement - see sub-section 3.1.1); all data were reported to the chosen wavelengths using for each instrument hourly AAEs calculated as power-law fits of original data (4-λ: 405, 532, 635, 780 nm for PP_UniMI; 7-λ: 370, 470, 520, 590, 660, 880, 950 nm for AE33).

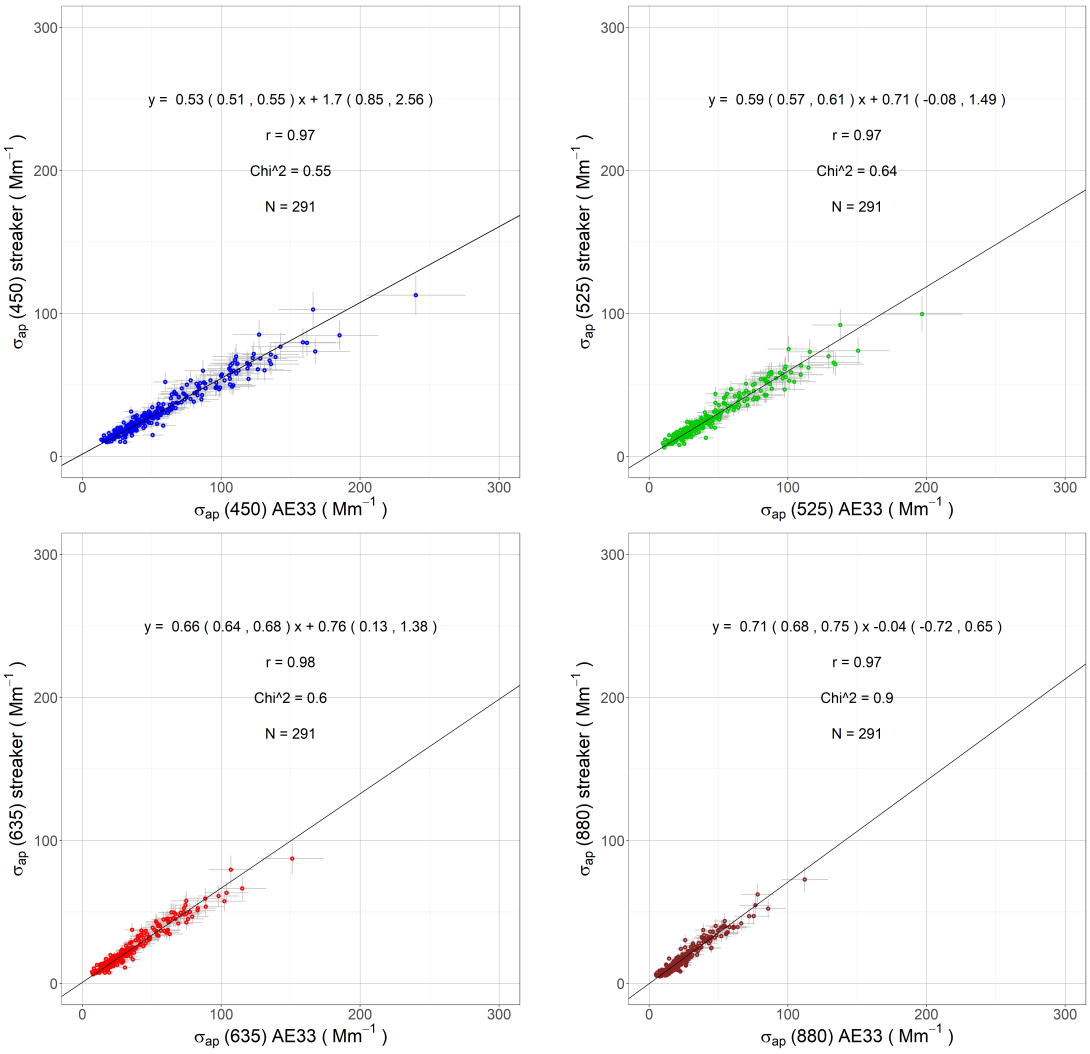

Figure 3.13: Scatter-plots of $\sigma_{ap}(\lambda)$ measured with PP_UniMI on hourly streaker samples versus $\sigma_{ap}(\lambda)$ obtained by hourly averaged AE33 data. Ranges in brackets are 95% confidence intervals of the Deming regression parameters.

At all wavelengths, data are well correlated (r>0.95), and the effect of sampling artefacts appears to vary with the wavelength. The observed behaviour could be caused by the combination of a different optical response to artefacts at different λs and the approach chosen to correct AE33 data for scattering enhancement (see sub-sections 2.2.4 and 3.1.2), that was considered λ-independent.

3.2 Indoor and outdoor multi-wavelength aerosol absorption coefficients in Terni

As described in sub-section 2.2.3, a campaign was performed in Terni (Central Italy) by the University La Sapienza (Rome - Italy) and the Institute for Atmospheric Pollution of the National Research Council (IIA-CNR) using low-cost smart samplers to assess the impact of different anthropogenic aerosol sources on the air quality of this city. Indeed, Terni is located in a basin that prevents an efficient atmospheric dispersion causing the accumulation of pollutants; moreover, several local emission sources (power plant - waste incinerator, rail network, biomass burning for heating and industrial processes, vehicular traffic, steel plant) are present. A map of Terni with the location of major anthropogenic aerosol sources and of sampling sites chosen for the campaign is reported in Figure 3.14.

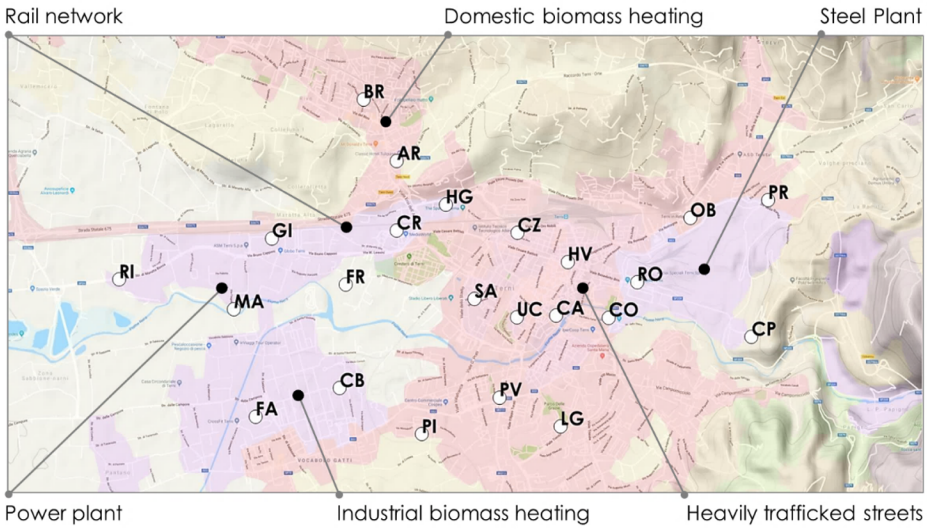

Figure 3.14: Map of the Terni city; the location of major anthropogenic aerosol sources and of sampling sites are reported.

A total of 32 sites were chosen to analyse the effects of the main anthropogenic sources in Terni. 7 out of 32 samplers were located in indoor environments to evaluate the penetration coefficients of pollutants in different situations; moreover, in one location (PV - a sky-scraper in the city centre) three samplers were installed at different

altitudes (0, 15, 50 m agl, named PV0, PV1, PV2, respectively) in order to obtain the vertical profile of measured species and optical properties.

PM_{10} samples were collected on 37-mm PTFE filters on which several quantitative analyses were performed: X-Ray Fluorescence (XRF) for elements, Ion Chromatography (IC) for water-soluble ions, and Inductively Coupled Plasma-Mass Spectrometry (ICP-MS) for soluble and insoluble elemental fractions. Moreover, the four ARPA monitoring stations located in Terni measured in parallel the concentrations of elemental and organic carbon (EC and OC, respectively).

Smart samplers collected aerosol at a low flow rate (0.5 l/min), and filters were typically changed once a month. Two 1-month periods (one in summertime and one in wintertime) were selected to perform additional measurements with PP_UniMI (see sub-section 2.2.1), to estimate the impact and possible signature of different sources on aerosol absorption properties. The two periods with optical measurements (10 June - 17 July 2017; 20 January - 19 February 2018) will be hereafter referred to as "summer" and "winter" campaigns, respectively. It is noteworthy that, as far as the author knows, optical parameters are not reported in the literature for indoor environments.

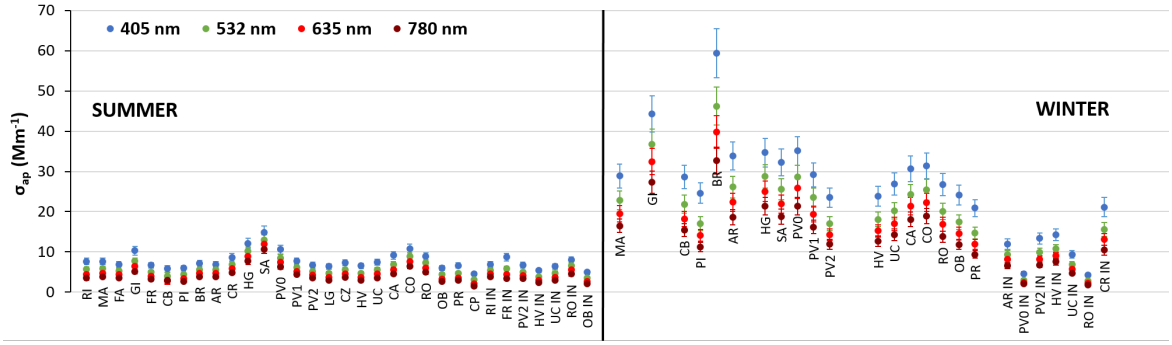

Figure 3.15: Aerosol absorption coefficient measured with PP_UniMI on Terni samples.

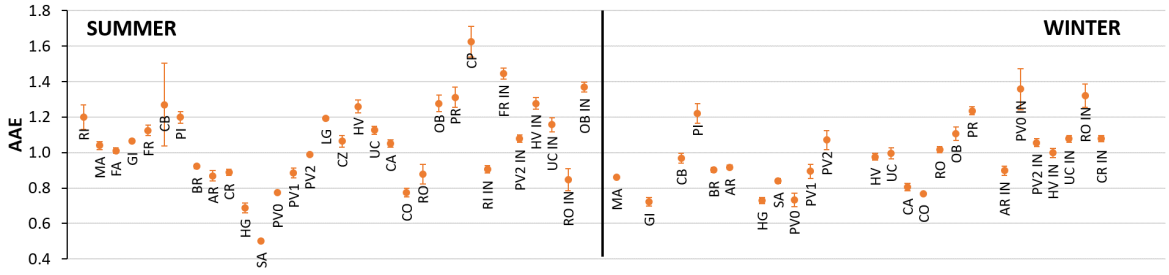

Figure 3.16: Absorption Ångström Exponent calculated as a power-law fit of $\sigma_{ap}(\lambda)$ measured with PP_UniMI on Terni samples.

Figures 3.15 and 3.16 represent respectively the multi-wavelength $\sigma_{ap}(\lambda)$ and the *AAE* as measured by PP_UniMI on Terni samples and retrieved as a power-law fit on

all λs from these measurements, respectively. Data labels indicate the sampling sites (see Figure 3.14) and "IN" stands for indoor sample.
In general, it can be noted that the aerosol absorption coefficient was higher during the winter campaign than during the summer campaign at all wavelengths, as can be expected due to the lower mixing layer height that reduces atmospheric dilution and due to some additional local sources (e.g. biomass burning for domestic heating) that are active only during the cold season. Table 3.4 reports statistics of $\sigma_{ap}(\lambda)$ and AAE for the two Terni campaigns.

Table 3.4: Statistics of $\sigma_{ap}(\lambda)$ (in Mm^{-1}) and AAE retrieved for the summer and winter Terni campaigns form measurements performed with PP_UniMI.

Statistic	SUMMER					WINTER				
	σ_{ap} (405)	σ_{ap} (532)	σ_{ap} (635)	σ_{ap} (780)	AAE	σ_{ap} (405)	σ_{ap} (532)	σ_{ap} (635)	σ_{ap} (780)	AAE
average	7.7	5.9	4.9	4.0	1.1	25.5	19.7	16.9	14.0	1.0
std. dev.	2.1	2.0	2.0	1.8	0.2	12.1	10.0	8.8	7.4	0.2
min	4.6	3.1	2.2	1.5	0.5	4.2	2.8	2.3	1.8	0.7
10^{th} perc.	5.8	4.0	3.0	2.6	0.8	10.4	7.9	6.7	5.5	0.8
90^{th} perc.	10.6	8.5	7.4	6.2	1.3	34.9	28.7	25.5	21.4	1.2
max	14.9	12.9	11.9	10.7	1.6	59.3	46.2	39.9	32.7	1.4

In addition to the seasonal variability, differences between outdoor and indoor samples can be observed: for instance, average ($\pm$ standard deviation) $\sigma_{ap}(635)$ measured on outdoor and indoor samples were $\sigma_{ap,OUT}$=5.1$\pm$2.1 Mm^{-1} and $\sigma_{ap,IN}$=4.0$\pm$1.0 Mm^{-1} during the summer campaign, and $\sigma_{ap,OUT}$=20.7$\pm$7.0 Mm^{-1} and $\sigma_{ap,IN}$=7.0$\pm$3.8 Mm^{-1} during the winter one. Outdoor and indoor values were similar for the summer data, reflecting the habit of keeping windows open in this season hence allowing air from outside to enter indoor environments, whereas during wintertime measured aerosol absorption coefficients were higher outdoor than indoor, due to the lower penetration. Larger $\sigma_{ap}(635)$ were observed at sites characterised by the influence of vehicular and railway traffic, and steel plant millwork processes; moreover, for the winter campaign, also a site (BR) impacted by domestic biomass burning heating showed high values of the aerosol absorption coefficient.
As far as the absorption wavelength dependence is concerned, AAE values were similar in both campaigns, and slightly higher values were registered indoor. Indeed, for the summer campaign AAE_{OUT}=1.0$\pm$0.2 and AAE_{IN}=1.2$\pm$0.2 and during wintertime AAE_{OUT}=0.9$\pm$0.2 and AAE_{IN}=1.1$\pm$0.2. Sites exhibiting a stronger absorption wave-

length dependence were those impacted by emissions from combustion processes in the steel plant and cigarette smoke (indoor sites); the latter observation is particularly interesting, since it highlighted a possible optical signature of cigarette smoke. Indeed, the same sites (especially FR and PV0) showed the highest indoor-to-outdoor ratio for AAE.
Finally, the vertical profile of $\sigma_{ap}(\lambda)$ and AAE at the PV site is reported in Figure 3.17.

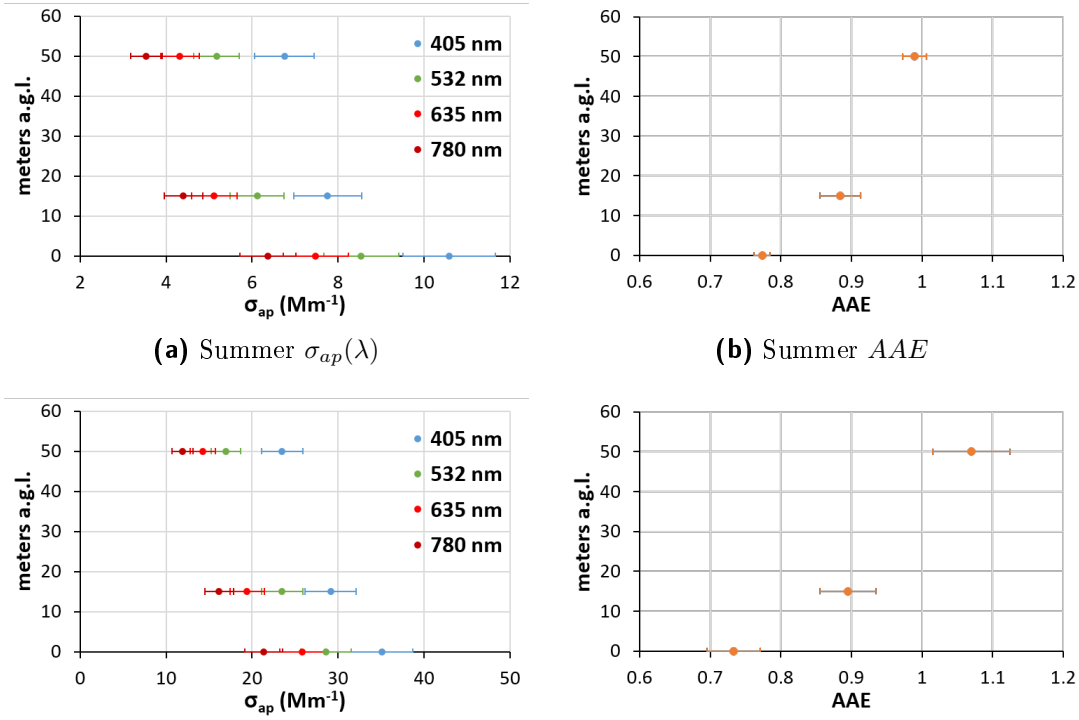

(a) Summer $\sigma_{ap}(\lambda)$ **(b)** Summer AAE

(c) Winter $\sigma_{ap}(\lambda)$ **(d)** Winter AAE

Figure 3.17: Vertical profiles of $\sigma_{ap}(\lambda)$ (a, c) and of AAE (b, d) during the summer and winter Terni campaigns.

It can be observed that $\sigma_{ap}(\lambda)$ decreased at higher altitudes for both campaigns, likely due to the dispersion of local emissions, that are mainly from vehicular traffic at the PV0 site (ground level). Conversely, AAE increased with the height: this feature is probably caused by the impact of combustion processes in the Terni steel plant. Indeed, the PV2 site (50 m a.g.l.) is located downwind the steel plant (considering the average wind direction in the city) and at an altitude that can be easily reached by emissions from the chimneys of the steel plant; moreover, as observed above, combustion processes in the steel plant were responsible for high AAE values compared to those from vehicular traffic.

3.2.1 Aerosol absorption coefficient due to cigarette smoke: preliminary results

Results of measurements performed on samples collected in Terni gave rise to an additional sampling campaign carried out by the research groups of University La Sapienza and the IIA-CNR during which outdoor and indoor samples were collected in parallel in order to evaluate the effect of cigarette smoke on aerosol optical properties and chemical composition. The campaign took place between February 25$^{\text{th}}$ and March 15$^{\text{th}}$ 2019 in Rome (Italy). PM_{10} samples were collected simultaneously inside a cigarette smoker's office and at a standard monitoring station about 100 m far from it. The samples were divided in three time slots during each week of the campaign: "Weekend" (Friday 19:00 LT - Monday 09:00 LT), "Mon-Tue" (Monday 09:00 LT - Wednesday 09:00 LT), and "Wed-Fri" (Wednesday 09:00 LT - Friday 19:00 LT). Sampled filters were then analysed as for multi-wavelength aerosol absorption coefficient $\sigma_{ap}(\lambda)$ with PP_UniMI, and elemental and chemical analyses are in progress. In the following, preliminary results obtained by optical measurements are shown.

Figures 3.18 and 3.19 show $\sigma_{ap}(\lambda)$ measured with PP_UniMI and AAE obtained as a power-law fit, respectively; data are framed according to the different time slots.

It can be observed that both $\sigma_{ap}(\lambda)$ (at all wavelengths) and AAE were generally higher for indoor samples than for corresponding outdoor ones. If only working days (time slots "Mon-Tue" and "Wed-Fri" are considered, average ($\pm$ standard deviation) $\sigma_{ap}(635)$ was $9.9 \pm 2.0\,\text{Mm}^{-1}$ and $7.7 \pm 3.7\,\text{Mm}^{-1}$ for indoor and outdoor samples, respectively, and $AAE(\text{indoor}) = 2.0 \pm 0.6$ while $AAE(\text{outdoor}) = 1.2 \pm 0.2$. When weekends are considered, an opposite behaviour is observed in $\sigma_{ap}(635)$ ($5.7 \pm 2.9\,\text{Mm}^{-1}$ and $7.4 \pm 4.7\,\text{Mm}^{-1}$ for indoor and outdoor samples, respectively), even though the variability is larger compared to working days, while indoor and outdoor AAEs were similar ($AAE(\text{indoor}) = 1.3 \pm 0.4$ and $AAE(\text{outdoor}) = 1.2 \pm 0.3$). This reflects the small indoor-outdoor exchanges during wintertime; indeed, air from outside, largely influenced by traffic emissions (that significantly contribute to σ_{ap} but typically show $AAE \approx 1$), does not penetrate, and indoor air impacted by cigarette smoke does not exit.

These preliminary results show that cigarette smoke may have a characteristic optical signature, since AAE values as high as 2.9 were registered for indoor samples: this may be caused by the incomplete combustion in cigarettes, producing compounds such as BrC that generally show AAE significantly larger than 1. Further investigations coupling optical properties and chemical composition could give more information about features of aerosol produced by this particular source.

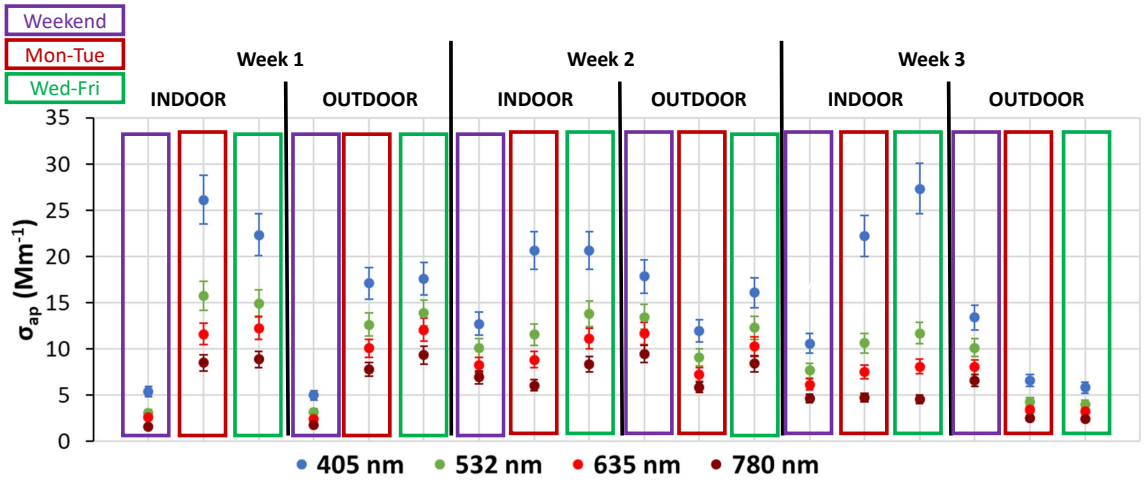

Figure 3.18: Multi-wavelength aerosol absorption coefficient measured on filters of the cigarette smoke campaign.

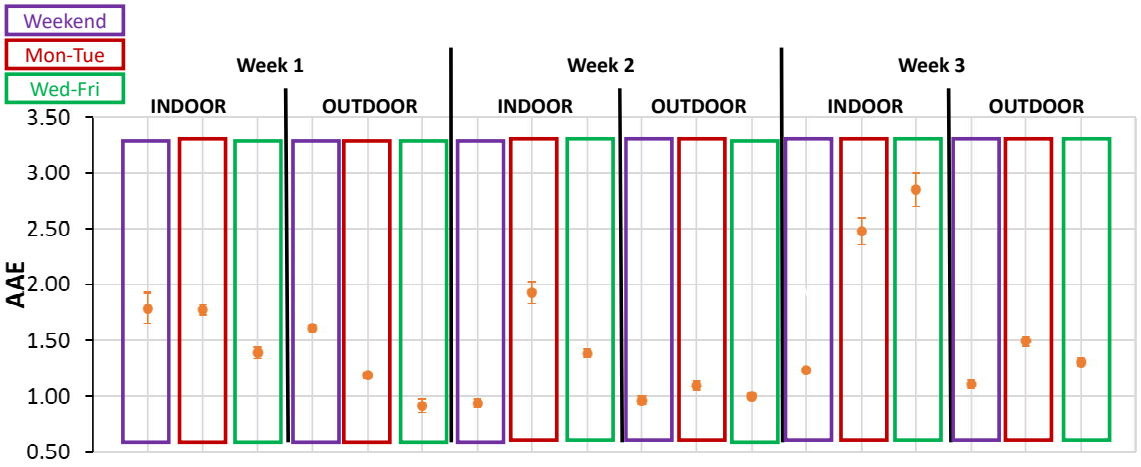

Figure 3.19: Absorption Ångström Exponent calculated as a power-law fit of $\sigma_{ap}(\lambda)$ measured on filters of the cigarette smoke campaign.

3.3 Measurements of multi-λ absorption coefficient in the frame of the ACTRIS-2 – Mt. Cimone and Po Valley Field Campaign

As mentioned in sub-section 2.2.3, an international field campaign was realised in July 2017 in the framework of the European project ACTRIS-2. The study had two main objectives: (1) the definition of parameters and artefacts affecting the (optical) measurement techniques of Black Carbon (BC); (2) understanding source areas and dynamics of aerosol transport and aging. To reach these aims, several instruments

measuring aerosol absorption coefficient were deployed at three sites in Central Italy with different characteristics: Bologna (BO - urban background), Mt. Cimone (MTC - mountain remote background), and San Pietro Capofiume (SPC - rural background). In addition to on-line techniques, filter sampling was carried out for off-line optical and chemical analyses.

It is noteworthy that samples from the rural and remote sites of SPC and MTC, respectively, often exhibited absorbance (ABS) values near or lower than PP_UniMI LODs; indeed, only 27% of MTC filters resulted in $ABS(635) > 0.1$. Some results from optical measurements performed on filters sampled during the ACTRIS-2 Mt. Cimone and Po Valley Field Campaign are reported in Table 3.5. It is noteworthy that PP_UniMI was also effective in providing robust results also in case of lightly loaded samples as those collected at remote sites thus opening the way to further applications in future research works.

Table 3.5: Statistics for $\sigma_{ap}(635)$ and AAE values obtained from PP_UniMI measurements of filters collected during the ACTRIS-2 Mt. Cimone and Po Valley Field Campaign at Bologna (BO), San Pietro Capofiume (SPC) and Mt. Cimone (MTC) sites.

Site	$\sigma_{ap}(635)$ (Mm^{-1})		AAE	
	average±std. dev.	min-max	average±std. dev.	min-max
BO	5.6±2.1	2.5-11.9	1.1±0.1	0.8-1.3
SPC	4.2±1.8	1.0-8.3	1.1±0.2	0.9-1.5
MTC	0.9±0.2	0.6-1.2	0.9±0.2	0.7-1.2

In Table 3.5, statistics of $\sigma_{ap}(635)$ and its wavelength dependence (represented by AAE) are reported. Note that for MTC data only samples with $ABS(635) > 0.1$ were considered; this caused an overestimation of $\sigma_{ap}(635)$: values reported are hence to be considered as upper limits. AAE was calculated fitting the 4-λ σ_{ap} values obtained with PP_UniMI with a power law.

Results show a gradient in aerosol absorption coefficient, that decreased going from urban to rural locations and in particular to remote sites. A different behaviour was exhibited by AAE, being very similar among the three sites and showing low values (about 1) typical of BC, thus excluding a significant contribution of Brown Carbon, that is typically more relevant in wintertime due to domestic heating.

3.4 Application of the tailored IMPROVE algorithm

In the last decades, the concern for PM fine fractions increased due to their adverse effects on human health, climate and visibility. Indeed, air pollution impacts on solar light extinction, a parameter which can be related to visibility as routinely done by the IMPROVE network in the U.S. (see Section 2.3).

From the scientific and legislative point of view, studies on particulate matter moved from PM_{10} (EU Air Quality Directive EC/30/1999 and EN12341) to $PM_{2.5}$ (EN14907/2005) and, more recently, the scientific community has addressed its interest to submicron sized (PM_1, aerodynamic diameter lower than 1 μm) and ultrafine particles (UFP, aerodynamic diameter lower than 0.1 μm) as smaller sized aerosols can penetrate deeply into the respiratory system causing adverse health effects (e.g. [166, 167]; see also Section 1.1).

At different locations in Europe, PM_1 can be a significant fraction of $PM_{2.5}$ and PM_{10} (e.g. [168, 169, 170]) and previous works demonstrated that it can be considered a good indicator of emissions from anthropogenic sources (e.g. [171, 172]). Few previous studies on PM_1 physical-chemical properties and sources were performed in Milan ([173, 174, 92, 170]). Notwithstanding, none of them investigated daytime and nighttime PM_1 concentrations, composition, sources, and their impact on light extinction as done in this work for wintertime, i.e. the period of the year when Milan typically experiences very high PM concentrations. In heavily polluted areas such as the Po Valley and the large urban areas located there, air quality management policy and risk assessment need a comprehensive knowledge of the detrimental pollutants as well as of major emission sources.

The straightforward way to assess light extinction is based on direct measurements of aerosol optical properties (i.e. extinction, scattering, and absorption coefficients) using dedicated instrumentation. Unfortunately, these instruments (e.g. Nephelometers, absorption/extinction analysers - see Section 2.1) are not always available in monitoring networks or during measurement campaigns thus preventing any information about visibility and aerosol optical properties. In this frame, the alternative and simple approach proposed by the IMPROVE algorithm, giving estimates of the extinction coefficient through atmospheric chemical components assessment, can be very useful although less accurate (as described in Section 2.3). Indeed, in many monitoring networks and measurement campaigns PM samples are routinely collected to be chemically analysed for retrieving aerosol composition; these data can be fruitfully used also to estimate light extinction as done in the IMPROVE network.

In this work, to assess atmospheric light extinction and visibility impairment a tailored site-specific approach (Section 2.3) is used to better exploit the characteristics of the well-known IMPROVE algorithm.

At the state of the art, there are still very few papers (e.g. [175, 84, 176, 177, 178]) estimating the impact of the different emission sources on light extinction (i.e. reconstructed light extinction, σ_{ext}) as done in this work, although this is one of the environmental challenges at many polluted areas. In addition, this was the first time that the contribution to light extinction due to different aerosol components and sources was assessed at a European pollution hot spot site. These results are extensively reported in Vecchi et al. [111].

3.4.1 Measurement campaign

PM_1 aerosol measurements were performed in Milan which is the largest town in the Po Valley (Italy); the latter is a reknown pollution hot-spot in Europe characterised by low atmospheric dispersion especially during wintertime.
The sampling campaign was carried out at the urban background monitoring station of the Department of Physics, at about 10 meters a.g.l. in the University campus (details in Vecchi et al. [97]) during wintertime 2012 (from 9^{th} January to 18^{th} March).
PM_1 samples were collected in parallel on quartz-fibre (Pall, 2500 QAO-UP, 47 mm diameter) and PTFE (Whatman, PM2.5 Membranes, 46.2 mm with ring) filters using low-volume sequential samplers (Charlie HV coupled to Sentinel PM by TCR Tecora srl-Italy; and LVS 3 by Derenda-Germany) operated at a 2.3 m^3/h flow-rate. Nighttime and daytime 9-hour samplings (07-16; 19-04 LT) were performed obtaining 120 samples in total. The reduced time slots were needed to avoid filter clogging and were chosen in order to sample during major emission periods (e.g. traffic rush hours and wood burning hours for domestic heating in the evening).
Before and after the sampling, filters were conditioned for 48 hours in an air-controlled weighing room (T = 20±1 °C and R.H. = 50 ±5%). PM_1 mass concentration was determined by weighing them using an analytical microbalance (precision 1 μg, details in Vecchi et al. [92]).
Samples were chemically characterised as follows: elements by Energy Dispersive X-Ray Fluorescence analysis on PTFE filters (ED-XRF, details in Vecchi et al. [92]), ions by Ionic Chromatography on a portion of each quartz-fibre filter (IC, details in Piazzalunga et al. [179]), elemental and organic carbon (EC and OC) by thermal optical transmittance analysis on a punch taken from each quartz-fibre filter (TOT using NIOSH-like thermal protocol, details in Piazzalunga et al. [179]), anhydrosugars by high performance anion-exchange chromatography coupled with pulsed amperometric detection on a portion of each quartz-fibre filter (HPAEC-PAD, details in Piazzalunga et al. [180]).
Moreover, to retrieve the light-absorption coefficient at 635 nm the samples were analysed using the polar photometer PP_UniMI (see sub-section 2.2.1 - details in Vecchi

et al. [45] and Bernardoni et al. [46]).
Meteorological parameters (temperature, pressure, relative humidity, wind speed and direction, global solar radiation, precipitation) recorded by the meteorological station located at the same urban background monitoring station, and gaseous pollutants data retrieved by the nearby station of the Environmental Agency of Lombardy (`www.arpalombardia.it`) were used for data interpretation.

3.4.2 Receptor modelling for source apportionment

Positive Matrix Factorization (PMF) was the receptor model used in this study. Here, only a brief description of the method is given, since it is not the focus of this PhD work; more details can be found in the references. PMF is a least squares program for solving multi-linear problems. Specifically, it solves models where the data values are fitted by sums of products of unknown factor elements [181]. For bilinear problems it takes the form X = G·F + E, where X is the known n by m matrix of the m measured chemical species in n samples; G is an n by p matrix of factor contributions to the samples; F is a p by m matrix of species concentrations in the factor profile; p is the factors number. G and F are factor matrices to be determined and they are constrained to non-negative values only. E is defined as a residual matrix i.e. the difference between the measurements X and the model Y = G·F as a function of G and F.
The dataset was analysed with EPA-PMF 5.0 [182] and comprised only strong variables, defined according to the signal-to-noise criterion reported in Paatero [183] and all data were pre-treated according to Polissar et al. [184] as for uncertainties, values below detection limits and missing data. The dataset was composed by 17 variables (mass, Si, K, Ca, Ti, Mn, Fe, Cu, Zn, Br, Pb, OC, EC, NO_3^-, SO_4^{2-}, NH_4^+, Levoglucosan) and 109 data entries.
The optimal solution for the base case was given by 7 factors; factor labelling was accomplished according to percentage of species and the chemical profile (represented as dots and bars, respectively, in Figure 3.20). Percentages higher than 30% were considered as significant and the factor-to-source assignments were nitrate, sulphate, wood burning, industry, traffic, fine dust and a Pb-rich source. The latter source in Milan was associated to industrial/waste incinerator emissions; it was also identified at other sites, e.g. in Southern Italy [185] and in Switzerland [186] and was related to an industrial origin.

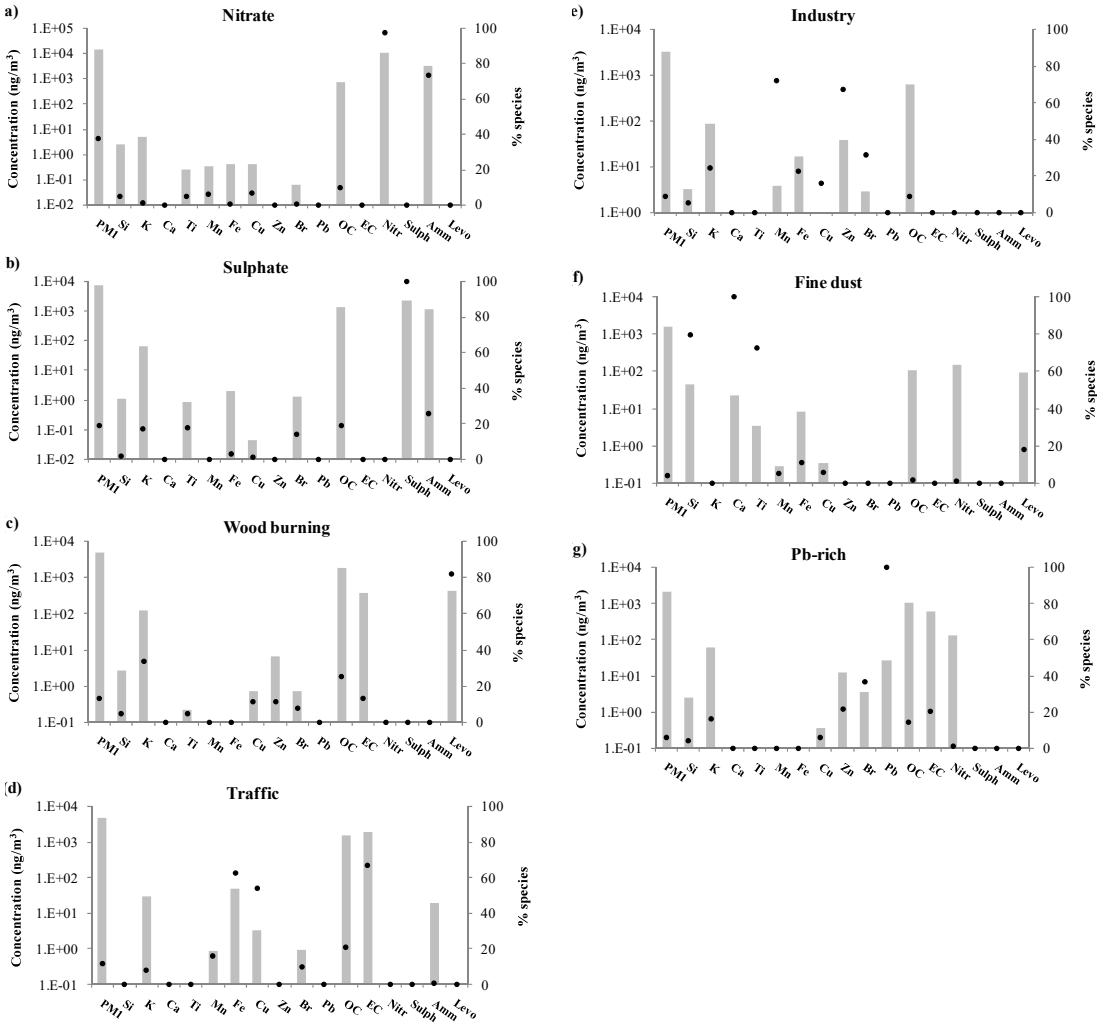

Figure 3.20: Factors chemical profiles (bars) and percentage of species (dots) in each factor of the 7-factor solution obtained by EPA-PMF with Fpeak=+0.5. Note that Nitr stands for Nitrate, Sulph for Sulphate, Amm for Ammonium, and Levo for Levoglucosan. [111]

Factor 1 (nitrate) was the most relevant contributor accounting for 37% of PM_1 mass; all the other factors explained less than 20% of PM_1 mass. Factor 2 (sulphate) was responsible on average of 19% of measured mass, while factors 3 (wood burning) and 4 (traffic) explained respectively 13% and 12% of PM_1 mass, respectively. Factor 5 (industry) accounted for 9% of measured mass concentration. Finally, factors 6 (fine dust) and 7 (Pb-rich) explained on average 4% and 5% of PM_1 mass, respectively. Average, nighttime and daytime source apportionment are reported in Figure 3.21.

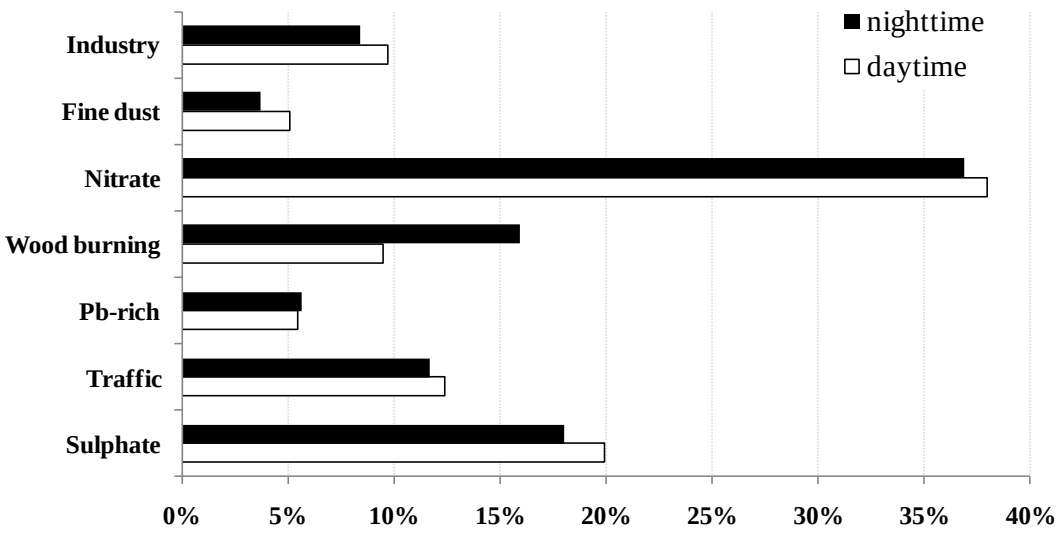

Figure 3.21: Source apportionment (in %) given for nighttime and daytime [111].

Except for wood burning, which was consistently higher (on average +7%) during the night, source contributions did not show significant differences between daytime and nighttime, although on daytime all other resolved factors (i.e. sulphate, fine dust, and industry) showed slightly higher percentages (differences higher than 1%).
More details about the source apportionment performed on PM_1 samples can be found in Vecchi et al. [111].

3.4.3 Recontructed extinction coefficient of PM_1 and source apportionment of light extinction

In this work, a multi-linear regression (MLR) analysis was applied to the sources resolved by PMF (i.e. elements of the G matrix) and σ_{ep} (i.e. considering only the contribution to σ_{ext} due to aerosol components thus excluding Rayleigh scattering and NO_2 contributions - see Equation 2.27) to assess source contributions to σ_{ep} [84, 176]. Light extiction was reconstructed from atmospheric compositional and meteorological data according to the tailored algorithm described in Section 2.3 and in Valentini et al. [91].
On average (Table 3.6), among the aerosol components the major contributor to total light extinction coefficient (σ_{ext}) was ammonium nitrate (34.1%), followed by organic matter (27.0%), light absorption components (σ_{ap}) consisting primarily of BC (10.5%), ammonium sulphate (8.5%), and coarse mass (7.3%). As expected, in PM_1 fine soil was almost a negligible contributor (0.4%) to σ_{ext}. The gases extinction term - due to clear-air Rayleigh scattering and NO_2 absorption - overall explained 12.1% of σ_{ext}. From light extinction coefficient σ_{ext} the visual range (VR, in km - see Table 3.6) was also estimated using the Koschmieder equation (1.37) $VR = \frac{3.912}{\sigma_{ext}} \cdot 1000$.

Table 3.6: Statistics of light extinction coefficients σ_{ext} (in Mm^{-1}) and visual range (VR, in km). Total number of samples: 110 (adapted from Vecchi et al. [111]). Notation for components is the same as in Section 2.3.

σ_{ext} (Mm^{-1})	Total	AMSUL	AMNIT	OM	σ_{ap}	FS	CM	RS	NO_2	VR (km)
mean	287.2	24.1	108.9	77.1	28.2	0.8	21.1	12.0	14.9	18.8
std. dev.	158.1	20.0	88.1	44.9	15.2	0.5	11.6	0.2	4.4	13.2
min	45.0	1.6	1.4	12.4	5.5	0.3	1.9	11.5	4.9	4.3
max	919.9	111.5	510.9	214.4	75.1	4.8	64.8	12.5	26.1	86.9
average percentage		**8.5%**	**34.1%**	**27.0%**	**10.5%**	**0.4%**	**7.3%**	**5.7%**	**6.4%**	

The literature data on chemical extinction at urban sites refer mainly to Chinese towns. On average, σ_{ext} in Milan was much lower (i.e. about a factor 3-5) than values reported in Chinese cities (see for example [84, 87, 88]); on the contrary, comparable σ_{ext} wintertime values were found at a Chinese suburban site [89]. OM – which was one component accounting for a significant part of the light extinction in Milan - was reported as the largest contributor to σ_{ext} by some authors (e.g. [87, 178, 177] and in those papers ammonium nitrate typically accounted for 20% of σ_{ext}. Cao et al. [84] reported that OM was the second largest contributor when considering data corresponding to a visual range higher than 10 km; this is comparable to what detected for Milan in this work where a VR higher than 10 km was recorded in approximately 80% of the days and where OM represented the second largest contributor to light extinction. Cao et al. [84] in all other cases – corresponding to much lower visual range values – reported that the dominant component was ammonium sulphate, in agreement with what found at other Chinese cities and at non-urban IMPROVE sites [187] where percentages of about 40% and 60%, respectively, were recorded. It is noteworthy that this was never the case in this study where on average this component accounted for less than 9%. Temporal patterns of σ_{ep} showed that the contribution due to organic matter and ammonium nitrate was often comparable but when the highest σ_{ep} occurred ammonium nitrate generally contributed at most. In Milan, the relationship between VR and light extinction due to ammonium nitrate and OM could be well represented by a decreasing power law with squared R higher than 0.85 while the correlation parameter decreased to 0.5 for ammonium sulphate (not shown).
The apportionment of aerosol light extinction is reported in Table 3.7.

Table 3.7: Source apportionment of the extinction coefficient for atmospheric aerosols (σ_{ep}) in Mm^{-1} and %. (adapted from Vecchi et al. [111]).

	Sulphate	Traffic	Pb-rich	Wood burning	Nitrate	Fine dust	Industry	σ_{ep}
				All data				
Mm^{-1}	38.5	37.4	15.3	26.0	87.5	1.7	6.0	210.2
%	18.3	17.8	7.3	12.4	41.6	0.8	2.9	
				Daytime				
Mm^{-1}	39.0	37.3	14.6	19.2	85.7	2.0	6.3	202.7
%	19.3	18.4	7.2	9.5	42.3	1.0	3.1	
				Nighttime				
Mm^{-1}	38.0	37.5	16.0	32.3	89.3	1.5	5.8	217.5
%	17.5	17.2	7.3	14.8	41.1	0.7	2.7	

Results show that considering all samples together, ammonium nitrate contributed at most to σ_{ep} (on average 41.6%) with no significant daytime-nighttime difference and σ_{ep} was accounted for by sulphate, traffic, and wood burning sources as much as 18.3%, 17.8% and 12.4%, respectively. In Milan secondary inorganic aerosols (i.e. sulphate and nitrate) gave a very high contribution (up to 60%) to σ_{ep} which was typically much higher than most of the results reported in literature works for Chinese towns (i.e. [108, 178, 177]). Opposite, traffic contribution to σ_{ep} in Milan is low in comparison to estimates given by some Chinese authors (e.g. [108, 178]) who reported contributions which were twice than those found in this work (although in literature works a large variability exists on these estimates which range from less than 10% up to 40%). Another not negligible contribution was given by wood burning, which resulted comparable to estimates reported in literature works ranging from 4 to 25% (e.g. [176, 177]). Note that all sources used in the MLR but fine dust (accounting for less than 1% of σ_{ep}) were statistically significant, as verified by the t-statistics of the regression parameters.

It is noteworthy that a recent paper by the Environmental Physics research group in Milan [165] has shown that joining chemical and optical variables as input to receptor models can help to identify sources and to gain information on the effect of different sources on various aerosol properties simultaneously; currently, this kind of approach has been not attempted to estimate light extinction. In particular, when σ_{ep} is reconstructed by the IMPROVE methodology, some issues may arise: 1) the assumptions made increase σ_{ep} uncertainties so that the insertion of this variable in a receptor

model can be questionable; 2) chemical variables themselves are used to calculate σ_{ep} and retrieve sources.

Conclusions

Several methodologies investigated in this work were applied to data collected in the frame of several measurement campaigns.
In particular, an original method was developed to distinguish aerosol types combining different high-time resolved optical data, suitably corrected thanks to the knowledge gained about on-line instruments and their correction schemes.
Moreover, the flexibility of PP_UniMI was exploited to measure aerosol samples collected on various kinds of filters during sampling campaigns aiming at different goals, also in collaboration with other research groups.
Finally, the developed tailored approach to the IMPROVE algorithm was successfully applied to a PM_1 dataset and coupled with a source apportionment study to estimate contributions of aerosol sources to light extinction.

Conclusions and perspectives

In this thesis, experimental and modelling approaches were explored and developed to investigate atmospheric aerosol optical properties, that represent one of the major knowledge gaps in aerosol science. Aerosol has effects on Earth energy balance, visibility, air quality and human health. In particular, this thesis was focused on impacts on climate, strictly dependent on optical properties of atmospheric particles and whose estimate is affected by a very large uncertainty, and on visibility, which is a parameter directly perceived by people and related to air quality.

Several open issues in atmospheric science and research were addressed in this work through both advancements in experimental methods, such as the polar photometer developed by the Environmental Physics research group at the University of Milan (PP_UniMI) (also inter-compared with widespread on-line instrumentation), and modelling approaches.
In the following, major questions addresses in this PhD thesis are listed and briefly described.

- In the frame of an inter-comparison experiment carried out in collaboration with the Jülich Forschungszentrum FZJ (Jülich - Germany) and the University of Genoa (Physics Department), a possible bias was pointed out in the output of the MAAP, that is currently considered as the reference filter-based instrument to measure aerosol absorption coefficient σ_{ap}. Indeed, thanks to the flexibility of PP_UniMI, which directly measures the angular distribution of light scattered by a filter sample in the whole scattering plane, a discrepancy was observed between the outputs of PP_UniMI and MAAP when the angular distribution of scattered light is not well reproduced by the analytical functions set by default in the latter instrument (see sub-section 2.2.2). In addition, the inter-comparison showed a good agreement of PP_UniMI with the in-situ "Ext-Sca" method (i.e. retrieved by CAPS PM_{SSA} and Nephelometer data) when small and spherical Cabot soot particles and their mixtures with ammonium sulphate were generated; conversely, σ_{ap} of flaming soot, that typically forms fractal-like aggre-

gates with various sizes depending on the combustion conditions, was lower when retrieved by PP_UniMI compared to the "Ext-Sca" value. It is noteworthy that all filter-based methods were in agreement independently of the aerosol type. Therefore, the possible role of aerosol size distribution and morphology deserves further analyses.

- A hot topic related to biases in measurements by the Aethalometer and linked to a non-proper correction for scattering enhancement (C factor) was faced exploiting both experimental and modelling approaches to retrieve robust C values and to investigate potential wavelength dependence of this correction factor (see sub-section 2.2.4).
  The feasibility of performing PP_UniMI measurements on AE33 sample spots to obtain multi-wavelength C values was tested, highlighting the need of optimisation of the set-up and procedures for this specific purpose; these activities are currently in progress at the Environmental Physics research group in Milan.
  Furthermore, algorithms based on simultaneous MAAP and multi-wavelength aerosol scattering coefficient (σ_{sp}) data were investigated, and a method exploiting the comparison of AE33 attenuation and MAAP absorption data was considered to find out suitable C values.
  Aethalometer spots and parallel absorption and scattering data used in this thesis were collected in the frame of the international collaborative project CARE (Carbonaceous Aerosol in Rome and Environs).

- In close collaboration with the Aerosol Physics ad Environmental Physics group of the University of Vienna, the scattering coefficient of laboratory generated particles was measured with polar Nephelometers and modelled from particle size distribution data in the framework of a laboratory experiment with the aim of investigating the Nephelometer truncation correction (see sub-section 2.2.5). Preliminary results were shown in the thesis, and data analysis is in progress to improve estimates of modelled σ_{sp} and understand the reliability of truncation correction based on scattering wavelength dependence.

- The widespread IMPROVE algorithm, commonly used to estimate light extinction and visibility exploiting atmospheric composition and meteorological parameters, was investigated to highlight possible biases in its application at polluted urban sites, as its fixed coefficients could actually depend on aerosol properties as also recently pointed out in the literature [188]. A tailored approach was developed in this work to compute dry mass extinction efficiencies and water growth functions for typical characteristics of wintertime aerosol in Milan (Italy) (see Section 2.3). A further step in this research item could be the retrieval of

tailored coefficients for different seasons and at sites characterised by different properties (e.g. rural, marine, industry impacted), in order to develop look-up tables of dry mass extinction efficiencies and water growth functions that could be routinely used by air quality monitoring networks to assess light extinction and visibility, which are additional air quality metrics as already proven by the U.S. IMPROVE network.

The methodologies developed in this thesis were applied to datasets collected during several measurement campaigns, also in the frame of international collaborations, as briefly summarised in the following.

- High-time resolved aerosol absorption and scattering coefficients measured in Rome (Italy) with an Aethalometer, a MAAP, and a Nephelometer during the CARE experiment were investigated focusing on their wavelength dependence to extract the maximum information and to find out an original methodology to distinguish aerosol types based on the combination of several intensive optical parameters (see sub-section 3.1.2). Both advection-dominated aerosol typologies and local-sources dominated mixtures were identified, and the classification was confirmed by chemical and size distribution data. A possible perspective for this methodology could be its application to datasets collected at other sites and in different seasons, with the possibility to develop look-up tables of combined ranges of optical properties, which could be employed by monitoring networks to have first hints on the aerosol types and mixtures sampled. Note that the Aethalometer was corrected *a posteriori* using an algorithm previously chosen, to obtain a suitable and relaible C value for this campaign.

- PP_UniMI set-up and operation were optimised for the analyses of several filter types and sizes (see Sections 3.2 and 3.3). In particular, during this thesis indoor aerosol samples, collected during sampling campaigns designed and realised by the University La Sapienza (Rome - Italy) and the Institute for Atmospheric Pollution of the National Research Council (IIA-CNR), were measured for the first time with PP_UniMI; one of the most relevant and promising results obtained was a possible optical absorption signature of cigarette smoke, that gave rise to an additional sampling campaign and that could lead to interesting future research. Moreover, a source apportionment study coupling aerosol composition and optical properties measured in Terni is in progress.

- The tailored approach to light extinction retrieval was applied to a completely characterised dataset of PM_1 samples collected in Milan during wintertime in 2012, and the reconstructed aerosol extinction coefficient σ_{ep} was apportioned among emission sources identified applying a receptor model. Results showed

that nitrate was the major contributor to σ_{ep}, followed by sulphate, traffic, and wood burning emissions (see Section 3.4).

Appendix A

Two-layer radiative transfer model

The main quantities involved in the two-strean radiative transfer model used to retrieve aerosol absorption coefficient σ_{ap} from PP_UniMI measurements are:

- A: absorbance: fraction of incident radiation that is absorbed;
- T: transmittance: fraction of incident radiation that is transmitted in the same direction;
- F: fraction of incident radiation that is scattered in the forward hemisphere;
- B: fraction of the incident radiation that is scattered in the backward hemisphere;
- $P = T + F$: fraction of the incident radiation passing to the forward hemisphere.

For energy conservation law, $T + F + B + A = 1$.
In the following, subscripts p, f, and pf will denote the aerosol-filter layer, the filter layer, and the whole sampled filter system (see sub-section 2.2.1), respectively [37]; superscript (0) will represent the blank filter, while no superscript will indicate the sampled filter. Finally, quantities related to diffuse radiation will be denoted by the superscript $*$, whereas no superscript will be used for collimated incident radiation.

Adding method

In the development of the radiative transfer algorithm applied to aerosol collected on a filter, Hänel [47] considered all the interactions of the radiation with the deposited particles and with the filter matrix, taking into account multiple scattering effects in the aerosol-filter layer and between the two layers: this procedure is called adding method.
Radiative processes in the sampled filter system are reported in Figure A.1.

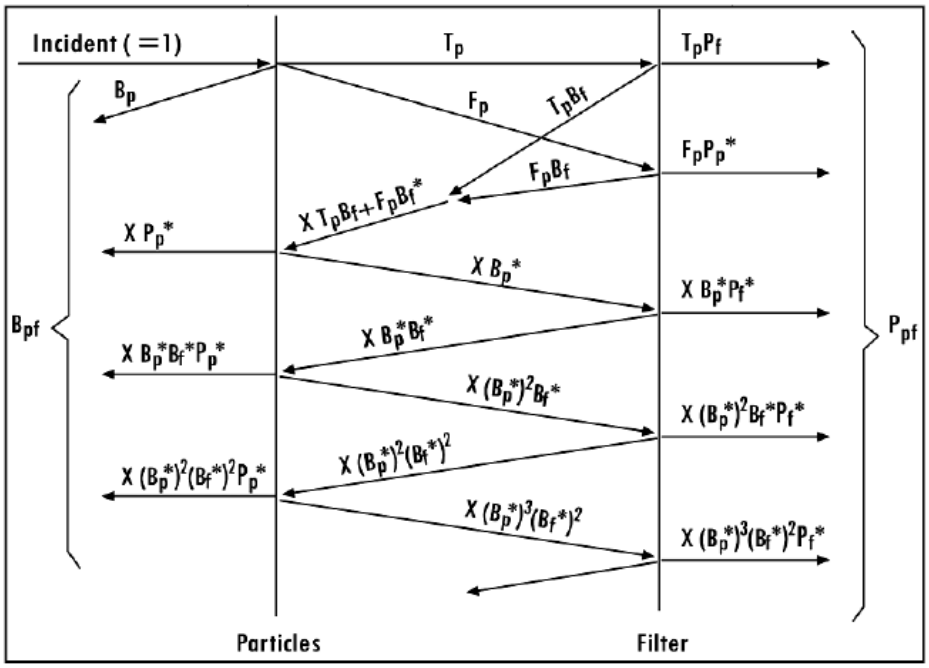

Figure A.1: Scheme of radiative processes in a sampled filter [47].

Collimated incident radiation hits the particles-containing layer perpendicularly and it is subject to absorption, scattering, and transmission; radiation passing through the aerosol-filter layer is strongly scattered due to multiple scattering effects and only a very small fraction the remains collimated. Radiation transmitted through the particles-containing layer hits the filter matrix perpendicularly and interacts with it as no particles were deposited; also the forward scattered radiation impinges on the matrix and it is partly transmitted and partly scattered; the back-scattered fraction hits particles again and interacts a second time. Continuing with this procedure, all the possible interactions are taken into account. The sum of relevant contributions can be expressed as [47]:

- fraction of the incident radiation that is back-scattered by the filter towards the particles:

$$\beta_f^* = \frac{T_p B_f + F_p B_f^*}{1 - B_p^* B_f^*} \tag{A.1}$$

  where the numerator represents the radiation that is back-scattered by the filter after the first passage of the incident radiation through the aerosol-filter layer, and the denominator is the amplification factor for multiple scattering between the two layers $(1/(1 - B_p^* B_f^*) = 1 + B_p^* B_f^* + (B_p^* B_f^*)^2 + ...)$;

- fraction of the incident radiation that is scattered by particles towards the filter:

$$\sigma_p^* = F_p + B_p^* \beta_f^* \tag{A.2}$$

- intensity of the radiation passing through the sampled filter:

$$P_{pf} = P_f T_p + P_f^* \sigma_p^* \tag{A.3}$$

- intensity of the radiation back-scattered by the sampled filter:

$$B_{pf} = B_p + P_P^* \beta_f^* \tag{A.4}$$

In the second member in Equations A.2, A.3, and A.4, the first term represents the interaction with collimated incident radiation and the second one with diffuse incident radiation. Quantities P_f^* and B_f^* can be replaced by corresponding quantities for collimated radiation P_f and B_f, since the difference is less than 10%, as verified by Clarke [189]. The assumptions $P_f^* = P_f$ and $B_f^* = B_f$, together with Equations A.1, A.2, A.3, A.4, allow to retrieve the two balance equations

$$\frac{P_{pf}}{P_f} = \frac{T_p + F_p}{1 - B_p^* B_f^*} \tag{A.5}$$

$$\frac{B_{pf}}{B_f} = P_p^* \cdot \frac{T_p + F_p}{1 - B_p^* B_f^*} + \frac{B_p}{B_f} \tag{A.6}$$

Petzold and Schönlinner [37] implemented the adding method developed by Hänel [47] replacing the quantities P_f and B_f (relative to the filter layer) in the first member of Equations A.5 and A.6 with the corresponding quantities related to the blank filter $P_f^{(0)}$ and $B_f^{(0)}$: the approximation $P_f^{(0)} \cong P_f$ and $B_f^{(0)} \cong B_f$ is justified by the small thickness of the aerosol-filter layer (see Figure 2.2), so that the filter layer is almost as thick as the whole filter itself. Therefore, it is possible to write the balance equations in their final form:

$$\frac{P_{pf}}{P_f^{(0)}} = \frac{T_p + F_p}{1 - B_p^* B_f^*} \tag{A.7}$$

$$\frac{B_{pf}}{B_f^{(0)}} = P_p^* \cdot \frac{T_p + F_p}{1 - B_p^* B_f^*} + \frac{B_p}{B_f} \tag{A.8}$$

The quantities P_{pf}, $P_f^{(0)}$, B_{pf}, $B_f^{(0)}$ can be directly measured by PP_UniMI, while F_p, B_p, P_p^*, B_p^* in the second member are functions of the optical depth $\tau_p = -\ln T_p$, of the single scattering albedo ω_p, and of the particle phase function, according to relationships obtained by the two-stream approximation (see later); B_f depends on the filter type and can be determined based on the blank filter measurement.

Two-stream approximation

In the radiative transfer theory, Hänel made use of a two-stream approximation developed by Coakley and Chýlek [48]: indeed, as explained in the following, although the application was different, analogies in the physical phenomena involved allowed to

employ this model to atmospheric aerosol collected on a filter. Indeed, Coakley and Chýlek developed a two-stream model for the transfer of radiation through an optically thin, plane, and parallel layer of the atmosphere; aiming at assessing the heating caused by the presence of an absorbing and scattering layer (the atmosphere itself) above a reflecting surface (the Earth).

Coakley and Chýlek applied to the atmosphere layer the radiative transfer equation taken from Sagan and Pollack [190] and Sellers [191]

$$\mu \cdot \frac{dI^{(0)}(\tau,\mu)}{d\tau} = I^{(0)}(\tau,\mu) - \frac{1}{2}\int_{-1}^{1} p^{(0)}(\mu,\mu')I^{(0)}(\tau,\mu')\,d\mu' \tag{A.9}$$

(where $\mu = \cos\theta$) with the approximation of a thin atmosphere in the limit of small aerosol optical thickness. They developed 2 two-stream models differing one another for the treatment of incident radiation (seen as an external or internal source). Hänel used the second two-stream model, considering the incident radiation as an internal source, to obtain P_p^* and B_p^* (parameters describing the phenomena generated by a diffuse radiation in a layer). Some analogies were exploited: the thin atmospheric layer with a small optical depth and the underlying reflecting surface introduced by Coakley and Chýlek were replaced by the aerosol and the filter layers, respectively. In this way, the same physical model is reproduced since particles, like air molecules, are placed in a thin layer.

Considering an isotropically scattered radiation, the following quantities describing the interactions of light scattered by the filter with the aerosol layer can be calculated:

$$B_p^* = \frac{b\left(1 - T_p^{2\sqrt{B}}\right)}{\sqrt{B} + a + (\sqrt{B} - a)T_p^{2\sqrt{B}}} \tag{A.10}$$

$$P_p^* = \frac{1}{2\sqrt{B}}\left[(\sqrt{B} - a + B_p^* b)T_p^{-\sqrt{B}} + (\sqrt{B} + a - B_p^* b)T_p^{\sqrt{B}}\right] \tag{A.11}$$

where

- $a = 2\left[1 - \omega_p(1 - \beta_p^*)\right]$
- $b = 2\omega_p\beta_P^*$
- $B = a^2 - b^2$

For a collimated incident radiation, it follows:

$$B_p = \frac{c - \frac{p_1}{1+\sqrt{B}} - \left(c - \frac{p_1}{1-\sqrt{B}}\right)T_p^{2\sqrt{B}} - \frac{2p_1\sqrt{B}}{1-B}T_p^{1+\sqrt{B}}}{\sqrt{B} + a + (\sqrt{B} - a)T_p^{2\sqrt{B}}} \tag{A.12}$$

$$F_p = \frac{1}{2\sqrt{B}}\left[\left(d + B_p b + \frac{p_2}{1+\sqrt{B}}\right)T_p^{-\sqrt{B}} - \left(d + B_p b + \frac{p_2}{1-\sqrt{B}}\right)T_p^{\sqrt{B}}\right] + \frac{p_2}{1-B}T_p \tag{A.13}$$

where

- $c = \omega_p \beta_p$
- $d = \omega_p (1 - \beta_p)$
- $p_1 = c - ac - bd$
- $p_2 = -ad - bc - d$

β_p and β_p^* represent the fractions of radiation back-scattered by the aerosol-filter layer for a collimated and a diffuse incident radiation, respectively; they depend only on the asymmetry parameter g:

$$\beta_p = \frac{1}{2}\left[1 - g - \frac{4}{25}\left(1 - \frac{|1-2g|}{8} - \frac{7}{8}(1-2g)^2\right)\right] \tag{A.14}$$

$$\beta_p^* = \frac{1}{2}\left[1 - \frac{g}{4}(3 + g^{3+2g^2})\right] \tag{A.15}$$

As already mentioned, the g value is usually fixed to be suitable for an average aerosol population (see sub-section 2.2.1). Equations A.14 and A.15 are approximated expressions obtained for a Henvey-Greenstein scattering phase function [47, 192], that well represents Hänel's experimental system.

Bibliography

[1] Fuzzi S., Baltensperger U., Carslaw K., Decesari S., Denier van der Gon H., Facchini M.C., Fowler D., Koren I., Langford B., Lohmann U., Nemitz E., Pandis S., Riipinen I., Rudich Y., Schaap M., Slowik J.G., Spracklen D.V., Vignati E., Wild M., Williams M., Gilardoni S.; Particulate matter, air quality and climate: lessons learned and future needs; Atmospheric Chemistry and Physics 15 (2015) 8217-8299; doi:10.5194/acp-15-8217-2015

[2] Raes F., Van Dingenen R., Vignati E., Wilson J., Putaud J.-P., Seinfeld J.H., Adams P.; Formation and cycling of aerosols in the global troposphere; Atmospheric Environment 34 (2000) 4215-4240

[3] Pöschl U.; Atmospheric Aerosols: Composition, Transformation, Climate and Health Effects; Atmospheric Chemistry 44 (2005) 7520-7540; DOI: 10.1002/anie.200501122

[4] Boucher O.; Atmospheric Aerosols - Properties and Climate Impacts; (2015); ISBN 978-94-017-9648-4

[5] Tomasi C., Fuzzi S., Kokhanovsky A.; Atmospheric Aerosols - Life Cycles and Effects on Air Quality and Climate; (2017) ISBN 978-3-527-33645-6

[6] Friedlander S.K.; Smoke, Dust, and Haze - Fundamentals of Aerosol Dynamics; Second edition (2000); ISBN 978-0-19-512999-1

[7] Ramachandran S.; Atmospheric Aerosols - Characteristics and radiative effects; (2018) ISBN 978-1-4987-5073-8

[8] Seinfeld J.H., Pandis S.; Atmospheric Chemistry and Physics. From Air Pollution to Climate Change (1998); Wiley Interscience; ISBN 0-471-17815-2

[9] Colbeck I., Lazaridis M.; Aerosol Science - Technology and Applications; (2014); ISBN 978-1-119-97792-6

[10] Hinds W.C.; Aerosol Technology; Second edition (2017); ISBN 0-471-19410-7

[11] Calvo A.I., Alves C., Castro A., Pont V., Vicente M., Fraile R.; Research on aerosol sources and chemical composition: Past, current and emerging issues; Atmospheric Research 120-121 (2013) 1-28; http://dx.doi.org/10.1016/j.atmosres.2012.09.021

[12] EPA - United States Environmental Protection Agency; Air Quality Criteria for Particulate Matter - Volume I; (2004)

[13] Whitby K.T.; The physical characteristics of sulphur aerosol; Atmospheric Environment 12 (1978) 135-159

[14] Hofmann W.; Modelling inhaled particle deposition in the human lung - a review; Journal of Aerosol Science 42 (2011) 693-724; https://doi.org/10.1016/j.jaerosci.2011.05.007

[15] Wilson W.E., Chow J.C., Claiborn C., Fusheng W., Engelbrecht J., Watson J.G.; Monitoring of particulate matter outdoors; Chemosphere 49 (2002) 1009-1043

[16] Hamra G.B., Guha N., Cohen A., Laden F., Raaschou-Nielsen O., Samset J.M., Vineis P., Forastiere F., Saldiva P., Yorifuji T., Loomis D.; Outdoor particulate matter exposure and lung cancer: a systematic review and meta-analysis; Environ. Health Perspect. 122 (9) (2014) 906-911; doi: 10.1289/ehp/1408092

[17] Gualtieri M., Øvrevik J., Holme J.A., Perrone M.R., Bolzacchini E., Schwarze P.E., Camatini M.; Differences in cytotoxicity versus pro-inflammatory potency of different PM fractions in human epithelial lung cells; Toxicol. in Vitro 24 (1) (2010) 29-39; https://doi.org/10.1016/j.tiv.2009.09.013

[18] Bohren C.F., Huffman D.R.; Absorption and scattering of light by small particles; Wiley (1983)

[19] Jackson J.D.; Classical Electrodynamics - Third Edition; Wiley (1998) ISBN 0-471-30932-X

[20] Wiscombe W.J, Grams G.W; The backscatter fraction in two-stream approximation; Journal of the Atmospheric Sciences 33 (1976) 2440-2451

[21] Sviridenkov M.A.; Retrieval of asymmetry factor of scattering phase function from scattering and extinction measurements; Presented at the European Aerosol Conference 2015, Milan (italy)

[22] Lack D.A., Cappa C.D.; Impact of brown and clear carbon on light absorption enhancement, single scatter albedo and absorption wavelength dependence of black

carbon; Atmospheric Chemistry and Physics 10 (2010) 4207-4220; doi:10.5194/acp-10-4207-2010

[23] Liu F, Yon J., Bescond A.; On the radiative properties of soot aggregates – Part 2: Effects of coating; Journal of Quantitative spectroscopy & Radiative transfer 172 (2016) 134-145; https://doi.org/10.1016/j.jqsrt.2015.08.005

[24] Bond T.C., Bergstrom R.W.; Light Absorption by Carbonaceous Particles: An Investigative Review; Aerosol Science and Technology 40 (2006) 27-67; doi: 10.1080/02786820500421521

[25] IPCC Climate Change 2013: The Physical Science Basis (Working Group I Contribution to the Fifth Assessment Report of the Intergovenmental Panel on Climate Change - IPCC), http://www.ipcc.ch/report/ar5/wg1/

[26] Watson J.G.; Visibility: science and regulation; Journal of the Air and Waste Management Association 52 (2002) 628-713

[27] Chang D., Song Y., Liu B.; Visibility trends in six megacities in China 1973-2007; Atmospheric Research 94 (2009) 161-167; doi:10.1016/j.atmosres.2009.05.006

[28] Koschmieder H.; Theorie der horizontalen Sichtweite; Beiträge zur Physik der freien Atmosphäre 12 (1924) 33-53

[29] Müller T., Henzing J.S., de Leeuw G., Alastuey A., Angelow H., Bizjak M., Collaud Coen M., Engström J.E., Gruening C., Hillamo R., Hoffer A., Imre K., Ivanow P., Jennings G., Sun J.Y., Kalivitis N., Karlsson H., Komppula M., Laj P., Li S.M., Lunder C., Marinoni A., Martins dos Santos S., Moerman M., Nowak A., Ogren J.A., Petzold A., Pichon J.M., Rodriquez S., Sharma S., Sheridan P.J., Teinilä K., Tuch T., Viana M., Weingartner E., Wilhelm R., Wang Y.Q.; Characterization and intercomparison of aerosol absorption photometers: results of two intercomparison workshops; Atmospheric Measurement Techniques 4 (2011) 245-268; doi:10.5194/amt-4-245-2011

[30] Onasch T.B., Massoli P., Kebabian P.L., Hills F.B., Bacon F., and Freedman A.; Single Scattering Albedo Monitor for Airborne Particulates; Aerosol Science and Technology 49 (2015) 267-279; doi: 10.1080/02786826.2015.1022248

[31] Varma R.M.K., Moosmüller H., Arnott W.P; Toward an ideal integrating nephelometer; Optics Letters 28 (2003) 1007-1009; doi: 10.1364/OL.28.001007

[32] Heintzenberg J., Charlson R.J.; Design and Applications of the Integrating Nephelometer: A Review; Journal of Atmospheric and Oceanic Technology 13 (1996) 987-1000

[33] Anderson T.L, Ogren J.A.; Determining aerosol radiative properties using the TSI 3563 integrating nephelometer; Aerosol Science and Technology 29 (1998) 57-69

[34] Bond T. C., Covert D.S., Müller T.; Truncation and Angular- Scattering Corrections for Absorbing Aerosol in the TSI 3563 Nephelometer; Aerosol Science and Technology 43 (2009) 866-871; doi: 10.1080/02786820902998373

[35] Massoli P., Murphy D.M., Lack D.A., Baynard T., Brock C.A., and Lovejoy E.R.; Uncertainty in Light Scattering Measurements by TSI Nephelometer: Results from Laboratory Studies and Implications for Ambient Measurements; Aerosol Science and Technology 43 (2009) 1064-1074; doi: 10.1080/02786820903156542

[36] Müller T., Laborde M., Kassell G., Wiedensohler A.; Design and performance of a three-wavelength LED-based total scatter and backscatter integrating nephelometer; Atmospheric Measurement Techniques 4 (2011) 1291–1303 doi:10.5194/amt-4-1291-2011

[37] Petzold A., Schönlinner M.; Multi-angle absorption photometry – a new method for the measurement of aerosol light absorption and atmospheric black carbon; Journal of Aerosol Science 35 (2004) 421-441; doi:10.1016/j.jaerosci.2003.09.005

[38] Petzold A., Schloesser H., Sheridan P.J., Arnott W.P., Ogren J.A., Virkkula A.; Evaluation of Multiangle Absorption Photometry for Measuring Aeroosl Light Absorption; Aerosol Science and Technology 39 (2005) 40-51; doi: 10.1080/027868290901945

[39] Bond T.C., Anderson T.L., and Campbell D.; Calibration and Intercomparison of Filter-Based Measurements of Visible Light Absorption by Aerosols; Aerosol Science and Technology 30 (1999) 582-600

[40] Weingartner E., Saathoff H., Schnaiter M., Streit N., Bitnar B., Baltensperger U.; Absorption of light by soot particles: determination of the absorption coefficient by means of aethalometers; Journal of Aerosol Science 34 (2003) 1445-1463; doi:10.1016/S0021-8502(03)00359-8

[41] Virkkula A., Ahlquist N.C., Covert D.S., Arnott W.P., Sheridan P.J., Quinn P.K., and Coffman D.J.; Modification, Calibration and a Field Test of an Instrument for Measuring Light Absorption by Particles; Aerosol Science and Technology 39 (2005) 68-83; doi: 10.1080/027868290901963

[42] Virkkula A.; Correction of the Calibration of the 3-wavelength Particle Soot Absorption Photometer (3λ PSAP); Aerosol Science and Technology 44 (2010) 706-712; doi: 10.1080/02786826.2010.482110

[43] Ogren J.A.; Comment on "Calibration and Intercomparison of Filter-Based Measurements of Visible Light Absorption by Aerosols"; Aerosol Science and Technology 44 (2010) 589-591; doi: 10.1080/02786826.2010.482111

[44] Müller T., Virkkula A., and Ogren J.A.; Constrained two-stream algorithm for calculating aerosol light absorption coefficient from the Particle Soot Absorption Photometer; Atmospheric Measurement Techniques 7 (2014) 4049-4070; doi: 10.5194/amt-7-4049-2014

[45] Vecchi R., Bernardoni V., Paganelli C., Valli G.; A filter-based light-absorption measurement with polar photometer: effects of sampling artefacts from organic carbon; Journal of Aerosol Science 70 (2014) 15-25; http://dx.doi.org/10.1016/j.jaerosci.2013.12.012

[46] Bernardoni V., Valli G., Vecchi R.; Set-up of a multi wavelength polar photometer for off-line absorption coefficient measurements on 1-h resolved aerosol samples; Journal of Aerosol Science 107 (2017) 84-93; http://dx.doi.org/10.1016/j.jaerosci.2017.02.009

[47] Hänel G.; Radiation Budget of the Boundary Layer. Part 2: Simultaneous Measurement of Mean Solar Volume Absorption and Extinction Coefficients of Particles; Beltr. Phys. Atmosph. 50 (2) (1987)

[48] Coakley J.A., Chýlek P.; The Two-Stream Approximation in Radiative Transfer: Including the Angle of the Incident Radiation; Journal of the Atmospheric Sciences 32 (1975) 409-418

[49] Valentini S.; Determinazione dei coefficienti di assorbimento ed estinzione a più lunghezze d'onda in campioni di aerosol atmosferico mediante approcci sperimentali e modellistici; Master Degree Thesis in Physics (2016)

[50] Massabò D., Bernardoni V., Bove M.C., Brunengo A., Cuccia E., Piazzalunga A., Prati P., Valli G., Vecchi R.; A multi-wavelength optical set-up for the characterization of carbonaceous particulate matter; Journal of Aerosol Science 60 (2013) 34-46; http://dx.doi.org/10.1016/j.jaerosci.2013.02.006

[51] Massabò D., Caponi L., Bernardoni V., Bove M.C., Brotto P., Calzolai G., Cassola F., Chiari M., Fedi M.E., Fermo P., Giannoni M., Lucarelli F., Nava S., Piazzalunga A., Valli G., Vecchi R., Prati P.; Multi-wavelength optical determination of black and brown carbon in atmospheric aerosols; Atmospheric Environment 108 (2015) 1-12; http://dx.doi.org/10.1016/j.atmosenv.2015.02.058

[52] Bernardoni V., Pileci R.E., Caponi L., Massabò D.; The Multi-Wavelength Absorption Analyzer (MWAA) Model as a Tool for Source and Component Apportionment Based on Aerosol Absorption Properties: Application to Samples Collected in Different Environments; Atmosphere 8 (2017) doi:10.3390/atmos8110218

[53] Saturno J., Pöhlker C., Massabò D., Brito J., Carbone S., Cheng Y., Chi X., Ditas F., de Angelis I.H., Morán-Zuloaga D., Pöhlker M.L., Rizzo L.V., Walter D., Wang Q., Artaxo P., Prati P. ,and Andreae M.O.; Comparison of different Aethalometer correction schemes and a reference multi-wavelength absorption technique for ambient aerosol data; Atmospheric Measurement Techniques 10 (2017) 2837-2850; https://doi.org/10.5194/amt-10-2837-2017

[54] Valentini S., Weber P., Bernardoni V., Bundke U., Massabò D., Petzold A., Prati P., Valli G., Vecchi R.; Multi-Wavelength Measurement of Aerosol Optical Properties: Laboratory Intercomparison of In-situ and Filter-based Techniques; Poster presentation at the 12th International Conference on Carbonaceous Particles in the Atmosphere (ICCPA) Vienna, 3-6 April 2019

[55] Kazemimanesh M., Moallemi A., Thomson K., Smallwood G., Lobo P., and Olfert J.S.; A novel miniature inverted-flame burner for the generation of soot nanoparticles; Aerosol Science and Technology 53 (2) (2019) 184-195; doi:10.1080/02786826.2018.1556774

[56] Moallemi A., Kazemimanesh M., Corbin J.C., Thomson K., Smallwood G., Olfert J.S., Lobo P.; Characterisation of black carbon particles generated by a propane-fueled miniature inverted soot generator; Journal of Aerosol Scince 135 (2019) 46-57 https://doi.org/10.1016/j.jaerosci.2019.05.004

[57] Petzold A., Onasch T., Kebabian P., and Freedman A.; Intercomparison of a Cavity Attenuated Phase Shift-based extinction monitor (CAPS PMex); with an integrating nephelometer and a filter-based absorption monitor; Atmospheric Measurement Techniques 6 (2013) 1141-1151; https://doi.org/10.5194/amt-6-1141-2013

[58] Perim de Faria J., Bundke U., Freedman A., Onasch T.B., and Petzold A.; Laboratory Validation and Field Deployment of a Compact Single-Scattering Albedo (SSA) Monitor; Atmospheric Measurement Techniques Discussion (2019) https://doi.org/10.5194/amt-2019-146

[59] Weber P., Bundke U., Bischof O., Fischer B., Berg M., Petzold A.; Assessing Multi-Spectral Measurement Methods for Aerosol Optical Properties by an Extensive Closure Study for Different Aerosol Types; Poster presentation at the 12th

International Conference on Carbonaceous Particles in the Atmosphere (ICCPA) Vienna, 3-6 April 2019

[60] Gyawali M., Arnott W.P., Lewis K., Moosmüller H.; In situ aerosol optics in Reno, NV, USA during and after the summer 2008 California wildfires and the influence of absorbing and non-absorbing organic coatings on spectral light absorption; Atmospheric Chemistry and Physics 9 (2019) 8007-8015 www.atmos-chem-phys.net/9/8007/2009/

[61] Massimi L., Ristorini M., Eusebio M., Florendo D., Adeymo A., Brugnoli D., and Canepari S.; Monitoring and Evaluation of Terni (Cetral Italy) Air Quality through Spatially Resolved Analyses; Atmosphere 8 (200) (2017) doi:10.3390/atmos8100200

[62] Hansen A.D.A., Rosen H., and Novakov T.; The aethalometer - an instrument for the real-time measurement of optical absorption by aerosol particles; Science of the Total Environment 36 (1984) 191-196

[63] Drinovec L., Močnik G., Zotter P., Prévôt A.S.H., Ruckstuhl C., Coz E., Rupakheti M., Sciare J., Müller T., Wiedensohler E., and Hansen D.A.; The "dual-spot" Aethalometer: an improved measurement of aerosol black carbon with real-time loading compensation; Atmospheric Measurement Techniques 8 (2015) 1965-1979; doi:10.5194/amt-8-1965-2015

[64] Aerosol d.o.o.; Magee Scientific Aethalometer® Model AE33 - User Manual; Version 1.54 (2016)

[65] Virkkula A., Mäkelä T., Hillamo R., Yli-Tuomi T., Hirsikko A., Hämeri K., and Koponen I.K.; A Simple Procedure for Correcting Loading Effects of Aethalometer Data; Journal of the Air and Waste Management Association 57 (2007) 1214-1222; doi: 10.3155/1047-3289.57.10.1214

[66] Petzold A., Ogren J.A., Fiebig M., Laj P., Li S.-M., Baltensperger U., Holzer-Popp U., Kinne T., Pappalardo G., Sugimoto N., Wehrli G., Wiedensohler A., Zhang X.-Y.; Recommendations for reporting "black carbon" measurements; Atmospheric Chemitry and Physics 13 (2013) 8365-8379; doi:10.5194/acp-13-8365-2013

[67] Collaud Coen M., Weingartner E., Apituley A., Ceburnis D., Fierz-Schmidhauser R., Flentje H., Henzing J.S., Jennings S.G., Moerman M., Petzold A., Schmid O., and Baltensperger U.; Minimizing light absorption measurement artifacts of the Aethalometer: evaluation of five correction algorithms; Atmospheric Measurement Techniques 3 (2010) 457–474; www.atmos-meas-tech.net/3/457/2010/

[68] Di Biagio C., Formenti P., Cazaunau M., Pangui E., Marchand N., and Doussin J.-F.; Aethalometer multiple scattering correction C_{ref} for mineral dust aerosols; Atmospheric Measurement Techniques 10 (2017) 613-625; https://doi.org/10.5194/amt-10-2923-2017

[69] Titos G., del Águila A., Cazorla A., Lyamani H., Casquero-Vera J.A., Colombi C., Cuccia E., Gianelle V., Močnik G., Alastuey A., Olmo F.J., Alados-Alarboledas L.; Spatial and temporal variability of carbonaceous aerosols: Assessing the impact of biomass burning in the urban environment; Science of the Total Environment 578 (2017) 2923-2939; doi:10.1002/2016JD026252

[70] Segura S., Estellés V., Titos G., Lyamani H., Utrillas M.P., Zortter P., Prévôt A.S.H., Močnik G., Alados-Alarboledas L., and Martínez-Lozano J.A.; Determination and analysis of in situ spectral aerosol optical properties by a multi-instrumental approach; Atmospheric Measurment Techniques 7 (2014) 2373–2387; doi:10.5194/amt-7-2373-2014

[71] Arnott W.P., Hamasha K., Moosmüller H., Sheridan P.J., and Ogren J.A.; Towards Aerosol Light-Absorption Measurements with a 7-Wavelength Aethalometer: Evaluation with a Photoacoustic Instrument and 3-Wavelength Nephelometer; Aerosol Science and Technology 39 (2005) 17-29; doi: 10.1080/027868290901972

[72] Schmid O., Artaxo P., Arnott W.P., Chand D., Gatti L.V., Frank G.P., Hoffer A., Schnaiter M., and Andreae M.O.; Spectral light absorption by ambient aerosols influenced by biomass burning in the Amazon Basin. I: Comparison and field calibration of absorption measurement techniques; Atmospheric Chemistry and Physics 6 (2006) 3443–3462; www.atmos-chem-phys.net/6/3443/2006/

[73] Ecotech; Aurora 4000 Polar Nephelometer User Manual; 1.0 edition (2011)

[74] Purcell E.M., Pennypacker C.; Scattering and absorption of light by non spherical dielectric grains; The Astrophysical Journal 186 (1973) 705-714

[75] Horvath H., Alados-Alarboledas L., Olmo Reyes F.J.; Angular scattering of the Sahara dust aerosol; Atmospheric Chemistry and Physics 18 (2018) 17735–17744; https://doi.org/10.5194/acp-18-17735-2018

[76] Horvath H.; Extrapolation of a truncated aerosol volume scattering function to the far forward and back region; Journal of Aerosol Science 90 (2015) 26–35; http://dx.doi.org/10.1016/j.jaerosci.2015.08.001

[77] Reischl G.P.; Measurement of Ambient Aerosols by the Differential Mobility Analyzer Method: Concepts and Realization Criteria for the Size Range

Between 2 and 500 nm; Aerosol Science and Technology 14 (1991) 5-24; doi: 10.1080/02786829108959467

[78] von der Weiden S.-L., Drewnick F., Borrmann S.; Particle Loss Calculator – a new software tool for the assessment of the performance of aerosol inlet systems; Atmospheric Measurement Techniques 2 (2009) 479–494; www.atmos-meas-tech.net/2/479/2009/

[79] Gasteiger J., Wiegner M.; Mopsmap v1.0: a versatile tool for the modeling of aerosol optical properties; Geoscientific Model Development 11 (2018) 2739–2762; https://doi.org/10.5194/gmd-11-2739-2018

[80] Müller T., Paixão M., Wiedensohler A.; Scattering Coefficients and Asymmetry Parameters derived from the Polar Nephelometer Aurora4000; Accepted abstract at the European Aerosol Conference EAC 2012 - Granada (Spain)

[81] Pitchford M., Malm W., Schichtel B., Kumar N., Lowenthal D., Hand J.; Revised Algorithm for Estimating Light Extinction from IMPROVE Particle Speciation Data; Journal of the Air and Waste Management Association 57 (2007) 1326-1336; http://dx.doi.org/10.3155/1047-3289.57.11.1326

[82] Malm W.C., Sisler J.F., Huffman D., Eldred R.A., Cahill T.A.; Spatial and seasonal trends in particle concentration and optical extinction in the United States; Journal of Geophysical Research 99 (1994) 1347-1370

[83] Jung J., Lee H., Kim Y.J., Liu X., Zhang Y., Gu J., Fan S.; Aerosol chemistry and the effect of aerosol water content on visibility impairment and radiative forcing in Guangzhou during the 2006 Pearl River Delta Campaign; Journal of Environmental Management 90 (2009) 3231-3244; doi:10.1016/j.jenvman.2009.04.021

[84] Cao J., Wang Q., Chow J.C., Watson J.G., Tie X., Shen Z., Wang P., An Z.; Impacts of aerosol composition on visibility impairment in Xi'an, China; Atmospheric Environment 59 (2012) 559-566; http://dx.doi.org/10.1016/j.atmosenv.2012.05.036

[85] Shen G., Xue M., Yuan S., Zhang J., Zhao Q., Li B., Wu H., Ding A.; Chemical compositions and reconstructed light extinction coefficients of particulate matter in a mega-city in the western Yangtze River Delta, China; Atmospheric Environment 83 (2014) 14-20; http://dx.doi.org/10.1016/j.atmosenv.2013.10.055

[86] Tao J., Zhang L., Ho K., Zhang R., Lin Z., Zhang Z., Lin M., Cao J., Liu S., Wang G.; Impact of PM2.5 chemical compositions on aerosol light scattering in

Guangzhou — the largest megacity in South China; Atmospheric Research 135-136 (2014) 48-58; http://dx.doi.org/10.1016/j.atmosres.2013.08.015

[87] Wang H., Li X., Shi G., Cao J., Li C., Yang F., Ma Y., He K.; PM2.5 Chemical Composition and Aerosol Optical Properties in Beijing during the Late Fall; Atmosphere 6 (2015) 164-182; doi:10.3390/atmos6020164

[88] Wang H., Tian M., Li X., Chang Q., Cao J., Yang F., Ma Y., He K.; Chemical Composition and Light Extinction Contribution of PM2.5 in Urban Beijing for a 1-Year Period; Aerosol and Air Quality Research 15 (2015) 220-2211; doi: 10.4209/aaqr.2015.04.0257

[89] Deng J., Zhang Y., Hong Y., Xu L., Chen Y., Du W., Chen J.; Optical properties of PM2.5 and the impacts of chemical composition in the coastal city Xiamen in China; Science of the Total Environment 557-558 (2016) 665-675; http://dx.doi.org/10.1016/j.scitotenv.2016.03.143

[90] Hand J.L., Malm W.C.; Review of aerosol mass scattering efficiecies from ground-based measurements since 1990; Journal of Geophysical Research 112 (2007) D16203; doi:10.1029/2007JD008484, 2007

[91] Valentini S., Bernardoni V., Massabò D., Prati P., Valli G., Vecchi R.; Tailored coefficients in the algorithm to assess reconstructed light extinction at urban sites: A comparison with the IMPROVE revised approach; Atmospheric Environment 172 (2018) 168-176; https://doi.org/10.1016/j.atmosenv.2017.10.038

[92] Vecchi R., Marcazzan G., Valli G., Ceriani M., Antoniazzi C.; The role of atmospheric dispersion in the seasonal variation of PM1 and PM2.5 concentration and composition in the urban area of Milan (Italy); Atmospheric Environment 38 (2004) 4437-4446; doi:10.1016/j.atmosenv.2004.05.029

[93] Lowenthal D.H., Zielinska B., Samburova V., Collins D., Taylor N., Kumar N.; Evaluation of assumptions for estimating chemical light extinction at U.S. national parks; Journal of the Air and Waste Management Association 65 (2015) 249-260; doi: 10.1080/10962247.2014.986307

[94] Elser Fritsche M.; Le particelle ultrafini in atmosfera: metodi di campionamento e caratterizzazione; Master Degree Thesis in Physics (2012)

[95] Bernardoni V., Elser M., Valli G., Valentini S., Bigi A., Fermo P., Piazzalunga A., Vecchi R.; Size-segregated aerosol in a hot-spot pollution urban area: Chemical composition and three-way source apportionment; Environmental Pollution 231 (2017) 601-611; http://dx.doi.org/10.1016/j.envpol.2017.08.040

[96] Hand J.L., Schichtel B.A., Pitchford M., Malm W.C., Frank N.H.; Seasonal composition of remote and urban fine particulate matter in the United States; Journal of Geophysical Research 117 (2012) D05309; doi:10.1029/2011JD017122, 2012

[97] Vecchi R., Bernardoni V., Fermo P., Lucarelli F., Mazzei F., Nava S., Prati P., Piazzalunga A., Valli G.; 4-hours resolution data to study PM10 in a "hot spot" area in Europe; Environ. Monit. Assess. 154 (2009) 283-300; doi: 10.1007/s10661-008-0396-1

[98] Marcazzan G.M., Ceriani M., Valli G., Vecchi R.; Composition, components and sources of fine aerosol fractions using multielemental EDXRF analysis; X-Ray Spectrometry 33 (2004) 267-272; doi: 10.1002/xrs.719

[99] Piazzalunga A., Bernardoni V., Fermo P., Valli G., Vecchi R.; Technical Note: On the effect of water-soluble compounds removal on EC quantification by TOT analysis in urban aerosol samples; Atmospheric Chemistry and Physics 11 (2011) 10193–10203; doi: 10.5194/acp-11-10193-2011

[100] Panteliadis P, Hafkenscheid T., Cary B., Diapouli E., Fischer A., Favez O., Quincey P., Viana M., Hitzenberger R., Vecchi R., Saraga D., Jaffrezo J.L., John A., Schwartz J., Giannoni M., Novak J., Karanasiou A., Fermo P., Maenhaut W.; ECOC comparison exercise with identical thermal protocols after temperature offset correction – instrument diagnostics by in-depth evaluation of operational parameters; Atmospheric Measurement Techniques 8 (2015) 779-792; doi:10.5194/amt-8-779-2015

[101] Yurkin M. A., A. G. Hoekstra A. G.; The discrete-dipole-approximation code ADDA: capabilities and known limitations; Journal of Quantitative Spectroscopy and Radiative Transfer 112 (2011) 2234-2247; doi:10.1016/j.jqsrt.2011.01.031

[102] Shelley R.U., Morton P.L., Landing W.M.; Elemental ratios and enrichment factors in aerosols from the US-GEOTRACES North Atlantic transects; Deep-Sea Research II: Topical Studies in Oceanography 116 (2015) 262-272; https://doi.org/10.1016/j.dsr2.2014.12.005

[103] Fernàndez-Olmo I., Andecochea C., Ruiz S., Fernàndez-Ferreras J.A., Irabien A.; Local source identification of trace metals in urban/industrial mixed land-use areas with daily PM10 limit value exceedances; Atmospheric Research 171 (2016) 92-16; https://doi.org/10.1016/j.atmosres.2015.12.010

[104] Megido L., Negral L., Castrillòn L., Suàrez-Peña B., Fernàndez-Nava Y., Marañòn E.; Enrichment factors to assess the anthropogenic influence on PM10

in Gijón (Spain); Environmental Science and Pollution Research 24 (2017) 711–724; doi: 10.1007/s11356-016-7858-8

[105] Lightstone J.M., Onasch T.B., Imre D.; Deliquescence, Efflorescence, and Water Activity in Ammonium Nitrate and Mixed Ammonium Nitrate/Succinic Acid Microparticles; Journal of Physical Chemistry 104 (2000) 9337-9346; doi: 10.1021/jp002137h

[106] Lowenthal D.H., Kumar N.; Evaluation of the IMPROVE Equation for Estimating aerosol light extinction; Journal of the Air and Waste Management Association 66 (2016) 726-737; doi: 10.1080/10962247.2016.1178187

[107] Curci G., Hogrefe C., Bianconi R., Im U., Balzarini A., Barò R., Brunner D., Forkel R., Giordano L., Hirtl M., Honzac L., Jiménez-Guerrero P., Knote C., Langer M., Makar P.A., Pirovano G., Pérez J.L., San José R., Syrakov D., Tuccella P., Werahn J., Wolke R., Žabkar R., Zhang J., Galmarini S.; Uncertainties of simulated aerosol optical properties induced by assumptions on aerosol physical and chemical properties: an AQMEII-2 perspective; Atmospheric Environment 115 (2015) 541-552; https://doi.org/10.1016/j.atmosenv.2014.09.009s

[108] Gao Y., Lai S., Lee S.-C., Yau P.S., Huang Y., Cheng Y., Wang T., Xu Z., Yuan C., Zhang Y.; Optical properties of size-resolved particles at Hong Kong urban site during winter; Atmospheric Research 155 (2015) 1-12; http://dx.doi.org/10.1016/j.atmosres.2014.10.020

[109] EPA (U.S Environmental Protection Agency); Guidance for Tracking Progress Under the Regional Haze Rule (2003)

[110] Hand J. L., Copeland S. A., Day D. E., Dillner A. M., Indresand H., Malm W. C., McDade C. E., Moore C. T. Jr., Pitchford M. L., Schichtel B.A., Watson J. G.; IMPROVE (Interagency Monitoring of Protected Visual Environments): Spatial and seasonal patterns and temporal variability of haze and its constituents in the United States; Report. V, Cooperative Institute For Research In the Atmosphere, (2011) Colorado State University Fort Collins, CO. (Available at http://vista.cira.colostate.edu/improve/Publications/Reports/2011/2011.htm)

[111] Vecchi R., Bernardoni V., Valentini S., Piazzalunga A., Fermo P, Valli G.; Assessment of light extinction at a European polluted urban area during wintertime: Impact of PM_1 composition and sources; Atmospheric Environment 233 (2018) 679-689; https://doi.org/10.1016/j.envpol.2017.10.059

[112] Costabile F., Alas H., Aufderheide M., Avino P., Amato F., Argentini S., Barnaba F., Berico M., Bernardoni V., Biondi R., Calzolai G., Canepari S., Casasanta

G., Ciampichetti S., Conidi A., Cordelli E., Di Ianni A., Di Liberto L., Facchini M. C., Facci A., Frasca D., Gilardnoni S., Grollino M. G., Gualtieri M., Lucarelli F., Malaguti A., Manigrasso M., Montagnoli M., Nava S., Padoan E., Perrino C., Petralia E., Petenko I., Querol X., Simonetti G., Tranfo G., Ubertini S., Valli G., Valentini S., Vecchi R., Volpi F., Weinhold K., Wiedensholer A., Zanini G., Gobbi G. P.; First Results of the "Carbonaceous Aerosol in Rome and Environs (CARE)" Experiment: Beyond Current Standards for PM_{10}; Atmosphere 8 (2017) doi:10.3390/atmos8120249

[113] Valentini S., Barnaba F., Bernardoni V., Calzolai G., Costabile F., Di Liberto L., Forello A.C., Gobbi G.P., Gualtieri M., Lucarelli F., Nava S., Petralia E., Valli G., Wiedensohler A., Vecchi R.; Classifying aerosol particles through the combination of optical and physical-chemical properties: Results from a wintertime campaign in Rome (Italy); submitted to Atmospheric Research (2019)

[114] Barnaba F., Gobbi G.P.; Aerosol seasonal variability over the Mediterranean region and relative impact of maritime, continental and Saharan dust particles over the basin from MODIS data in the year 2001; Atmospheric Chemistry and Physics 4 (2004) 2367–2391; doi: 10.5194/acpd-4-4285-2004

[115] Gobbi G. P., Kaufman Y. J., Koren I., Eck T. F.; Classification of aerosol properties derived from AERONET direct sun data; Atmospheric Chemistry and Physics 7 (2007) 453–458; www.atmos-chem-phys.net/7/453/2007/

[116] Barnaba F., Bolignano A., Di Liberto L., Morelli M., Lucarelli F., Nava S., Perrino C., Canepari S., Basart S., Costabile F., Dionisi D., Ciampichetti S., Sozzi R., Gobbi G.P.; Desert dust contribution to PM10 loads in Italy: Methods and recommendations addressing the relevant European Commission Guidelines in support to the Air Quality Directive 2008/50; Atmospheric Environment 161 (2017) 288-305; http://dx.doi.org/10.1016/j.atmosenv.2017.04.038

[117] Gobbi G. P., Barnaba F., Di Liberto L., Bolignano A., Lucarelli F., Nava S., Perrino C., Pietrodangelo A., Basart S., Costabile F., Dionisi D., Rizza U., Canepari S., Sozzi R., Morelli M., Manigrasso M., Drenwick F., Stuckmeier C., Poenitz K., Wille K.; An inclusive view of Saharan dust advections to Italy and the Central Mediterranean; Atmospheric Environment 201 (2019) 242–256; https://doi.org/10.1016/j.atmosenv.2019.01.002

[118] Perrino C., Canepari S., Catrambone M., Dalla Torre S., Rantica E., Sargolini T.; Influence of natural events on the concentration and composition of atmospheric particulate matter; Atmospheric Environment 43 (2009) 4766–4779 doi:10.1016/j.atmosenv.2008.06.035

[119] Costabile F., Gualtieri M., Canepari S., Tranfo G., Consales C., Grollino M.G., Paci E., Petralia E., Pigini D., Simonetti G.; Evidence of association between aerosol properties and in-vitro cellular oxidative response to PM1, oxidative potential of PM2.5, a biomarker of RNA oxidation, and its dependency on the combustion aerosol; Atmospheric Environment 213 (2019) 445-455; doi 10.1016/j.atmosenv.2019.06.023

[120] Douglas Goetz J., Giordano M.R., Stockwell C.E., Christian T.J., Maharian R., Adhikari S., Bhave P.V., Praveen P.S., Panday A.K., Jayarathne T., Stone E.A., Yokelson R.J., DeCarlo P.F.; Speciated online PM1 from South Asian combustion sources – Part1: Fuel-based emission factors and size distributions; Atmospheri Chemistry and Physics 18 (2018) 14653–14679; https://doi.org/10.5194/acp-18-14653-2018

[121] Hyvärinen A.-P., Vakkari V., Laasko L., Hooda R.K., Sharma V.P., Panwar T.S., Beukes J.P., van Zyl P., Josipovic M., Garland R.M., Andreae M.O., Pöschl U., Petzold A.; Correction for a measurement artifact in the Multi-Angle Absorption Photometer (MAAP) at high black carbon mas concentration levels; Atmospheric Measurement Techniques 6 (2013) 81-90; doi:10.5194/amt-6-81-2013

[122] Calzolai G., Lucarelli F., Chiari M., Nava S., Giannoni M., Carraresi L., Prati P., Vecchi R.; Improvements in PIXE analysis of hourly particulate matter samples; Nucl. Instr. Meth. B 363 (2015) 99–104; https://doi.org/10.1016/j.nimb.2015.08.022

[123] Ng N.L., Herndon S.C., Trimborn A., Canagaratna M.R., Croteau P., Onasch T.M., Sueper D., Worsnop D.R., Zhang Q., Sun Y.L., Jayne J.T.; An Aerosol Chemical Speciation Monitor (ACSM) for routine monitoring of atmospheric aerosol composition; Aerosol Science and Technology 45 (2011) 770–784; doi: 10.1080/02786826.2011.560211

[124] Canonaco F., Crippa M., Slowik J.G., Baltensperger U., Prévôt A.S.H.; SoFi, an IGOR-based interface for the efficient use of the generalized multilinear engine (ME-2) for the source apportionment: ME-2 application to aerosol mass spectrometer data; Atmospheric Measurement Techniques 6 (2013) 3649–3661; doi:10.5194/amt-6-3649-2013

[125] Khlystov A., Stanier C., Pandis S.N.; An algorithm for combining electrical mobility and aerodynamic size distributions data when measuring ambient aerosol special issue of aerosol science and technology on findings from the fine particulate matter supersites program; Aerosol Science and Technology 38 (2004) 229–238; doi: 10.1080/02786820390229543

[126] Alas H.D.C., Weinhold K., Costabile F. Di Ianni A., Müller T., Pfeifer S., Di Liberto L., Turner J.R., Wiedensohler A.; Methodology for High Quality Mobile Measurement with Focus on Black Carbon and Particle Mass Concentrations; Atmospheric Measurement Techniques 12 (2019) 4697-4712 https://doi.org/10.5194/amt-12-4697-2019

[127] Dubovik O., Holben B., Eck T. F., Smirnov A., Kaufman Y. J., King M. D., Tanré D., Slutsker I.; Variability of Absorption and Optical Properties of Key Aerosol Types Observed in Worldwide Locations; Journal of the Atmospheric Sciences 59 (2002) 590-608

[128] Kalapureddy M. C. R., Kaskaoutis D. G., Raj P. E., Devara P. C. S., Kambezidis H. D., Kosmopoulos P. G., Nastos P. T.; Identification of aerosol type over the Arabian Sea in the premonsoon season during the Integrated Campaign for Aerosol, Gases and Radiation Budget (ICARB); Journal of Geophysical Research, Vol. 114, D17203 (2009); doi:10.1029/2009JD011826

[129] Russell P. B., Bergstrom R. W., Shinozuka Y., Clarke A. D., DeCarlo P. F., Jimenez J. L., Livingston J. M., Redemann J., Dubovik O., Strawa A.; Absorption Angstrom Exponent in AERONET and related data as an indicator of aerosol composition; Atmospheric Chemistry and Physics 10 (2010) 1155–1169; www.atmos-chem-phys.net/10/1155/2010/

[130] Giles D.M., Holben B.N., Tripathi S.N., Eck T.F., Newcomb W.N., Slutsker I., Dickerson R.R., Thompson A.M., Mattoo S., Wang S.-H., Singh R.P., Sinyuk A., Schafer J.S.; Aerosol properties over the Indo-Gangetic Plain: A mesoscale perspective from the TIGERZ experiment; Journal of Geophysical Research 116, D18203 (2011); doi:10.1029/2011JD015809

[131] Giles D.M., Holben B.N., Eck T.F., Sinyuk A., Smirnov A., Slutsker I., Dickerson R.R., Thompson A.M., Schafer J.S.; An analysis of AERONET aerosol absorption properties and classifications representative of aerosol source regions; Journal of Geophysical Research 117, D17203 (2012); doi:10.1029/2012JD018127

[132] Cazorla A., Bahadur R., Suski K.J., Cahill J.F., Chand D., Schmid B., Ramanathan V., Prather K.A.; Relating aerosol absorption due to soot, organic carbon, and dust to emission sources determined from in-situ chemical measurements; Atmospheric Chemistry and Physics 13 (2013) 9337–9350; doi:10.5194/acp-13-9337-2013

[133] Rupakheti D., Kang S., Bilal M., Gong J., Xia X., Cong Z.; Aerosol optical depth climatology over Central Asian countries based on Aqua-MODIS Collection

6.1 data: Aerosol variations and sources; Atmospheric Environment 207 (2019) 205-214; https://doi.org/10.1016/j.atmosenv.2019.03.020

[134] Yang M., Howell S.G., Zhuang J., Huebert B.J.; Attribution of aerosol light absorption to black carbon, brown carbon, and dust in China – interpretations of atmospheric measurements during EAST-AIRE; Atmospheric Chemistry and Physics 9 (2009) 2035–2050; www.atmos-chem-phys.net/9/2035/2009/

[135] Lee S., Yoo S.-C., Lim S.-W., Kim Y. P., Ghim Y.S., Kim J.-H., Kang C.-H., Kim Y.J., Chang L.-S., Lee S.-J.; Spectral dependency of light scattering/absorption and hygroscopicity of pollution and dust aerosols in Northeast Asia; Atmospheric Environment 50 (2012) 246-254; doi:10.1016/j.atmosenv.2011.12.026

[136] Costabile F., Barnaba F., Angelini F., Gobbi G.P.; Identification of key aerosol populations through their size and composition resolved spectral scattering and absorption; Atmospheric Chemistry and Physics 13 (2013) 2455–2470; doi:10.5194/acp-13-2455-2013

[137] Cappa C.D., Kolesar K.R., Zhang X., Atkinson D.B., Pekour M.S., Zaveri R.A., Zelenyuk A., Zhang Q.; Understanding the optical properties of ambient sub- and supermicron particulate matter: results from the CARES 2010 field study in northern California; Atmospheric Chemistry and Physics 16 (2016) 6511–6535; doi:10.5194/acp-16-6511-2016

[138] Romano S., Perrone M.R., Pavese G., Esposito F., Calvello M.; Optical properties of PM2.5 particles: Results from a monitoring campaign in southeastern Italy; Atmospheric Environment 203 (2019) 35–47; https://doi.org/10.1016/j.atmosenv.2019.01.037

[139] Schmeisser L., Andrews E., Ogren J.A., Sheridan P., Jefferson A., Sharma S., Kim J.E., Sherman J.P., Sorribas M., Kalapov I., Arsov T., Angelov C., Mayol-Bracero O.M., Labuschagne C., Kim S.-W., Hoffer A., Lin N.-H., Chia H.-P., Bergin M., Sun J., Liu P., Wu H.; Classifying aerosol type using in situ surface spectral aerosol optical properties; Atmospheric Chemistry and Physics 17 (2017) 12097–12120; https://doi.org/10.5194/acp-17-12097-2017

[140] Timonen H., Aurela M., Carbone S., Saarnio K., Saarikoski S., Mäkelä T., Kulmala M., Kerminen V.-M., Worsnop D.R., and Hillamo R.; High time-resolution chemical characterization of the water-soluble fraction of ambient aerosols with PILS-TOC-IC and AMS; Atmospheric Measurement Techniques 3 (2010) 1063–1074; doi:10.5194/amt-3-1063-2010

[141] Lucarelli F., Chiari M., Calzolai G., Giannoni M., Nava S., Udisti R., Severi M., Querol X., Amato F., Alves C., Eleftheriasdis K.; The role of PIXE in the AIRUSE project "testing and development of air quality mitigation measures in Southern Europe"; Nuclear Instruments and Methods in Physics Research B 363 (2015) 92–98; http://dx.doi.org/10.1016/j.nimb.2015.08.023

[142] Eck T.F., Holben B.N., Reis J.S., Dubovik O., Smirnov A., O'Neill N.T., Slutsker I., Kinne S.; Wavelength dependence of the optical depth of biomass burning, urban, and desert dust aerosols; Journal of Geophysical Research 104, D24 (1999) 31333-31349

[143] Schuster G.L., Dubovik O., Holben B.N.; Angstrom exponent and bimodal aerosol size distributions; Journal of Geophysical Research 111, D07207 (2006) doi:10.1029/2005JD006328

[144] Moosmüller H., Chackabarty R.K.; Technical Note: Simple Analytical Relationships between Ångström Coefficients of Aerosol Extinction, Scattering, Absorption, and Single Scattering Albedo; Atmospheric Chemistry and Physics 11 (2011) 10677-10680; https://doi.org/10.5194/acp-11-10677-2011

[145] Kaufman, Y. J.; Aerosol optical thickness and atmospheric path radiance; Journal of Geophysical Research 98, D2 (1993) 2677–2692

[146] Zotter P., Herich H., Gysel M., El-Haddad I., Zhang Y., Močnik G. G., Hüglin C., Baltensperger U., Szidat S., Prévôt A.S.H.; Evaluation of the absorption Ångström exponents for traffic and wood burning in the Aethalometer-based source apportionment using radiocarbon measurements of ambient aerosol; Atmospheric Chemistry and Physics 17 (2017) 4229–4249; doi:10.5194/acp-17-4229-2017

[147] Ealo M., Alastuey A., Ripoll A., Pérez N., Minguillón M.C., Querol X., Pandolfi M.; Detection of Saharan dust and biomass burning events using near-real-time intensive aerosol optical properties in the north-western Mediterranean; Atmospheric Chemistry and Physics 16 (2016) 12567–12586; doi:10.5194/acp-16-12567-2016

[148] Titos G., Ealo M., Pandolfi M., Pérez N., Sola Y., Sicard M., Comerón A., Querol X., Alastuey A.; Spatiotemporal evolution of a severe winter dust event in the western Mediterranean: Aerosol optical and physical properties; Journal of Geophysical Research; Atmosphere 122 (2017) 4052–4069; doi:10.1002/2016JD026252

[149] Collaud Coen M., Weingartner E., Schaub D., Hueglin C., Corrigan C., Henning S., Schwikowski M., Baltensperger U.; Saharan dust events at the Jungfraujoch: detection by wavelength dependence of the single scattering albedo and first climatology analysis; Atmospheric Chemistry and Physics 4 (2004) 2465–2480

[150] Valenzuela A., Olmo F.J., Lyamani H., Antón M., Titos G., Cazorla A., Alados-Alarboledas L.; Aerosol scattering and absorption Angström exponents as indicators of dust and dust-free days over Granada (Spain); Atmospheric Research 154 (2015) 1–13; http://dx.doi.org/10.1016/j.atmosres.2014.10.015

[151] Sandradewi J., Prévôt A.S.H., Szidat S., Perron N., Alfarra M.R., Lanz V.A., Weingartner E., Baltensperger U.; Using Aerosol Light Absorption Measurements for the Quantitative Determination of Wood Burning and Traffic Emission Contributions to Particulate Matter; Environmental Science and Technology 42 (2008) 3316-3323; https://doi.org/10.1021/es702253m

[152] Takemura T., Nakajima T., Dubovik O., Holben B.N., Kinne S.; Single-Scattering Albedo and Radiative Forcing of Various Aerosol Species with a Global Three-Dimensional Model; Journal of Climate 15(4) (2002) doi:10.5194/acp-16-3289-2016

[153] Amato F., Alastuey A., Karanasiou A., Lucarelli F., Nava S., Calzolai G., Severi M., Becagli S., Gianelle V.L., Colombi C., Alves C., Custódio D., Nunes T., Cerqueira M., Pio C., Eleftheriadis K., Diapouli E., Reche C., Minguillón M.C., Manousakas M.-I., Maggos T., Vratolis S., Harrison R.M., Querol X.; AIRUSE-LIFE+: estimation of natural source contributions to urban ambient air PM10 and PM2:5 concentrations in southern Europe – implications to compliance with limit values; Atmospheric Chemistry and Physics 17 (2017) 3673–3685; doi:10.5194/acp-17-3673-2017

[154] Diapouli E., Manousakas M.I., Vratolis S., Vasilatou V., Pateraki S., Bairachtari K.A., Querol X., Amato F., Alastuey A., Karanasiou A.A., Lucarelli F., Nava S., Calzolai G., Gianelle V.L., Colombi C., Alves C., Custódio D., Pio C., Spyrou C., Kallos G.B., Eleftheriadis K.; AIRUSE-LIFE+: a harmonized PM speciation and source apportionment in five southern European cities; Atmospheric Chemistry and Physics 16 (2016) 3289–3309; https://doi.org/10.1021/es901558t

[155] Viana M., Amato F., Alastuey A., Querol X., Moreno T., García Dos Santos S., Herce M.D., Fernández-Patier R.; Chemical Tracers of Particulate Emissions from Commercial Shipping; Environmental Science and Technology 43 (2009) 7472–7477 https://doi.org/10.1021/es901558t

[156] Andreae T.W., Andreae M.O., Ichoku C., Maenhaut W., Cafmeier J., Kamieli A., Orlowski L.; Light scattering by dust and anthropogenic aerosol at a remote site in the Negev desert, Israel; Journal of Geophysical Research 107, D2 (2002) doi:10.1029/2001JD900252

[157] Lihavainen H., alghamdi M.A., Hyvärinen A., Hussein T., Neitola K., Khoder M., Abdelmaksoud A.S., Al-Jeelani H., Shabbaj I.I., Almehmadi F.M.; Aerosol optical properties at rural background area in Western Saudi Arabia; Atmospheric Research 197 (2017) 370–378 http://dx.doi.org/10.1016/j.atmosres.2017.07.019

[158] Fialho P., Freitas M.C., Barata F., Vieira B., Hansen A.D.A., Honrath R.E.; The Aethalometer calibration and determination of iron concentration in dust aerosols; Journal of Aerosol Science 37 (2006) 1497-1506 doi:10.1016/j.jaerosci.2006.03.002

[159] Chiapello I., Bergametti G., Chatenet B., Bousquet P., Dulac F., Santos Soares E.; Origins of African dust transported over the northeastern tropical Atlantic; Journal of Geophysical Research 102, D12 (1997) 13701-13709

[160] Formenti P., Caquineau S., Desboeufs K., Klaver A., Chevaillier S., Journet E., and Rajot J.L.; Mapping the physico-chemical properties of mineral dust in western Africa: mineralogical composition; Atmospheric Chemistry and Physics 14 (2014) 10663–10686; doi:10.5194/acp-14-10663-2014

[161] Nava S., Becagli S., Calzolai G., Chiari M., Lucarelli F., Prati P., Traversi R., Udisti R., Valli G., Vecchi R.; Saharan dust impact in central Italy: An overview on three years elemental data records; Atmospheric Environment 60 (2012) 444-452; http://dx.doi.org/10.1016/j.atmosenv.2012.06.064

[162] Caponi L., Formenti P., Massabò D., Di Biagio C., Cazaunau M., Pangui E., Chevaillier S., Landrot G., Andreae M.O., Kandler K., Pikhet S., Saeed T., Seibert D., Williams E., Balkanski Y., Prati P., Doussin J.-F.; Spectral- and size-resolved mass absorption efficiency of mineral dust aerosols in the shortwave spectrum: a simulation chamber study; Atmospheric Chemistry and Physics 17 (2017) 7175–7191; https://doi.org/10.5194/acp-17-7175-2017

[163] Jaenicke R.; Physical characterization of aerosols, In Lee S. D., Schneider T., Grant L.D., Verkerk P.J.; Eds., Aerosols, Lewis Publ., Chelsea, Mi (1986) 97-106

[164] Bahadur R., Praveen P.S., Xu Y., and Ramanathan V.; Solar absorption by elemental and brown carbon determined from spectral observations; PNAS 109, 43 (2012) www.pnas.org/cgi/doi/10.1073/pnas.1205910109

[165] Forello A.C., Bernardoni V., Calzolai G., Lucarelli F., Massabò D., Nava S., Pileci R.E., Prati P., Valentini S., Valli G., Vecchi R.; Exploiting multi-wavelength aerosol absorption coefficients in a multi-time source apportionment study to retrieve source-dependent absorption parameters; Atmospheric Chemistry and Physics 19 (2019) 11235–11252; https://doi.org/10.5194/acp-19-11235-2019

[166] Corsini E., Vecchi R., Marabini L., Fermo P., Becagli S., Bernardoni V., Caruso D., Corbella L., Dell'Acqua M., Galli C.L., Lonati G., Ozgen S., Papale A., Signorini S., Tardivo R., Valli G.; The chemical composition of ultrafine particles and associated effects at an alpine town impacted by wood burning; Science of the Total Environment 587-588 (2017) 223-231; https://doi.org/10.1016/j.scitotenv.2017.02.125

[167] Heinzerling A., Hsu J., Yip F.; Respiratory health effects of ultrafine particles in children: a literature review; Water. Air Soil Pollut. 227 (2016) https://doi.org/10.1007/s11270-015-2726-6

[168] Rogula-Kozlowska W., Keljnowski K; Submicrometer aerosol in rural and urban backgrounds in Southern Poland: primary and secondary components of PM1; Bull. Environ. Contam. Toxicol. 90 (2013) 103-109; https://doi.org/10.1007/s00128-012-0868-4

[169] Theodosi C., Grivas G., Zarmpas P., Chaloulakou A., Mihalopoulos N.; Mass and chemical composition of size-segregated aerosols (PM1, PM2.5, PM10) over Athens, Greece: local versus regional sources; Atmospheric Chemistry and Physics 11 (2011) 11895-11911; https://doi.org/10.1007/s00703-017-0538-5

[170] Vecchi R., Chiari M., D'Alessandro A., Fermo P., Lucarelli F., Mazzei F., Nava S., Piazzalunga A., Prati P., Silvani F., Valli G.; A mass closure and PMF source apportionment study on the sub-micron sized aerosol fraction at urban sites in Italy; Atmospheric Environment 42 (2008) 2240-2253 DOI

[171] Pérez N., Pey J., Querol X., Alastuey A., Lopez J.M., Viana M.; Partitioning of major and trace components in PM10-PM2.5-PM1 at an urban site in Southern Europe; Atmospheric Environment 42 (2008) 1677-1691; https://doi.org/10.1016/j.atmosenv.2007.11.034

[172] Perrone M.R., Becagli S., Orza J.A.G., Vecchi R., Dinoi A., Udisti R., Calbello M.; The impact of long-range transport on PM1 and PM2.5 at a Central Mediterranean site; Atmospheric Environment 71 (2013) 176-186; https://doi.org/10.1016/j.atmosenv.2013.02.006

[173] Giugliano M., Lonati G. Butelli P., Romele L., Tardivo R., Grosso M.; Fine particulate (PM2.5-PM1) at urban sites with different traffic exposure; Atmospheric Environment 39 (2005) 2421-2431; https://doi.org/10.1016/j.atmosenv.2004.06.050

[174] Putaud J.P., Van Dingenen R., Raes F.; Submicron aerosol mass balance at urban and semirural sites in the Milan area (Italy); Journal of Geophysical Research 107 (D22) (2002) 8198-8208; https://doi.org/10.1029/2000JD000111

[175] Eatough D-J., Farber R.; Apportioning visibility degradation to sources of PM2.5 using Positive Matrix Factorization; Journal of the Air and Waste Management Association 59 (2009) 1092-1110; doi: 10.3155/1047-3289.59.9.1092

[176] Chen W.-N., Chen Y.-C., Kuo C.-Y., Chou C.-H., Cheng C.-H., Huang C.-C., Chang S.-Y., Raman M.R., Shang W.-L., Chuang T.-Y., Liu S.-C.; The real-time method of assessing the contribution of individual sources on visbility degradation in Taichung; Science of the Total Environment 497-498 (2014) 219-228; https://doi.org/10.1016/j.scitotenv.2014.07.120

[177] Xiao S., Wang Q.Y., Cao J.J., Huang R.-J., Chen W.D., Han Y.M., Xu H.M., Liu S.X., Zhou Y.Q., Wang P., Zhang J.Q., Zhan C.L.; Long-term trends in visibility and impacts of aerosol composition on visibility impairment in Baoji, China; Atmospheric Research 149 (2014) 88-95; https://doi.org/10.1016/j.atmosres.2014.06.006

[178] Wang J., Zhang Y.-F., Feng Y.-C., Zheng X.-J., Jiao L., Hong S.-M., Shen J.-D., Zhu T., Ding J., Zhang Q.; Characterization and source apportionment of aerosol light extintion with a coupled model of CMB-IMPROVE in Hangzhou, Yangtze River Delta of China; Atmospheric Research 178-79 (2016) 570-579; https://doi.org/10.1016/j.atmosres.2016.05.009

[179] Piazzalunga A., Bernardoni V., Fermo P., Vecchi R.; Optimisation of analytical procedures for the quantification of ionic and carbonaceous fractions in the atmospheric aerosol and application to ambient samples; Analytical and Bioanalytical Chemistry 405 (2013) 1123-1132; https://doi.org/10.1007/s00216-012-6433-5

[180] Piazzalunga A., Fermo P., Bernardoni V., Vecchi R., Valli G., De Gregorio M.A.; A simplified method for levoglicosan quantification in wintertime atmospheric particulate matter by High-Performance Anion-Exchange Chromatography coupled with Pulsed Amperometric Detection; Journal of the Environmental and Analytical Chemistry 90 (12) (2010) 934-347; https://doi.org/10.1080/03067310903023619

[181] Paatero P.; User's Guide for the Multilinear Engine Program "ME2" for Fitting Multilinear and Quasi-multilinear Models; (2000)

[182] Norris G., Duvall R., Brown S., Bai S.; EPA Positive Matrix Factorization (PMF) 5.0. Fundamentals and User Guide; EPA/600/R-14/108 (2014) U.S. Environmental Protection Agency

[183] Paatero P.; User's Guide for Postive Matrix Factorization Programs PMF2 and PMF3, Part 1: Tutorial; University of Helsinki, Helsinki; Finland last changed on 31 March 2015

[184] Polissar A.V., Hopke P.K., Paatero P., Malm W.C., Sisler J.F.; Atmospheric aerosol over Alaska - 2. Elemental composition and sources; Journal of Geophysical Research 103 (1998) 19045-19057

[185] Cesari D., De Benedetto G.E., Bonasoni P., Busetto M., Dinoi A., Merico E., Chirizzi D., Cristofanelli P., Donateo A., Grasso F.M., Marinoni A., Pennetta A., Contini D.; Seasonal variability of $PM_{2.5}$ and PM_{10} composition and sources in an urban background site in Southern Italy; Science of the Total Environment 612 (2018) 202–213; http://dx.doi.org/10.1016/j.scitotenv.2017.08.230

[186] Rai P., Furger M., Slowik J., Canonaco F., Frölich R., Hüglin C., Minguillón M.C., Petterson K., Baltensperger U., Prévôt A.S.H.; Source apportionment of highly time resolved trace elements during a firework episode from a rural freeway site in Switzerland; Atmospheric Chemistry and Physics Discussion (2019); https://doi.org/10.5194/acp-2018-1229

[187] Malm W.C., Day D.E.; Optical properties of aerosols at Gran Canyon national park; Atmospheric Environment 34 (2000) 3373-3391; https://doi.org/10.1016/S1352-2310(00)00108-4

[188] Prenni A.J., Hand J.L., Malm W.C., Copeland S., Luo G., Yu F., Taylor N., Russell L.M., Schichtel B.A.; An examination of the algorithm for estimating light extinction from IMPROVE particle speciation data; Atmospheric Environment 214 (2019) 116880; https://doi.org/10.1016/j.atmosenv.2019.116880

[189] Clarke A.D.; Effects of filter internal reflection coefficient on light absorption measurements made using the integrating plate method; Applied Optics 21 (1982) 3021-3031

[190] Sagan C., Pollack J.B.; Anisotropic nonconservative scattering and the clouds of Venus; Journal of Geophysical Research 72 (1967) 469-477

[191] Sellers W.D.; A new global climate model; Applied Meteorology 12 (1973) 241-254

[192] Hansen J.E.; Exact and approximate solutions for multiple scattering by clouds and hazy planetary atmospheres; Journal of Atmospherical Science 26 (1969) 478-487

List of Publications

Peer-reviewed papers

P1 Forello A.C., Bernardoni V., Calzolai G., Lucarelli F., Massabò D., Nava S., Pileci R.E., Prati P., Valentini S., Valli G., Vecchi R.; Exploiting multi-wavelength aerosol absorption coefficients in a multi-time source apportionment study to retrieve source-dependent absorption parameters; Atmospheric Chemistry and Physics 19 (2019), 11235–11252; https://doi.org/10.5194/acp-19-11235-2019

P2 Valentini S., Bernardoni V., Massabò D., Prati P., Valli G. and Vecchi R.; Tailored coefficients in the algorithm to assess reconstructed light extinction at urban sites: A comparison with the IMPROVE revised approach; Atmospheric Environment 172 (2018), 168-176, https://doi.org/10.1016/j.atmosenv.2017.10.038

P3 Vecchi R., Bernardoni V., Fermo P., Piazzalunga A., Valentini S., and Valli G.; Assessment of light extinction at a European polluted urban area during wintertime: Impact of PM1 composition and sources; Environmental Pollution 233 (2018), 679-689, https://doi.org/10.1016/j.envpol.2017.10.059

P4 Costabile F., Alas H., Aufderheide M., Avino P., Amato F., Argentini S., Barnaba F., Berico M., Bernardoni V., Biondi R., Calzolai G., Canepari S., Casasanta G., Ciampichetti S., Conidi A., Cordelli E., Di Ianni A., Di Liberto L., Facchini M.C., Facci A., Frasca D., Gilardoni S., Grollino M.G., Gualtieri M., Lucarelli F., Malaguti A., Manigrasso M., Montagnoli M., Nava S., Padoan E., Perrino C., Petralia E., Petenko I., Querol X., Simonetti G., Tranfo G., Ubertini S., Valli G., Valentini S., Vecchi R., Volpi F., Weinhold K., Wiedensholer A., Zanini G., Gobbi G.P.; First results of the "Carbonaceous aerosol in Rome and Environs (CARE)" experiment: beyond current standards for PM10; Atmosphere 2017, 8, 249; doi: 10.3390/atmos8120249

P5 Bernardoni V., Elser M., Valli G., Valentini S., Bigi A., Fermo P., Piazzalunga A., Vecchi R.; Size-segregated aerosol in a hot-spot pollution urban area: Chemical

composition and three-way source apportionment; Environmental Pollution 231 (2017), 601-611, https://doi.org/10.1016/j.envpol.2017.08.040

Papers submitted to peer-reviewed journals

S1 Valentini S., Barnaba F., Bernardoni V., Calzolai G., Costabile F., Di Liberto L., Forello A.C., Gobbi G.P., Gualtieri M., Lucarelli F., Nava S., Petralia E., Valli G., Wiedensohler A., Vecchi R.; Classifying aerosol particles through the combination of optical and physical-chemical properties: Results from a wintertime campaign in Rome (Italy); Atmospheric Research, under revision

Contributions in volumes

V1 Bernardoni V., Forello A.C., Mariani F., Paroli B., Potenza M.A.C., Pullia A., Riccobono F., Sanvito T., Valentini S., Valli G., Vecchi R.; Innovative instrumentation for the study of atmospheric aerosol optical properties; Toward a Science Campus in Milan. A Snapshot of Current Research at the Physics Department Aldo Pontremoli, Springer; ISBN 978-3-030-01628-9 ISBN 978-3-030-01629-6 (eBook); https://doi.org/10.1007/978-3-030-01629-6

Presentations to international conferences

Oral presentations (author in bold to indicate the presenter)

IO1 Valentini S., Bernardoni V., Bundke U., Forello A.C., Massabò D., Petzold A., Prati P., Soldan F., Valli G., **Vecchi R.**, Weber P.; Multi-wavelength Polar Photometers to Assess Absorption Optical Properties of Aerosol Collected on Filters; European Aerosol Conference EAC2019

IO2 **Vecchi R.**, Bernardoni V., Valentini S., Piazzalunga A., Fermo P., Valli G.; Contribution of PM1 composition and sources to light extinction in a hot-spot pollution urban area in Europe; European Aerosol Conference EAC2019

IO3 **Forello A.C.**, Bernardoni V., Calzolai G., Lucarelli F., Massabò D., Nava S., Pileci R.E., Prati P., Valentini S., Valli G. and Vecchi R.; Multi-time source apportionment: exploiting multi-wavelength aerosol absorption coefficient to better identify sources; European Aerosol Conference EAC2019

IO4 Valentini S., Bernardoni V., Calzolai G., Costabile F., Di Liberto L., Gobbi G.P., Gualtieri M., Lucarelli F., Nava S., Petralia E., Valli G. and Vecchi R.; High time-resolved optical and chemical characterisation of wintertime aerosol in Rome (Italy): case studies; 12th International Conference on Carbonaceous Particles in the Atmosphere (ICCPA) 2019

IO5 **Vecchi R.**, Bernardoni V., Forello A., Massabò D., Prati P., Soldan F., Valentini S. and Valli G.; Exploiting the features of multi-λ polar photometers to retrieve optical properties of aerosols collected on filters; 12th International Conference on Carbonaceous Particles in the Atmosphere (ICCPA) 2019

IO6 **Bernardoni V.**, Ferrero L., Soldan F., Valentini S., Massabò D., Močnik G., Gregorič A., Cataldi M-A., Bolzacchini E., Prati P., Valli G. and Vecchi R.; Multi-wavelength aerosol absorption coefficient measurements: instrument inter-comparison and results of source and source-component modelling; 12th International Conference on Carbonaceous Particles in the Atmosphere (ICCPA) 2019

IO7 **Bernardoni V.**, Ferrero L., Soldan F., Valentini S., Massabò D., Močnik G., Gregorič A., Cataldi M., Bolzacchini E., Prati P., Valli G., Vecchi R.; WG3 COLOSSAL winter campaign 2018 in Milan – Part 1: Instruments inter-comparison and results of source and source-component modelling by multi-wavelength aerosol absorption coefficient measurements; COST Action CA16109 COLOSSAL-WG3 meeting, 16 January 2019, Leipzig, Germany

IO8 **Teri M.**, Gasteiger J., Müller T., Valentini S., Horvath H., Schöberl M., Dollner M., Seibert P., Philipp A., Vecchi R., Weinzierl B.; Airborne multi-wavelength polar scattering measurements in Saharan and Arabian dust layers during A-LIFE; 2nd A-LIFE Workshop, 28 November 2018, Darmstadt, Germany

IO9 Bernardoni V., Forello A.C., Pileci R.E., Valentini S., Valli G., **Vecchi R.**, Caponi L., Prati P., Massabò D.; Multi-wavelength absorption coefficient measurements of aerosol collected on filters: instrumentation and modelling developments for brown carbon studies; Aerosol Technology Conference 2018 (AT2018)

Poster presentations (author in bold to indicate the presenter)

IP1 Valentini S., Barnaba F., Bernardoni V., Calzolai G., Costabile F., Di Liberto L., Gobbi G.P., Gualtieri M., Lucarelli F., Nava S., Petralia E., Valli G., **Vecchi R.**; Optical and Physical-Chemical Properties of Wintertime Aerosol in Rome (Italy) Measured with High Time Resolution: Case Studies; European Aerosol Conference EAC2019

IP2 Bernardoni V., Ferrero L., Soldan F., Valentini S., Massabò D., Močnik G., Gregorič A., Cataldi M., Bolzacchini E., Prati P., Valli G., **Vecchi R.**; Multi-wavelength aerosol absorption coefficient measurements: instrument inter-comparison and implications for source and component apportionment; European Aerosol Conference EAC2019

IP3 **Valentini S.**, Weber P., Bernardoni V., Bundke U., Massabò D., Petzold A., Prati P., Valli G. and Vecchi R.; Multi-Wavelength Measurement of Aerosol Optical Properties: Laboratory Intercomparison of In-Situ and Filter-Based Techniques; 12th International Conference on Carbonaceous Particles in the Atmosphere (ICCPA) 2019

IP4 **Forello A.C.**, Bernardoni V., Calzolai G., Lucarelli F., Massabò D., Nava S., Pileci R., Prati P., Valentini S., Valli G. and Vecchi R.; Retrieving information on black and brown carbon emission sources exploiting aerosol optical properties in an advanced receptor model; 12th International Conference on Carbonaceous Particles in the Atmosphere (ICCPA) 2019

IP5 **Vecchi R.**, Bernardoni V., Bigi A., Calzolai G., Elser M., Fermo P., Forello A., Lucarelli F., Massabò D., Nava S., Piazzalunga A., Pileci R.E., Prati P., Valentini S., Valli G.; Advanced Receptor Models as a Tool to Improve the Knowledge of Aerosol Emission Sources at a Hot-Spot Pollution Site (Milan – Italy); International Aerosol Conference IAC2018

IP6 **Valentini S.**, Bernardoni V., Massabò D., Prati P., Valli G. and Vecchi R.; Light extinction estimates using the IMPROVE algorithm: The relevance of site-specific coefficients; European Aerosol Conference EAC2017

Presentations to national conferences

Oral presentations (author in bold to indicate the presenter)

NO1 **Valentini S.**, Bernardoni V., Fermo P., Massabò D., Piazzalunga A., Prati P., Valli G., Vecchi R.; Studio dell'impatto delle sorgenti di PM1 sul coefficiente di estinzione atmosferico in area urbana; Convegno Nazionale sul Particolato Atmosferico PM2018

NO2 **Forello A.C.**, Bernardoni V., Calzolai G., Massabò D., Lucarelli F., Nava S., Pileci R.E., Prati P., Valentini S., Valli G., Vecchi R.; Multi-time source apportionment. Un approccio avanzato per l'identificazione delle sorgenti di par-

ticolato atmosferico a Milano; Convegno Nazionale sul Particolato Atmosferico PM2018

NO3 Bernardoni V., Elser M., Valli G., Forello A., Valentini S., Bigi A., Fermo P., Piazzalunga A., Vecchi R.; Source apportionment 3-D di aerosol urbano separato dimensionalmente mediante impattore multistadio. Convegno Nazionale sul Particolato Atmosferico PM2018

NO4 Bernardoni V., Forello A.C., Mariani F., Paroli B., Potenza M.A.C., Pullia A., Riccobono F., Sanvito T., Valentini S., Valli G., Vecchi R.; Optical properties of atmospheric aerosol: development of innovative instrumentation and modelling applications; Congresso del Dipartimento di Fisica 2017 - Milano

Poster presentations (author in bold to indicate the presenter)

NP1 Nava S., Calzolai G., Chiari M., Lucarelli F., Costabile F., Di Liberto L., Gobbi G.P., Bernardoni V., Valentini S., Valli G., Vecchi R.; Studio del particolato atmosferico urbano con alta risoluzione temporale. Risultati delle analisi orarie PIXE e termo-ottiche del progetto CARE; Convegno Nazionale sul Particolato Atmosferico PM2018

NP2 Valentini S., Bernardoni V., Massabò D., Prati P., Valli G. and Vecchi R.; Tailoring coefficients in IMPROVE algorithm to assess site-specific chemical light extinction; Congresso del Dipartimento di Fisica 2017 - Milano

NP3 Forello A.C., Bernardoni V., Calzolai G., Chiari M., Lucarelli F., Massabò D., Nava S., Prati P., Valentini S., Valli G., Vecchi R.; High-time resolved atmospheric aerosol characterization for source apportionment studies; Congresso del Dipartimento di Fisica 2017 – Milano

Acknowledgments

The author is grateful to the referees Dr. Daniele Contini and Prof. Maria Rita Perrone for their contribution.

I would like to acknowledge all people from the Environmental Physics research group of the University of Milan and INFN-Milan and from institutions collaborating to this work for instruments deployment, technical support, data analyses, and fruitful discussions.
In particular, I am grateful to researchers from: Aerosol Physics and Environmental Physics group - Universität Wien; Jülich Forschungszentrum; ISAC-CNR Rome; Department of Chemistry - Università La Sapienza (Rome); IIA-CNR Rome; Department of Physics - University of Genoa and INFN-Genoa; Physics Department - University of Florence; INFN-LABEC Florence; ENEA-SSPT-MET – Atmospheric Pollution Laboratory (INAT); Leibniz Institute for Tropospheric Research (TROPOS); and from all CARE research groups.

A special mention goes to my supervisor Prof. Roberta Vecchi for having guided me throughout the PhD and having made this work possible.
A particular ackowledgement goes also to Univ. -Prof. Dr. Bernadett Weinzierl for her welcome and support in Vienna, where I learnt a lot from her and the whole Aerosol group.

Ringraziamenti

Grazie ancora a Roberta per l'enorme sostegno, sia scientifico che morale, datomi in ogni fase del Dottorato di Ricerca: mi ha resa più matura e consapevole.
Un sentito ringraziamento anche a Vera e Gianluigi per la collaborazione e le sempre utili discussioni, che mi hanno insegnato molto sull'aerosol e dal punto di vista personale.
Un grazie speciale alla mia compagna di ufficio (e "di merende", letteralmente...) Alice per i consigli, il supporto e semplicemente per la bella compagnia.
Ringrazio vivamente anche Marilena per aver condiviso con me una parte importante del Dottorato e della vita e per essere la mia personale guida di Vienna e della sua cultura.

Sono molto grata a tutti i miei amici per essermi sempre vicini e per i tanti momenti spensierati trascorsi insieme.

Ringrazio la mia famiglia e soprattutto il mio babbo per essere mio confidente e parte razionale "sostitutiva" quando la mia viene sommersa dal lato emotivo.

Infine ringrazio il mio fidanzato Stefano. Grazie per supportarmi e sopportarmi ogni giorno; sono estremamente grata che tu scelga di condividere la tua vita con me.